Journal of Geochemical Exploration 267 (2024) 107598

Contents lists available at ScienceDirect

Journal of Geochemical Exploration

journal homepage: www.elsevier.com/locate/gexplo

Advanced exploration of rare metal mineralization through integrated remote sensing and geophysical analysis of structurally-controlled hydrothermal alterations

Mohamed A. Abdelkader [a,b], Yasushi Watanabe [a], Ali Shebl [c,d,*], Mohamed Badawi [e,f], Maher Dawoud [b], Hanaa A. El-Dokouny [b], Árpád Csámer [c,g], Mahmoud Abdellatif [h]

[a] *Department of Earth Resource Science, Graduate School of International Resource Sciences, Akita University, 010-8502 Akita, Japan*
[b] *Department of Geology, Faculty of Science, Menoufia University, 32513 Menoufia, Egypt*
[c] *Department of Mineralogy and Geology, University of Debrecen, 4032 Debrecen, Hungary*
[d] *Department of Geology, Faculty of Science, Tanta University, 31527 Tanta, Egypt*
[e] *Institute of Exploration Geosciences, University of Miskolc, Miskolc 3515, Hungary*
[f] *Department of Geology, Faculty of Science, Mansoura University, Mansoura 35516, Egypt*
[g] *Cosmochemistry and Cosmic Methods Research Group, University of Debrecen, Debrecen 4032, Hungary*
[h] *Department of Geology, Faculty of Science, South Valley University, 83523 Qena, Egypt*

ARTICLE INFO

Keywords:
Hydrothermal alterations
Rare metals
ASTER
Sentinel-2
Mineral chemistry
Arabian Nubian Shield

ABSTRACT

Fusing multi-source (remote sensing and geophysical) data and diverse approaches validation in targeting hydrothermal alteration and structural anomalies enhances the potential for accurately detecting and characterizing mineralization zones. Sentinel 2 data and ASTER were processed for lithological and hydrothermal alteration mapping in the rare metal-rich Umm Naggat area (Egypt). Different image processing techniques were implemented, including false color composites, minimum noise fraction, band rationing, band math, mineral indices, relative absorption band depth, and constrained energy minimization. The rare metal-bearing Umm Naggat younger granite (NYG) pluton was lithologically discriminated and intra-differentiated to mafic-rich biotite granites, mafic-poor alkali feldspar granites, and albitized granites. Extensive hydrothermal alterations, such as albitization, ferrugination, propylitization, argillization, and phyllitization, overprint the NYG pluton. Normalized standard deviation, automatic lineament extractions, and trend analysis highlighted the key structural directions (NW, NNW, NNE, and NE) and distinguished the NYG pluton as a moderate to high structural density zone. The high structural density and intensive alteration zones are spatially associated and more localized within the NYG pluton than the surrounding rocks. Spatial overlay analysis confirmed that the hydrothermal alterations and fluid circulation systems are structurally-controlled. Furthermore, the hydrothermal alteration mapping and structural analysis outcomes were verified by combining fieldwork, slab polishing, petrographic investigations, and mineral chemistry through semi-quantitative scanning electron microscopy with energy dispersive spectroscopy (SEM-EDS) and quantitative electron probe microanalysis (EPMA) analysis. As a result, the hydrothermal genesis of rare metal-bearing minerals (Nb-rutile, Nb-ilmenite, and columbite) close to or incorporated within alteration minerals (chlorite, muscovite, and hematite) is confirmed from the alteration zones (propylitic, phyllic, and ferruginated). In addition, biotite muscovitization and chloritization significantly contribute to the secondary rare metal enrichment. The current study emphasizes the extensive distribution of secondary rare metal-bearing minerals within the entire NYG pluton (not only limited to the northern albitized granite as depicted by previous studies), which might shed light on these hydrothermally-altered younger granites as a new potential source for Nb and Ta in Egypt.

---

* Corresponding author at: Department of Mineralogy and Geology, University of Debrecen, 4032 Debrecen, Hungary.
E-mail address: ali.shebl@science.tanta.edu.eg (A. Shebl).

https://doi.org/10.1016/j.gexplo.2024.107598
Received 23 October 2023; Received in revised form 8 August 2024; Accepted 3 October 2024

1. Introduction

Deep-seated tectonic zones are the main structures that run deep into the Earth's crust. Regarding the Arabian Nubian Shield (ANS), where our study area is located, they are mostly connected to the Pan-African Orogeny's transpressive (like metamorphic domes and nappe assemblage thrust packages) and extensional (like molasse sedimentary basins and post-orogenic magmatism) features. They act as channels for magmatic-bearing fluids flowing through these fracture systems to the surface, consequently localizing potential mineralization. These zones are distinguished by mafic and acidic affinities (Garson and Krs, 1976; Hamimi et al., 2020; Hamimi et al., 2021b; Johnson, 2021; Krs, 1977; Nations, 1973).

The intrusion of such younger granites characterizes Egypt's late Neoproterozoic crustal evolution (Abdel-Rahman and El-Kibbi, 2001; El Hadek et al., 2016; Hamimi et al., 2021a; Hamimi et al., 2020; Hamimi et al., 2021b; Hussein, 1973; Johnson, 2021; Küster, 2009; Sabet, 1973). These granites represent 30 % of the plutonic batholiths within the Egyptian Basements, with a notable prevalence in the Northern regions compared with the Central and Southern ones (Akaad and AM, 1978; El-Gaby et al., 1988; Hamimi et al., 2021a; Hamimi et al., 2020; Hamimi et al., 2021b; Johnson, 2021; Said, 1990). These granitic are classified as post-orogenic to anorogenic and are composed of monzogranite, syenogranite, and alkali granite (Beyth et al., 1994; Hamimi et al., 2021a; Hamimi et al., 2020; Hamimi et al., 2021b; Johnson, 2021; Said, 1990; Stern and Gottfried, 1986).

In Egypt's Central Eastern Desert, more than 15 rare-metal granitic bodies and pegmatitic systems have been identified such as Abu Dabbab, Nuweibi, Igla, Zabara, Sikait, Abu Rusheid, Mueilha, Humr Waggat, El-Yetima, Um Salim, Ineigi, Umm Naggat, Um Bisilla, EI-Bakriya, and Abu Diab (Abd El Wahed, 2006; Abdalla and Mohamed, 1999; Abdalla et al., 2008; Abouzeid and Khalid, 2011; Dawood, 2010; El-Rus et al., 2017; El-Sayed et al., 2004; El-Sayed, 2006; Emam et al., 2018; Hamimi et al., 2021a; Hamimi et al., 2020; Hamimi et al., 2021b; Johnson, 2021; Melcher et al., 2015; Moghazi et al., 1999; Sabet, 1973; Sami et al., 2017; Sami et al., 2018). Niobium and tantalum, classified as rare metals, possess considerable geological and economic importance. The economic significance of niobium and tantalum is relevant due to their scarcity and crucial role in present-day technology. This has led to increased global exploration activities and emphasized the necessity for new potential sources to maintain a sustainable supply chain (Abd El Wahed, 2006; Abdalla et al., 2008; Abuamarah et al., 2022; Azer et al., 2019; El-Dokouny et al., 2023; El-Rus et al., 2017; Khedr et al., 2023; Zoheir et al., 2020). Recently, several approaches utilizing traditional remote sensing techniques and machine learning (ML) methods were used for mapping rare metal and rare earth-rich granites and granitic pegmatites (Abdelkader et al., 2022; Cardoso-Fernandes et al., 2021; Cardoso-Fernandes et al., 2020; Köhler et al., 2021; Santos et al., 2022).

Integrating remote sensing satellite images and geophysical data with laboratory methods, such as petrography and mineral chemistry analysis, represents a swift and cost-efficient means of identifying hydrothermal areas for mineral extraction to facilitate the exploration and utilization of mineral resources of such granitic rocks (Aali et al., 2022; Alrefaee et al., 2023; Araffa et al., 2022; Badawi et al., 2023; Cardoso-Fernandes et al., 2020; El-Qassas et al., 2023; Gabr et al., 2022; Gemusse et al., 2023; Hegab et al., 2022; Mahdi et al., 2022; Olatunji, 2022; Salawu et al., 2023; Santos et al., 2022; Sayah et al., 2023; Shebl et al., 2022; Shebl et al., 2023a; Shebl et al., 2021). Throughout the hydrothermal processes, the alteration zones can be detected and precisely characterized and categorized (albitization, ferrugination, propylitic, argillic, and phyllic) based on their spectral characteristics and extent, which can be observed through ASTER and Sentinel 2 data.

Consequently, within the Umm Naggat area (Egypt), the present investigation utilized Sentinel 2, ASTER, and aeromagnetic datasets due to their superiority in similar geological applications. These datasets had the leverage to highlight several forms of hydrothermal alteration, structures, and their associated mineralization (rare-metal bearing), which can serve as valuable indicators for identifying promising mineralization zones (e.g., Nb and Ta). This investigation was then corroborated through field surveys, petrographic examinations, and mineral chemistry through scanning electron microscopy with energy dispersive spectroscopy (SEM-EDS) and electron probe microanalysis (EPMA), reinforcing the accuracy of our findings. Additionally, the current research substantially contributes to the continuing debate regarding the hydrothermal genesis of rare metals. It triggers the need for additional research and investigation of unexplored reservoirs of hydrothermally-generated rare metal deposits, which might be a new potential source for Nb and Ta mineralization in Egypt and worldwide.

2. Study area and geological setting

The Umm Naggat area is situated in the Central Eastern Desert of Egypt within longitudes 34° 10″E–34° 19″E and latitudes 25° 27″N–25° 32″N (Fig. 1a, b). It mainly comprises igneous and metamorphic basement rocks such as serpentinites, metagabbro-diorites, metavolcanics, metasedimentary rocks, older granites, and rare metal-bearing younger granites (Fig. 1c) (Abd El Nabi, 2012; Abdelkader et al., 2022; Al-Arifi et al., 2021; Badr et al., 2014; El-Afandy et al., 2000; Gaafar, 2015; Gaafar et al., 2022; Gamal-Adeen et al., 2023). The former lithological units are frequently dissected by several trachyte plugs and dykes.

The Umm Naggat rare metal-bearing younger granite (NYG) constitutes the major rock unit in the study area, forming a high, mountainous, nearly oval-shaped pluton (Fig. 1b). The NYG pluton is classified into three distinct granitic varieties: mafic-rich biotite granites, mafic-poor alkali feldspar granites, and albitized granites (Fig. 1c) (Abdelkader et al., 2022). The granitic pluton has irregular boundaries and sharp intrusive contacts towards the country rocks. Several offshoots of the NYG are frequently recorded within the metavolcanics, metasedimentary rocks, and older granites along the intrusion's northern side.

Biotite granite (BTG) is predominantly exposed in the southern and western parts of the NYG, forming a 25 km^2 -body that extends in the East-West direction (Figs. 1c and 2a). Several scattered occurrences of the BTG are recorded in the northwestern portion of the study area (Fig. 1c). Moreover, enclaves of older rocks, specifically metagabbro-diorites, are frequently observed within the biotite granite. The latter is considered the early-crystallized granitic phase within the pluton. The BTG mainly consists of biotite-rich alkali feldspar granite; however, biotite-rich monzogranite and syenogranite variations are infrequently recorded around the outer peripheries of the pluton. It usually exhibits gradational contacts towards the mafic-poor alkali feldspar granite and the albitized granite (Fig. 2d). The BTG is characterized by coarse-grained textures, buff to reddish colors, and considerable amounts of mafic minerals, particularly biotite, Fe-Ti oxides, and amphibole (Fig. 2e).

The mafic-poor alkali feldspar granite (AFG) outcrops in the central part of the NYG pluton, located to the North of the BTG (Fig. 1c). It usually shows moderate to high reliefs and grades into albitized granite along its northern boundaries (Fig. 2b). The AFG represents a more differentiated phase after the BTG. It exhibits medium to coarse-grained textures and massive structures characterized by a relatively lower abundance of mafic minerals than the BTG (Fig. 2f).

The albitized granite (ABG) predominantly exists as marginal dome-shaped cupolas or protrusions around the NYG's peripheries (Fig. 2c). The most prominent outcrop of the ABG is situated towards the North of the AFG, constituting an E-W-oriented body covering a distance of approximately 3 km (Fig. 1c). The ABG mainly exhibits irregular boundaries, low to moderate reliefs, and is distinguished by whitish fine- to medium-grained texture (Fig. 2g). Furthermore, it exhibits gradational contacts with biotite granite and the mafic-poor alkali feldspar granite (Fig. 2b, d). At the northern contacts of the NYG, numerous apophyses of the albitized granites intrude into the surrounding

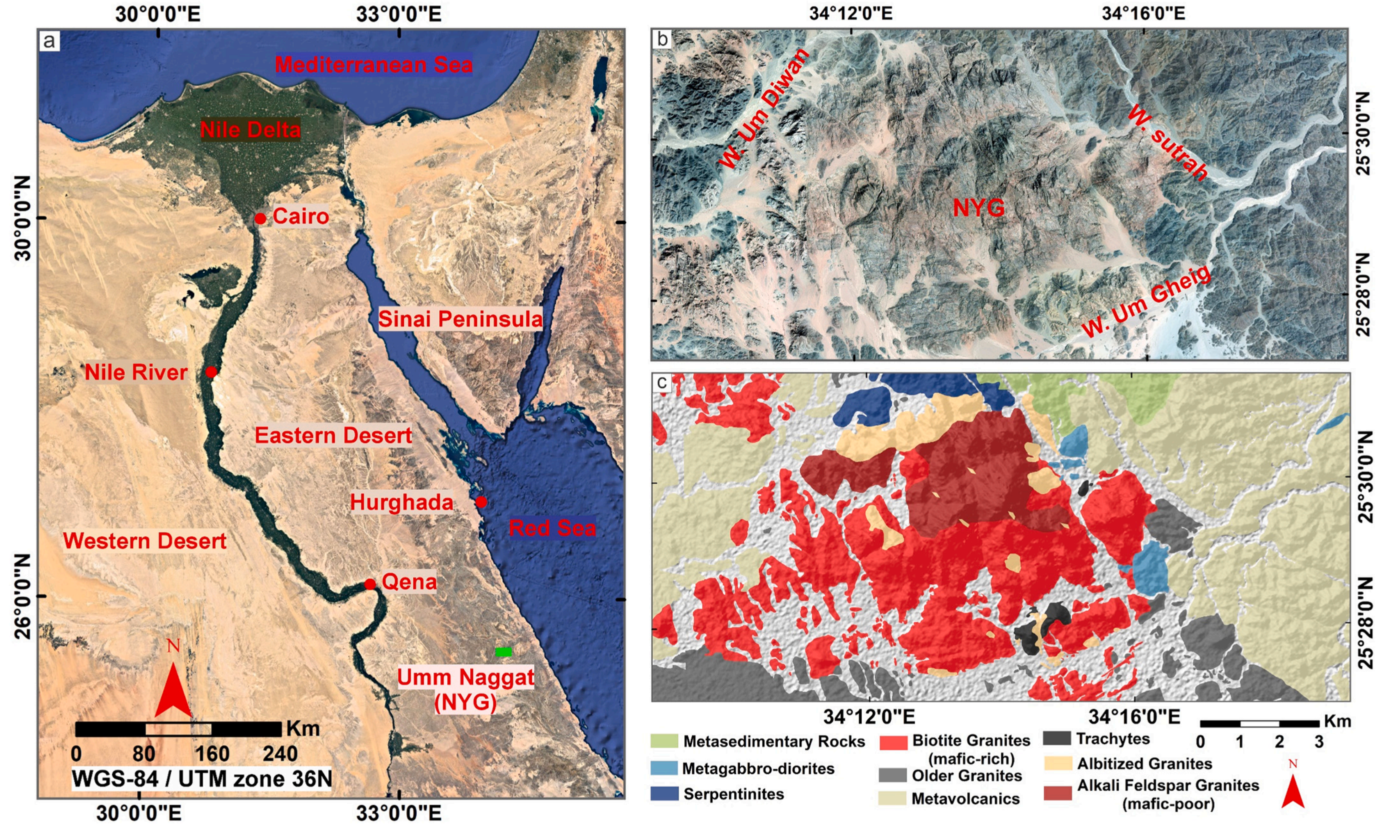

Fig. 1. (a) A simplified map of Egypt shows the main geomorphological units and location of the study area, (b) Google satellite image showing the main topography and wadies of the study area with the Umm Naggat younger granite pluton (NYG) in the center, and (c) geological map of the exposed rock units in the Umm Naggat area modified after Abdelkader et al. (2022).

metavolcanics.

Generally, The NYG pluton has undergone significant metasomatic reworking due to the infiltration of hydrothermal fluids, resulting in various alterations and rare metal enrichment (Abd El Nabi, 2012; Abdelkader et al., 2022; Al-Arifi et al., 2021; Gaafar et al., 2022; Gamal-Adeen et al., 2023; Khedr et al., 2023). The most common alterations are Na-metasomatism (albitization), chloritization, muscovitization, silicification, argillization, and ferrugination. Swarms of quartz-fluorite veins are prevalent. The NYG pluton exhibits chilled margins and locally distinct blackish to brownish staining, primarily attributed to impregnations of Fe-Mn-rich infiltrations along the joint planes and shearing zones. The NYG pluton is dissected by several post-granitic acidic to basic dykes and strike-slip faults of predominating NS, NNW, and NNE trends.

3. Materials and methodology

3.1. Remote sensing data and pre-processing

The present study employed multi-sensor satellite data from Sentinel 2 and Advanced Spaceborne Thermal Emission and Reflection Radiometer (ASTER) to decipher the nature and distribution of hydrothermal alterations as well as the structural framework linked to rare metal-hosting granites in the Umm Naggat area (Appendix A). The Sentinel 2A satellite, as a part of the Copernicus Project's multispectral imaging mission, was launched on June 23, 2015. It operates in conjunction with the Sentinel 2B satellite, successfully launched on May 7, 2017, creating a binary satellite system. The Sentinel 2 satellite comprises a total of 13 spectral channels that span from visible light to shortwave infrared. These channels can be classified into two sets: (1) ten visible and near-infrared (VNIR) bands spanning a wavelength range of 0.433–0.955 μm, and (2) three shortwave infrared (SWIR) bands with a wavelength range of 1.360–2.28 μm (Appendix A). The spatial coverage of each Sentinel 2 scene is 290 × 290 km^2.

The ASTER satellite, a component of NASA's Earth Observing System program, was successfully launched on December 18, 1999. The ASTER data encompasses 14 spectral channels distributed across three distinct spectral domains, ranging from the visible light region to the thermal infrared region: (1) three VNIR bands spanning a wavelength range of 0.52–0.86 μm with a 15-m spatial resolution; (2) six SWIR bands with a wavelength range of 1.6–2.43 μm and a 30-m spatial resolution; (3) five thermal infrared (TIR) bands having a wavelength range of 8.125–11.65 μm and a 90-m spatial resolution (Appendix A). Each scene captured by ASTER encompasses a spatial extent of 60 × 60 km^2. The performance of the ASTER subsystems was rudimentary until April 2008. No additional SWIR data could be acquired at that time due to a malfunction of the detector cooling apparatus (not the Stirling cycle chiller) in the SWIR subsystem (Abrams and Yamaguchi, 2019).

The study utilized the two satellite scenes (Sentinel 2, acquired on August 30, 2021, and ASTER, acquired on March 29, 2004) for further image processing, spectral characterization, and structural analysis. Both datasets (ASTER and Sentinel 2) are free of clouds, and the area is completely arid, maximizing the output of the remote sensing analysis in hydrothermal alteration detection. The atmospheric preprocessing of the Sentinel 2 satellite remote sensing dataset was conducted using the sen2cor processor, which is integrated into the Sentinel 2 Application Platform (SNAP). The ASTER satellite data underwent atmospheric and radiometric correction using the Fast Line-of-Sight Atmospheric Analysis of Spectral Hypercubes (FLAASH) plugin combined with the Environment for Visualizing Images (ENVI) (version 5.6) and ArcGIS software packages (version 10.8). Unifying the data characteristics is recommended for spectral analysis studies to maintain better

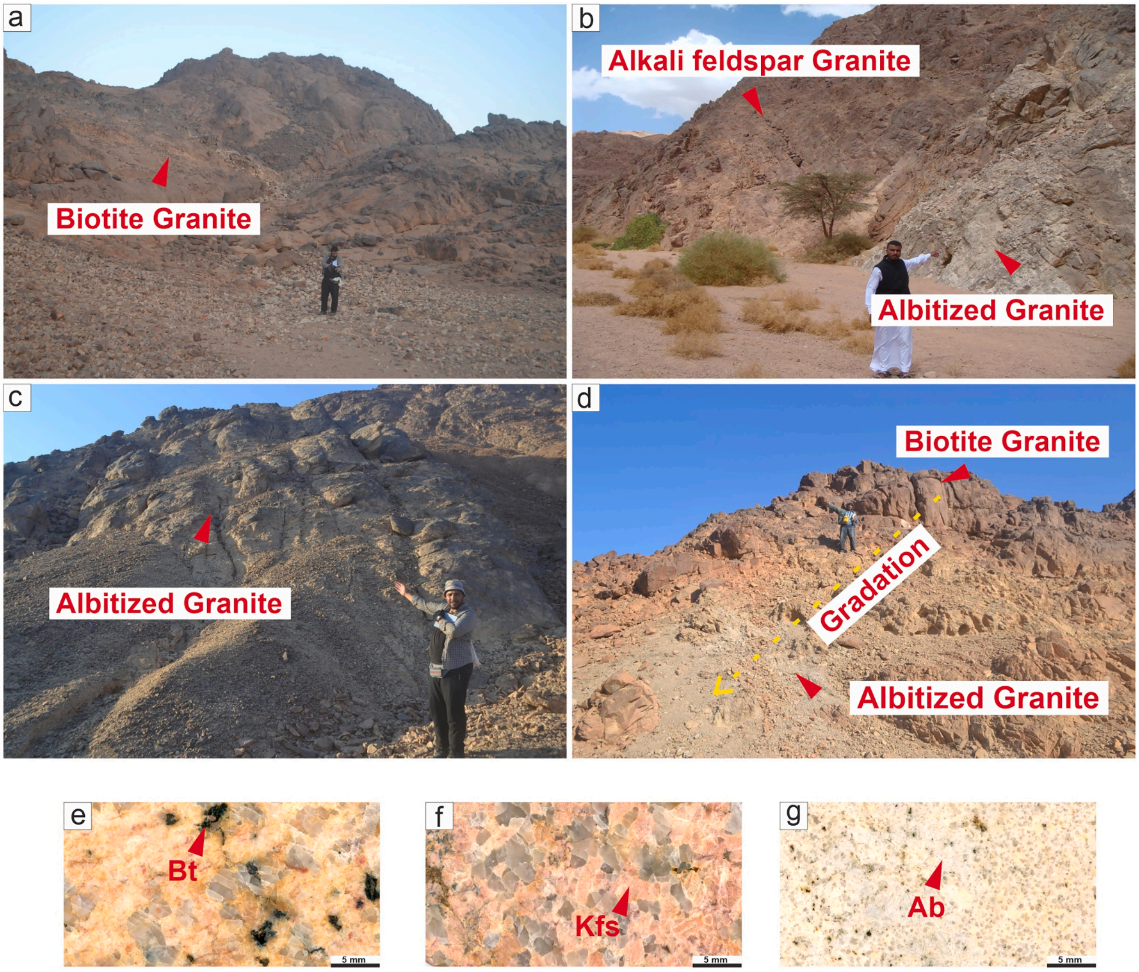

Buff mafic-rich biotite granite

Red mafic-poor alkali feldspar granite

White albitized granite

Fig. 2. Field photographs show (a) an outcrop of the reddish buff mafic-rich biotite granite (BTG), (b) an outcrop of the reddish mafic-poor alkali feldspar granite (AFG) in contact with the whitish Albitized granite (ABG), (c) a large outcrop of the albitized granite, exhibiting white color, in the southwestern part of the NYG, (d) the gradational contact between the biotite granite and the albitized granite, (e, f, and g) polished hand specimens from the BTG, AFG, and ABG, respectively. (For interpretation of the references to color in this figure legend, the reader is referred to the web version of this article.)

comparison results. Therefore, Sentinel 2 and ASTER surface reflectance scenes were resized to the study area boundaries (to minimize the computational analysis time) and underwent resampling to achieve a pixel size of 10 m. Fusing ASTER and Sentinel 2 data was performed using the Gram-Schmidt pan-sharpening methodology proposed by Chen et al. (2022) to enhance the lithological mapping results. Their study provided evidence supporting the efficacy of fusing ASTER and Sentinel 2 data to improve ASTER's ground resolution while preserving its spectral consistency (Abdelkader et al., 2022; Chen et al., 2022). Chen et al. (2022) stated that Principal Component Analysis (PCA), Gram–Schmidt (GS), and High-Pass Filtering (HPF) had the best fusion effect. The fused bands utilized in their study are Sentinel 2 b2, b3, b4, and b8, which correspond to the wavelength range of the ASTER bands. The imagery utilized in this study has undergone georeferencing to the UTM zone 36 North projection, employing the WGS84 datum.

3.2. Airborne geophysical (aeromagnetic) data

The Total magnetic intensity (TMI) map of the Umm Naggat area (Fig. 3a) is a part of the aeromagnetic survey conducted by the aero-service division of Western Geophysical Company of America surveyed and compiled between 1983 and 1984 (Aero-Service, 1984). The survey covered a large section of the central and northern Red Sea Mountains in the eastern desert of Egypt as part of the mineral, groundwater, and petroleum assessment program. The survey used the following flight specifications: (1) Flight altitude is 120 m terrain clearance, (2) The flight line direction is NE-SW, (3) Traverse flight line spacing is 1.5 km, (4) Tie line spacing is 10 km., and (5) Twin-engine Cessna-Titan, type 404 aircraft. The TMI data is reduced to the magnetic pole (Fig. 3b) to place the magnetic anomalies directly over their sources.

3.3. Methodology

3.3.1. Satellite imagery processing techniques

Various techniques have been employed for the analysis of multispectral data, such as false color composites (FCC), minimum noise fraction (MNF), band rationing (BR), band math (BM), mineral indices (MI), relative absorption band depth (RBD), and constrained energy minimization (CEM). The majority of the composites generated through these techniques exhibit greyscale coloration. In order to enhance visualization and facilitate correlation for hydrothermal alteration mapping, colored ramps were devised from the gray-scale images. The implemented approach in the current study is designed as a flowchart in Fig. 4. To ensure the reliability of our findings, our research focused on detecting hydrothermal alteration patterns within the study area using

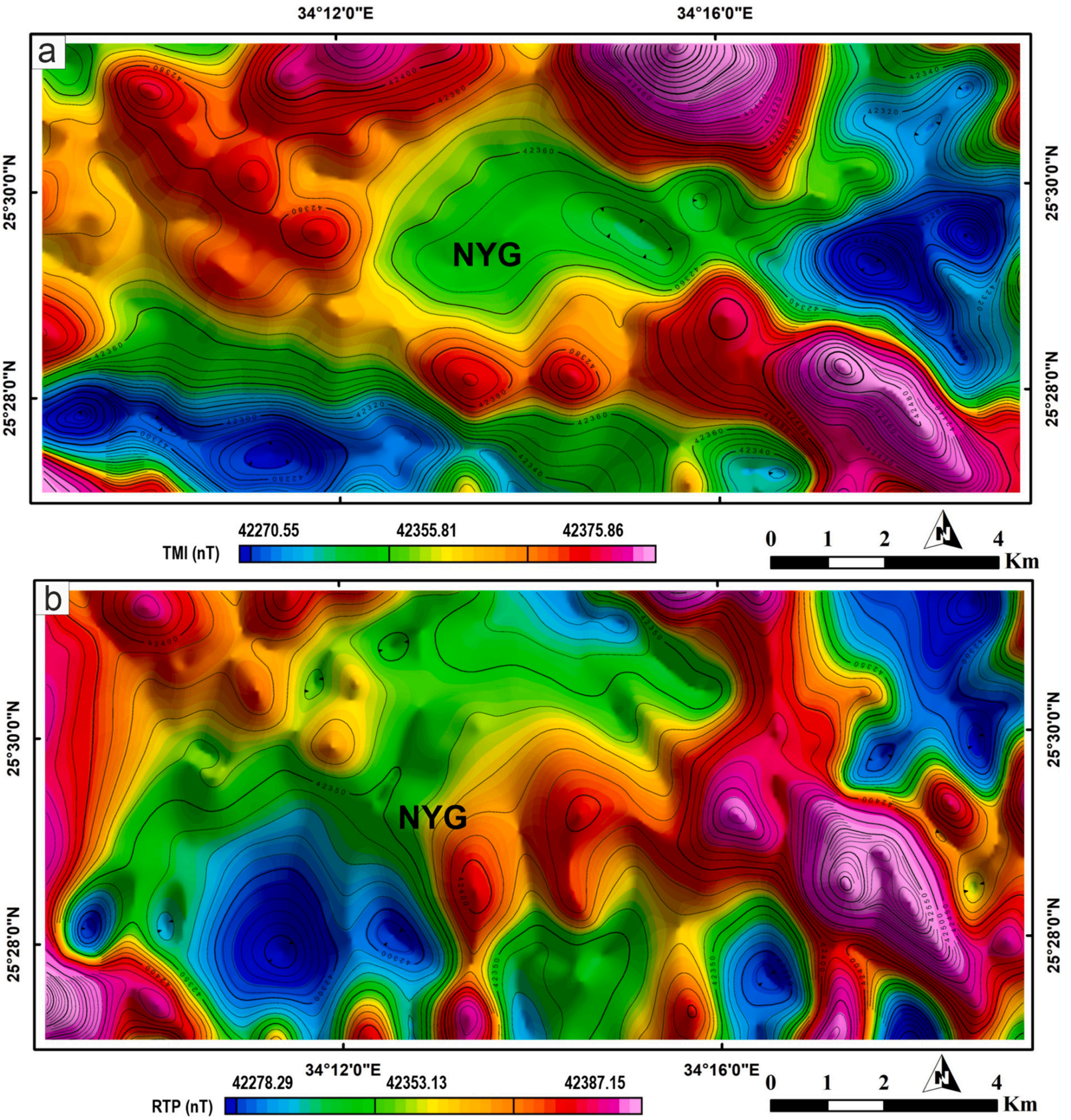

Fig. 3. Aeromagnetic data (a) TMI shaded relief map, and (b) RTP shaded relief map of the study area.

widely-approved band combinations across different multispectral sensors supplemented by geophysical data and field investigations. Given the complexity and variability of the terrain's hydrothermal alterations, machine learning algorithms were not employed in this study as they often provide thematic classifications based solely on pixel values without adequate consideration of the regional geological context necessary for accurate interpretation. Instead, our approach utilized specific band indices to differentiate alteration types, allowing for a more nuanced interpretation informed by field observations and the broader geological context of the area. All the utilized techniques are summarized in Appendix A.

3.3.1.1. False color composites. The FCC technique is widely employed in remote sensing and satellite imagery analysis for several purposes such as lithological and hydrothermal alteration mapping (Anwar et al., 2023; Dawoud et al., 2023; Fahmy et al., 2023a; Fahmy et al., 2023b; Meyyappan and Brijesh, 2022; Ousmanou et al., 2023; Shebl et al., 2023a). The FCC technique enables allocating three types of information (e.g., spectral bands) to the primary red, green, and blue (RGB) channels. It facilitates the visualization of multichannel images as a result of color and texture variations based on the values in their spectral single channels, leading to a more accurate interpretation (Abdelkader et al., 2022; Pohl and van Genderen, 2014; Shebl et al., 2023a; Shebl et al., 2021). Consequently, they effectively improve the discrimination of lithological units, minerals, and areas of alteration by utilizing specific spectral properties (Bajwa et al., 2020; Bety, 2022; Qari et al., 2008; Salem et al., 2016). The current study utilizes the proposed VNIR-SWIR Sentinel 2 FCC of b6-b2-b12 in RGB and SWIR ASTER FCC of b9-b8-b5 in RGB to better discriminate the exposed rocks in the study area and subsequently facilitate the correlation of different types of alteration with their respective lithologies.

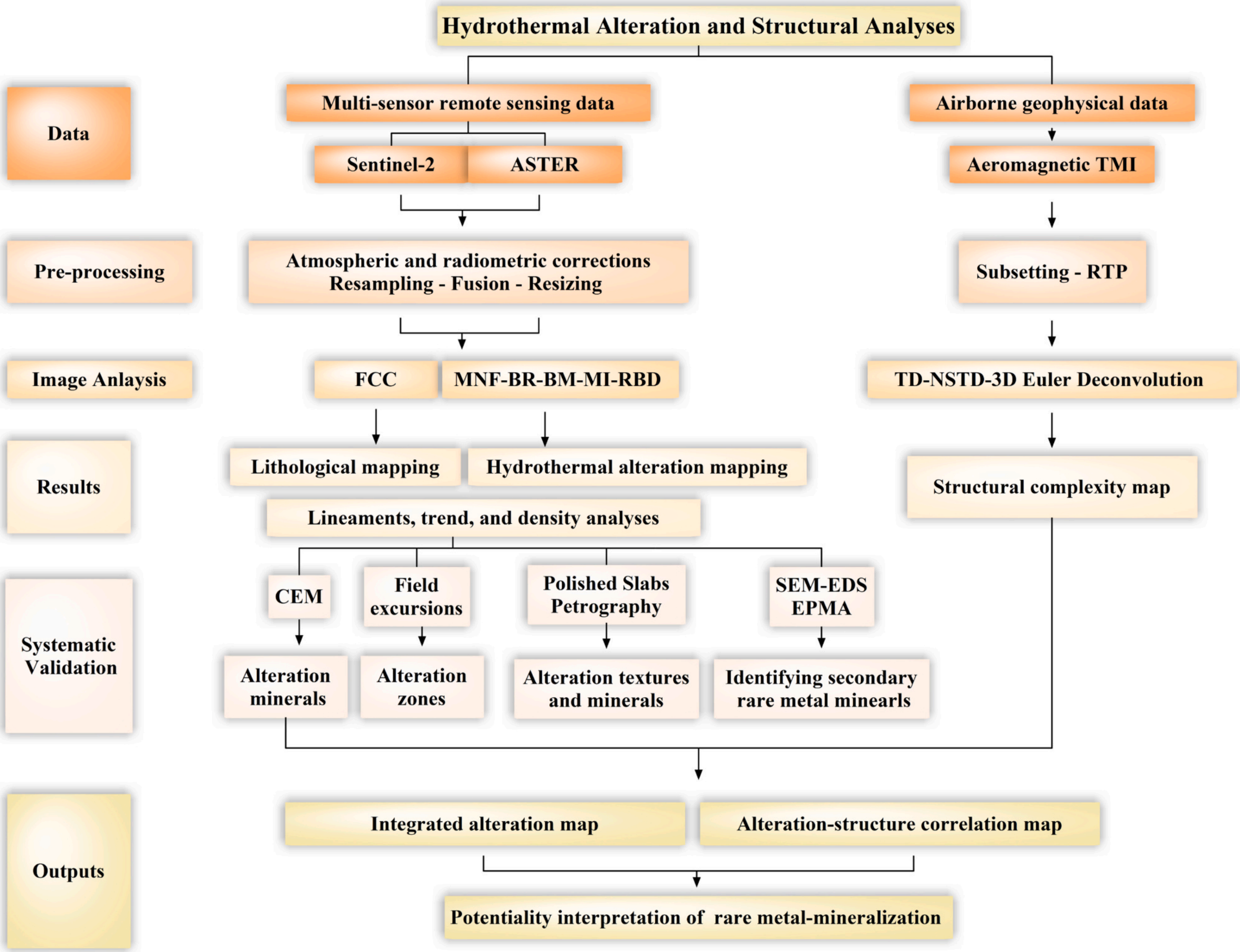

Fig. 4. Flowchart showing the adopted methodology in the current study.

3.3.1.2. Minimum noise fraction. Minimum noise fraction is a commonly utilized technique in image processing for enhancing the identification and mapping of subtle spectral variations, including hydrothermal alterations (Abdelkader et al., 2022; Mahanta and Maiti, 2022; Niyeh et al., n.d.; Pazand and Pazand, 2022; Rani et al., 2022; Shebl and Hamdy, 2023). It was frequently employed to assess the inherent dimensionality, segregate noise in the image data, and condense the computing requirements for succeeding analysis (Abdelkader et al., 2022; Ducart et al., 2016; Green et al., 1988; Shebl et al., 2023a; Shebl et al., 2023b). The MNF employs a preliminary transformation to condense the most significant data into a limited number of spectral bands, with the most relevant bands appearing first (Denghui and Le, 2011; Sayed et al., 2023; Xi et al., 2022). This study uses MNF linear transform in noise whitening, extracting key features, and reduction of spectral data. Particularly, utilizing the MNF3-MNF1-MNF2 components following Sentinel 2 transformation is beneficial in identifying distinct alteration types.

3.3.1.3. Band rationing, band math, and mineral indices. Through the literature, numerous band ratios were widely utilized and refined for mapping hydrothermal alterations and enhancing the variance in spectral signatures of their associated minerals while mitigating the influence of topographical factors and solar illumination. (Aisabokhae and Tampul, 2019; Badawi et al., 2023; El-Desoky et al., 2022a; Fotze et al., 2019; Frutuoso et al., 2021; Holben and Justice, 1981; Osinowo et al., 2021; Pour et al., 2018; Shebl et al., 2023b). Band ratios, band math, and mineral indices involve performing basic arithmetic computations on various bands, allowing for semi-quantitative analysis of the prevalence and intensity of specific absorption or reflectance features (Sabins Jr and Ellis, 2020). Specifically, BR involves dividing one band's digital number value by another's digital number value. Consequently, BR, BM, and MI are effectively employed in digital image processing to visualize and analyze variations in spectral characteristics. The current study employed various BR, BM, and MI to highlight the altered rock units and classify their alteration type and secondary minerals. The implementation of several band rationing computations resulted in the identification of the optimal combinations of band ratios as (b4/b11,b4/b3, and b11/b12) for Sentinel 2 proposed and utilized by Shebl et al. (2023a), and (b2/b1, b5/b3 + b1/b2, b4/b3, b4/b6, b7/b6*b4/b6, b5/b4, b7/b5, b4/b5*b8/b6, b9/b5*b7/b8, b7/b6, and b7/b6*b4/b6) for ASTER images, proposed and utilized by Ninomiya (2003a, 2003b), Ninomiya et al. (2005), Pour et al. (2019b), Shebl et al. (2023a), Van der Meer et al. (2014) and Van der Meer et al. (2012), to be effective in highlighting different types of hydrothermal alterations. All of these expressions are tabulated in Appendix A.

3.3.1.4. Relative absorption band depth. The relative absorption band depth can highlight the spectral differences between altered and non-altered rocks (Abdelkader et al., 2022; Alarifi et al., 2022; Canbaz, 2023; El-Desoky et al., 2022a; Niyeh et al., n.d.; Saed et al., 2022; Shebl et al., 2023a). In order to determine the RBD, the numerator of the calculation involves the summation of the bands that enhance the shoulder of an absorption feature (Crowley et al., 1989). Conversely, the denominator is the band closest to the absorption feature (Crowley et al., 1989; Mars and Rowan, 2006). ASTER [(b4 + b7)/b6] and [(b5 + b7)/b6] and [(b7 + b9)/b8] images have been applied in previous studies to delineate propylitic, phyllic, and argillic mineral assemblages implementing SWIR data (Rowan and Mars, 2003; Shebl et al., 2023a). Specifically, the current study calculated the ASTER RBD of [(b5 + b7)/b6], proposed by Mars and Rowan (2006) and Rowan and Mars (2003), to highlight the OH-bearing alteration.

3.3.1.5. Constrained energy minimization. The CEM method is a linear spectral approach widely utilized for mapping mineral intensity levels (Alarifi et al., 2022; Ali et al., 2023; Atif et al., 2022; El-Desoky et al., 2023; El-Desoky et al., 2022a; Mahdi et al., 2022; Ousmanou et al., 2023; Shebl and Hamdy, 2023). The CEM amplifies the response of the known end member (target alteration mineral) using the partial unmixing matrix and minimizes the response of the composite unknown background (gangue minerals), thus correlating and highlighting the reference and target signatures (Farrand and Harsanyi, 1997; Harsanyi, 1993; Pour et al., 2019a; Shebl et al., 2021). The results of the CEM analysis are represented by a set of gray-scale images, with each image corresponding to a specific end member selected for analysis. The CEM possesses the advantage of being a straightforward method that can be employed to map the alteration zones. Epidote, muscovite, hematite, Ilmenite, calcite, albite, chlorite, kaolinite, sericite, illite, and alunite are considered markers for the distinct types of alterations (e.g., alkali metasomatism, Ferrugination, argillic, phyllic, and propylitic) within various hydrothermal systems (Abdelkader et al., 2022; Beygi et al., 2021; Mars and Rowan, 2006; Pour and Hashim, 2012; Zamyad et al., 2019). Identifying and differentiating targeted alteration minerals in the study area using CEM were conducted using the USGS spectral library through the ENVI software and ASTER data.

3.3.1.6. Structural lineaments extraction. Automated methodologies for lineament extraction have been acknowledged for their capacity to achieve reproducibility and enhance efficiency (El-Desoky et al., 2022b; Shebl and Csámer, 2021; Weerasekara et al., 2014). Moreover, geological structures have a crucial role in tracing the development of mineral deposits (Badawi et al., 2023; Beygi et al., 2021; Bishta et al., 2014; Gabr et al., 2022; Ibrahim, 2013; Megwara and Udensi, 2014; Salawu et al., 2023; Sayed et al., 2023). These structural features can be accurately mapped at a regional level using several spatial data sources. This study used the first principal component of Sentinel 2 data (Sentinel 2 PC1) to extract linear or curvilinear edges successfully by employing the edge enhancement "LINE" extraction algorithm tool incorporated within the PCI Geomatics software package (version 2016) (Gabr et al., 2022; Ghoneim et al., 2022; Hung et al., 2003; Shebl and Csámer, 2021). The "Line" algorithm encompasses the processes of thresholding, edge detection, and curve extraction to extract lineaments from any single 8-bit image (Abdelnasser et al., 2023; Bishta et al., 2014; Maged and Mazlan, 2010). The selection of Sentinel 2 was based on its superior spatial (ground) resolution, ability to amplify the response of structural elements of geological origin, and improvement of edge contrast and topographic variations (Hung et al., 2005; Immaculate et al., 2020). The algorithm utilizes pairs of parallel-facing and closed polylines regulated through pre-defined parameters (Appendix A). The initial procedure for automatic lineament extraction involves an experimental evaluation by employing several trial values for each variable within the LINE module to define the best values that give the most reliable results to visual inspection, manually extracted lineaments, and field data (Appendix A). The polylines have the potential to be extracted as a vector layer and subsequently integrated into the ArcGIS software, which is commonly employed for manual inspection of lineaments to remove erroneously-extracted wadi (valley) lines due to tonal contrast, density map creation, data analysis, and image layout finalization. Spatial and statistical analyses followed the lineament extraction, including orientation and frequency analysis using rose plots integrated into Rockworks software (version 16). Consequently, the Sentinel 2-PC1 component, which contains the most information, yielded extensive data, capturing the most variability of lineaments and enabling enhanced observation of small structural characteristics within the study area.

3.3.2. Airborne magnetic data processing techniques

3.3.2.1. Tilt derivative (TD). Commonly, derivatives of potential field data assist in identifying and estimating the physical properties of the source structures (e.g., shear zones, fractures, contacts, edges, faults) causing the anomaly. The tilt derivative is suitable and has distinct advantages over many conventional derivatives for mapping shallow structures, principally the edges of magnetic structures (zero contour line represents the contact location). The filter is described by Miller and Singh (1994) in Eq. (1) as

$$TD = tan^{-1}\left(\frac{\frac{\partial f}{\partial x}}{\sqrt{\left(\frac{\partial f}{\partial x}\right)^2 + \left(\frac{\partial f}{\partial y}\right)^2}}\right) \tag{1}$$

where $\frac{\partial f}{\partial x}$ is the first vertical and $\frac{\partial f}{\partial x}, \frac{\partial f}{\partial y}$ are horizontal derivatives of the magnetic field in the x and y directions, respectively. Since TD relies on the ratio of derivatives, large- and small-amplitude anomalies are well improved.

3.3.2.2. Normalized standard deviation (NSTD). Several techniques based on vertical or horizontal derivatives were suggested for mapping edges, faults, and contacts. The normalized standard deviation is one of these methods (Cooper and Cowan, 2008), which relies on the ratio of the windowed standard deviation of derivatives and is computed using Eq. (2).

$$NSTD = \frac{\sigma\left(\frac{\partial f}{\partial z}\right)}{\sigma\left(\frac{\partial f}{\partial x}\right) + \sigma\left(\frac{\partial f}{\partial y}\right) + \sigma\left(\frac{\partial f}{\partial z}\right)} \tag{2}$$

where f is the magnetic field in x, y, and z directions, and σ is the standard deviation computed utilizing a moving square window of data points.

3.3.2.3. 3D Euler deconvolution method. Euler deconvolution is a widely applied methodology in interpreting filed data to estimate the shape and depth of the causative sources (Reid et al., 1990). The homogeneity equation that Thompson (1982) obtained provides the base of 3D Euler deconvolution. It relates the geopotential field (aeromagnetic) and its gradient components to the source location. The usual Euler's formula is given in Eq. (3) as

$$(x - x_0)\frac{\partial F}{\partial x} + (y - y_0)\frac{\partial F}{\partial y} + (z - z_0)\frac{\partial F}{\partial z} = N(B - F), \tag{3}$$

where F is the measured field at (x, y, z) and x_0, y_0, z_0 are coordinates, N is the structural index, and B is the field base level.

3.3.3. Field and laboratory analyses

Comprehensive field observations were conducted through three excursions to the study area (September 2021, March 2023, and July 2023) to investigate the field relationships between various rock units (particularly the NYG pluton) and to understand the diverse alteration processes. This fieldwork also aimed to validate and approve the findings derived from our remote sensing and geophysical data analysis, verify the spatial distribution of hydrothermal alteration zones, and asses hydrothermal alteration mineral identification reliability through integrated multisource remote sensing and geophysical data. A GNSS

(Global Navigation Satellite System)-based inspection was conducted to accurately correlate the coordinates of the different field features and the collected samples. Field high-resolution photography (20 Megapixels) was employed to capture the attributes and characteristics of lithological units and hydrothermal alteration zones.

Over 60 samples from the Umm Naggat rare-metal granite and the alteration zones have been collected and sliced for hand specimen scanning and to investigate their microscopic primary-secondary mineral assemblages and alteration textures through petrographic analysis. Polished thin sections were prepared from fresh and altered samples and investigated using a conventional transmitted, reflected-light polarizing microscope. A subset of the thin sections was coated by a 15–20 μm thick carbon layer. Subsequently, the mutual textural relationship and mineralogical composition of alteration minerals and their related rare metals were identified and semi-quantitatively confirmed using a scanning electron microscope (JEOL JSM-IT300) equipped with an energy dispersive spectrometer housed at Akita University in Japan. The operating conditions for SEM-EDS were 15–20 Kev and 15 mm working distance.

Major element contents of biotite, muscovite, chlorite, and alteration-formed rare metal-bearing minerals in the Umm Naggat granites were quantitatively determined using an electron probe microanalyzer equipped with wavelength dispersive X-ray spectrometry (JEOL JXA-8230) housed at Akita University in Japan. Operating conditions were 15 kV accelerating voltage, 20 nA beam current, and 1–5 mm beam diameter. Natural and synthetic standards were used for calibration, and the raw data was corrected using oxide ZAF matrix correction. For major elements, the peak count time was 20 s, and the background time was 10 s; for trace elements, the corresponding times were 40–60 s and 20–30 s.

4. Results

4.1. Lithological mapping results

In this study, two FCCs were generated by employing Sentinel 2 and ASTER datasets. Producing these FCCs primarily aims to distinguish the predominant rock units within the Umm Naggat area by enhancing the detection of lithological contacts. Additionally, these FCCs were intended to provide guidance and a general outline for the subsequent hydrothermal alteration mapping. In order to obtain the highest level of discrimination, the selection of the RGB of FCC combinations is established on prior familiarity with the exposed rocks and their mineralogical composition that broadly directs their spectral behavior.

Sentinel 2 proposed VNIR-SWIR b6-b2-b12 have been assigned to the RGB channels to outline the major rock units in the study area (Appendix B). This FCC demonstrated the Sentinel 2 ability to demarcate both the geomorphological features and the overall geological framework. Through the previous Sentinel 2 FCC visual inspection, the NYG boundaries are sharply distinguished from the surroundings by a contrast signature in violet hue. The basement rocks surrounding the NYG exhibit a similar bluish-green hue, making them indistinguishable, except for the trachytes that are highlighted by brown coloration.

Subsequently, the SWIR b9-b8-b5 of ASTER was assigned in RGB to generate the second FCC image (Appendix B). ASTER FCC revealed an enhanced capability in distinguishing the exposed rocks with great spectral sensibility and improved details than Sentinel 2 owing to the sharper spectral resolution of ASTER. Therefore, it provides better discrimination results between various rock units with sharp contacts. For instance, the NYG was separated by a light brown color. At the same time, the neighboring rocks were characterized from each other by different colors owing to their different spectral characteristics. This ASTER band combination outlines the curved boundary contacts and the zonation within the NYG, which gradually transitions from a lighter brown hue (mafic-rich biotite granite) in the southern region to a darker brown shade (mafic-poor alkali feldspar granite) in the northern region. This color variation suggests a sequential process of late-stage magmatic differentiation. The metavolcanics exhibit a distinct blue color, whereas a prominent greyish-green coloration characterizes the metasedimentary rocks. Moreover, older granites, metagabbro-diorites, and serpentinites are separated by blackish-green color due to their analogous intermediate-mafic composition.

4.2. Hydrothermal alteration results

4.2.1. Na-metasomatism (albitization)

Spectrally informative MNF is implemented to investigate Na-rich alterations (albitization). MNF is crucial for accentuating specific spectral features that may not be readily discernible in FCC images. The execution of the RGB MNF2-MNF3-MNF1 was performed utilizing the Sentinel 2 dataset (Fig. 5a). The favorable selection of the first three components following the MNF transformation was governed by their substantial embedded information with less noise than subsequent components. For instance, the former MNF combination effectively highlights the zones of Na-metasomatism or albitization, which are visually represented by a striking sky-blue contrast. Albitization mainly occurs as a marginal alteration phase confined to the younger granites in the central part of the study area. It predominantly occurs as irregular patches along the outer boundaries of the NYG pluton. Occasionally, Na-alteration exhibits a linear trend following the NNW-trending fracture system within the NYG pluton (Fig. 5a). The analysis of the MNF transformation applied to the Sentinel 2 image emphasizes that this technique effectively detects albitized granitic rocks with high color contrasts and more accurate boundaries.

4.2.2. Fe-bearing alteration (ferrugination)

The outcomes obtained by the color ramp images for Fe-bearing alterations, Al-OH alteration, and Mg-Fe-OH alteration in the study area are classified into three alteration-intensity levels: low or weak, moderate, and high or strong. Various band ratios and mathematical band combinations were employed to effectively utilize ASTER and Sentinel 2 data for delineating Fe-bearing alteration and the associated minerals. Band rationing is the most efficient technique for delineating the abundance of iron oxides from Sentinel 2 and ASTER imagery in various parts of the study area. The absorption characteristics of iron hydroxide/oxide minerals exhibit notable distinctions throughout the wavelength range of 0.50 to 1.0 μm, which corresponds to band 1 (0.52–0.60) and band 2 (0.63–0.69 μm) of ASTER (Sekandari et al., 2022). Consequently, The ASTER's VNIR-SWIR combination (b4/b2 + b2/b1) was employed to analyze the iron oxides distribution (Fig. 5b). Iron-bearing alteration principally extends into the NYG pluton and the metavolcanics, exhibiting moderate to slightly strong concentrations (Fig. 5b). The NYG displays varying degrees of ferrugination, with the mafic-rich biotite granite in the southern region and the albitized granite in the northern region exhibiting moderate to strong levels of alteration. Furthermore, the mafic-poor alkali feldspar granite content exhibits areas of weak alteration as well as areas of strong alteration. Sentinel 2 and ASTER data were further utilized in order to classify the iron-bearing alteration into ferrous and ferric types.

4.2.2.1. Ferrous-bearing alteration. The band ratios of Sentinel 2 (b11/b4) and ASTER (b5/b3 + b1/b2) were utilized to extract ferrous-bearing minerals in the study area (El-Desoky et al., 2022a; Pour et al., 2019b; Shebl et al., 2023a; Van der Meer et al., 2014; Van der Meer et al., 2012). Sentinel 2 BR of (b11/b4) discriminates the exposed rock units into ferrous-rich and ferrous-poor (Fig. 5c). The majority of ferrous iron-rich zones are found in the younger granites (BTG-ABG) and metavolcanics. On the other hand, older granites, metagabbro-diorites, serpentinites, and metasedimentary rocks exhibit lower quantities of ferrous minerals. Locally, the NYG pluton shows variable ferrous alteration ranging from extremely weak (blue color) to extremely strong (brown color). The AFG

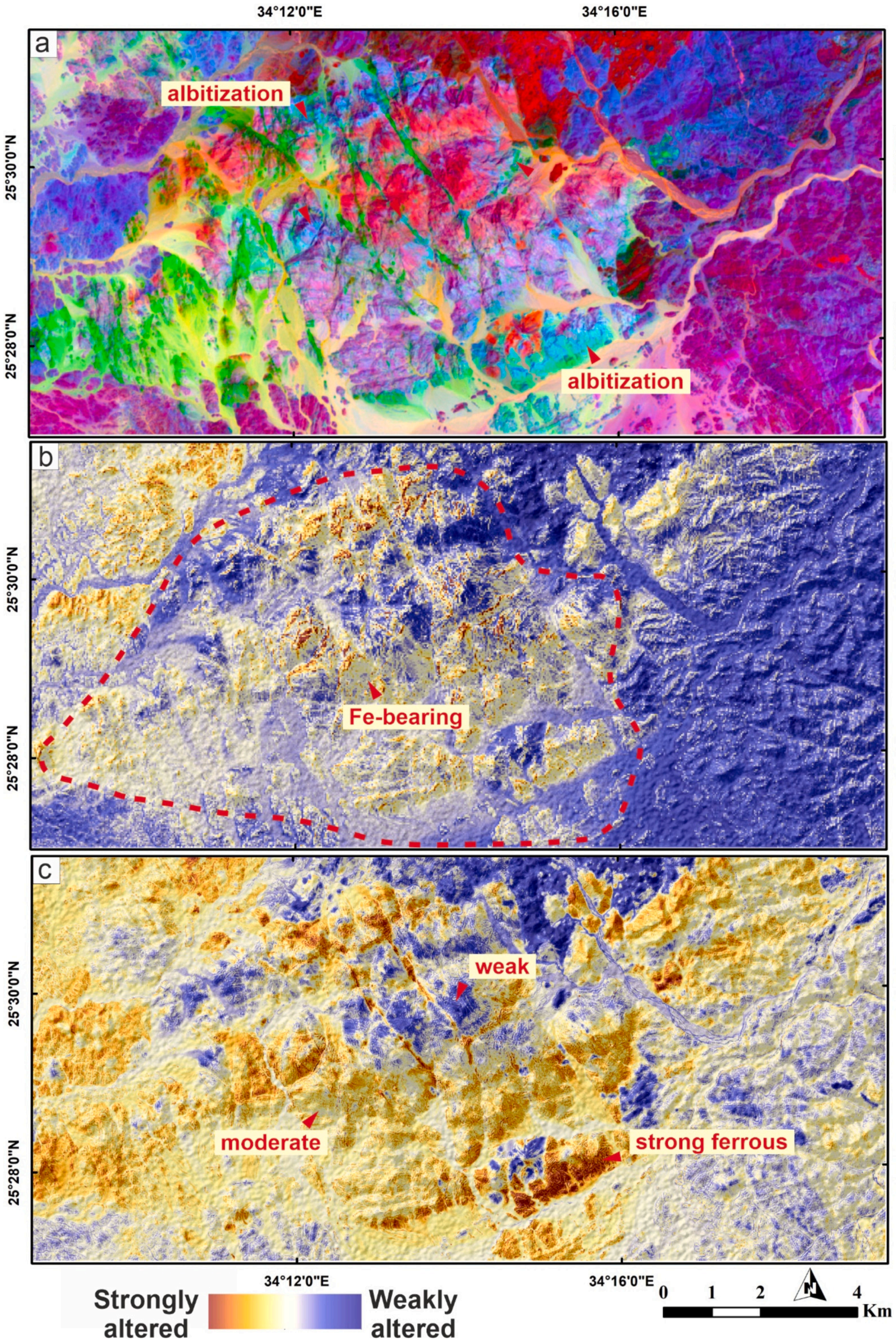

Fig. 5. (a) Albitization mapping utilizing the Sentinel 2 MNF2-MNF3-MNF1, (b) color ramp showing the overall Fe-bearing alteration utilizing ASTER combination of (b4/b2 + b2/b1), the dashed red line shows the boundaries of the NYG pluton, and (c) color ramp showing the ferrous-bearing alteration utilizing Sentinel 2 band ratio of (b11/b4). Weak, moderate, and strong refer to the degree of alteration intensity. (For interpretation of the references to color in this figure legend, the reader is referred to the web version of this article.)

demonstrates minimal ferrous alteration within the pluton (dark blue color) (Fig. 5c).

In comparison, the mafic-rich biotite granite and the albitized granites display varying degrees of iron-bearing signatures, ranging from moderate (yellow) to strong (brown). Notably, the southern peripheries of the BTG exhibit pronounced stronger intensities of ferrous alteration (extremely dark brown). Certain instances characterized by elevated levels of ferrous concentrations have a linear extension, traversing both the ABG and the AFG in the NNW direction (as shown by dark brown mesh-like fractures crossing from BTF through AFG to ABG). Moreover, the distribution of ferrous-bearing alteration throughout the metavolcanics exhibits a lack of uniformity. Metavolcanic rocks largely show moderate levels of ferrous minerals, occasionally disturbed by irregular patches of low-ferrous concentrations (Fig. 5c).

Additionally, the VNIR-SWIR (b5/b3 + b1/b2) combination of ASTER yields comparable allocation outcomes for the ferrous-bearing altered rocks to the Sentinel 2 band ratio, thus confirming the validity of the obtained mapping (Fig. 6a). Similar to Sentinel 2, the ASTER combination defines the NYG as exhibiting a weak to moderate degrees of ferrous alteration. This ferrous alteration is spatially associated with the two ends of the NYG: the mafic-rich biotite granite and the albitized granite. In contrast to Sentinel 2 results, the western outcrop of the BTG shows very weak ferrous alteration. At the same time, older granites exhibit moderate concentrations of ferrous minerals. Metasedimentary rocks, metagabbro-diorites, and serpentines were differentiated into weakly-altered and moderately-altered patches. Moreover, ASTER (b5/b3 + b1/b2) highlights the metavolcanics in the northeastern and northwestern in deep brown color, indicating their high-ferrous content. Conversely, the metavolcanics in the southeastern area display intermediate quantities of ferrous iron.

4.2.2.2. Ferric-bearing Alteration. In order to demarcate the ferric iron alteration, Sentinel 2 (b4/b3) and ASTER (b2/b1) VNIR band ratios were applied (Pour et al., 2019b; Shebl et al., 2023a; Van der Meer et al., 2014; Van der Meer et al., 2012). These combinations show concordant results regarding the ground distribution and intensities of the ferric-bearing minerals. Visual inspection of the two Sentinel 2 and ASTER color ramps (Fig. 6b, c, respectively) demonstrate the prominent prevalence of ferric-bearing alteration limitedly in the NYG pluton. Simultaneously, most country rocks exhibit no ferric alteration, including metavolcanics, older granites, metasedimentary rocks, serpentinites, and metagabbro-diorites.

Within the NYG, the western outcrop of the biotite granite displays the peak density of ferric-related minerals in both Sentinel 2 and ASTER outcomes, evidenced by the dark brown coloration. The Sentinel 2 VNIR (b4/b3) (Fig. 6b) demonstrates superior precision and efficacy when compared to ASTER in differentiating the main body of the NYG pluton according to their relative content of ferric alteration. The mafic-rich biotite granite, which represents the southern portion of the pluton, exhibits a higher level of ferric enrichment compared to the mafic-poor alkali feldspar granite and albitized granite, which comprise the northern half. Biotite granite shows moderate to extensively high ferric character, whereas the AFG and ABG exhibit weak signs of ferric alteration.

Despite the band ratio of ASTER VNIR (b2/b1) (Fig. 6c) showing similar overall ferric characterization to the Sentinel 2 of the NYG, the distribution pattern of ferric alteration is locally inconsistent. Since ASTER has a lower spectral resolution than Sentinel 2 in the VNIR region, the ferric distribution pattern resulting from ASTER is not uniform. The NYG demonstrates irregular concentrations of ferric-bearing alteration ranging from significantly low to slightly high. Generally, the consistent results between Sentinel 2 and ASTER (with acceptable differences) validate the results and confirm the superiority of Sentinel 2 in mapping alterations with distinct absorption characteristics in the VNIR region.

4.2.3. OH-bearing Alteration

In order to accurately delineate the broad framework of the OH-bearing alteration, two ratio images, Sentinel 2 (b11/b12) (Fig. 7a) and ASTER (b4/b6) (Fig. 7b), were implemented using SWIR bands. These ratios were utilized to improve the spectral contrast of absorption-reflectance anomalies specific to OH-bearing minerals. Focusing on the selected SWIR bands helped to mitigate the impact of shadow effects resulting from variations in solar illumination due to the rugged topography of the various rock units in the study area, especially BTG, AFG, and ABG (Hewson et al., 2006; Ninomiya et al., 2005; Sengar et al., 2020). Coinciding with Pour et al. (2019b); Shebl et al. (2023a), the two ratio images show similar results, highlighting that most of the OH-bearing alterations are confined to the Umm Naggat younger granite pluton (Fig. 7a, b). The hydroxyl-bearing alterations exhibit a predominant occurrence as linear trends that intersect with one another in NW-NNW-WNW-NNE directions. Several occurrences of hydroxyl-bearing alteration are prominently observed towards the East along the contact boundary between the NYG and the adjacent metavolcanics (Fig. 7a). Both the ASTER and Sentinel 2 images demonstrate the classification of the metavolcanics and country rocks as weakly OH-altered.

The ASTER BR image provides a more precise demarcation of OH-alteration compared to the Sentinel 2 image (Fig. 7a, b). For instance, the NYG pluton exhibits moderate to strong OH alteration in the ASTER image, while it is classified as weakly- to strongly- altered in Sentinel 2. Furthermore, the ASTER image reveals the presence of irregular patches containing OH-bearing minerals along the southern boundary of the BTG, which are not discernible in the Sentinel 2 image. Utilizing ASTER, further detailed discrimination of different OH-alteration types, such as propylitic, Phyllic, and argillic, is facilitated due to the sufficient spectral resolution of ASTER in the SWIR region (Rowan and Mars, 2003) and the previously demonstrated superior performance over Sentinel 2 data.

4.2.3.1. Propylitic Fe-Mg-OH-bearing alteration and ferrous silicates. Alteration mapping outcomes demonstrate the reliability of utilizing the ASTER SWIR band math (b5/b4 + b9/b8) to generate spectrally-enhanced images that identify Fe-Mg-OH enriched minerals, indicating propylitic alteration. Additionally, the former combination effectively detects ferrous silicate minerals associated with propylitic and potassic alterations, such as chlorite, epidote, amphibole, and biotite (Shebl et al., 2023a; Van der Meer et al., 2014). The common minerals of the Mg-Fe-OH group (epidote, chlorite, biotite, and amphibole) display their diagnostic spectral features around 2.33 μm and 2.166 μm (Ninomiya et al., 2005; Pour et al., 2019b; Sengar et al., 2020). Particularly, the maximum reflectance feature associated with these minerals is located within the range of bands 5, 6, and 9. In contrast, band 8 (2.295–2.365 μm) displays an intense absorption feature (Ninomiya et al., 2005; Pour et al., 2019b; Sengar et al., 2020).

The color ramp image obtained from ASTER SWIR (b5/b4 + b9/b8) effectively distinguishes the Mg-OH and ferrous silicate-bearing alteration, uniquely characterizing the propylitic alteration zone (Fig. 7c). In the Umm Naggat area, the propylitic and ferrous silicate zone has largely developed in the central NYG pluton. Also, the wall rocks surrounding the pluton represent a broad propylitic and ferrous silicate zone distributing an outward semi-circular pattern around the NYG pluton. The predominant alteration minerals of the propylitic zone are mainly chlorite, followed by epidote, along with other ferrous silicate minerals such as biotite.

Furthermore, the visual analysis of Fe-Mg-OH alteration within the studied area reveals a lack of discernible spatial patterns. The distribution of alteration is characterized by uneven patterns with different intensities extending across a significant portion of the Umm Naggat region ramp, indicating that a substantial area of the exposed rocks had undergone propylitic alteration (Fig. 7c). Mapping results using (b5/b4 + b9/b8) of ASTER SWIR bands highlight the spatial distribution of a strongly developed propylitic alteration zone in the metavolcanics, older granites, and serpentinites where the alteration is more intensive and less scattered. In contrast, the NYG exhibits varying degrees of iron-magnesium hydroxide (Fe-Mg-OH) alteration, ranging from weak to strong, which is comparatively less extensive and more dispersed than the metavolcanic rocks. Significantly, results show a decrease in the density of Fe-Mg-OH minerals when proceeding from the southern region, characterized by mafic-rich biotite granite, towards the northern region, characterized by mafic-poor alkali feldspar granite and albitized granite. This observation provides evidence for the spatial and spectral correlation between the occurrence of the mafic-rich biotite granite in

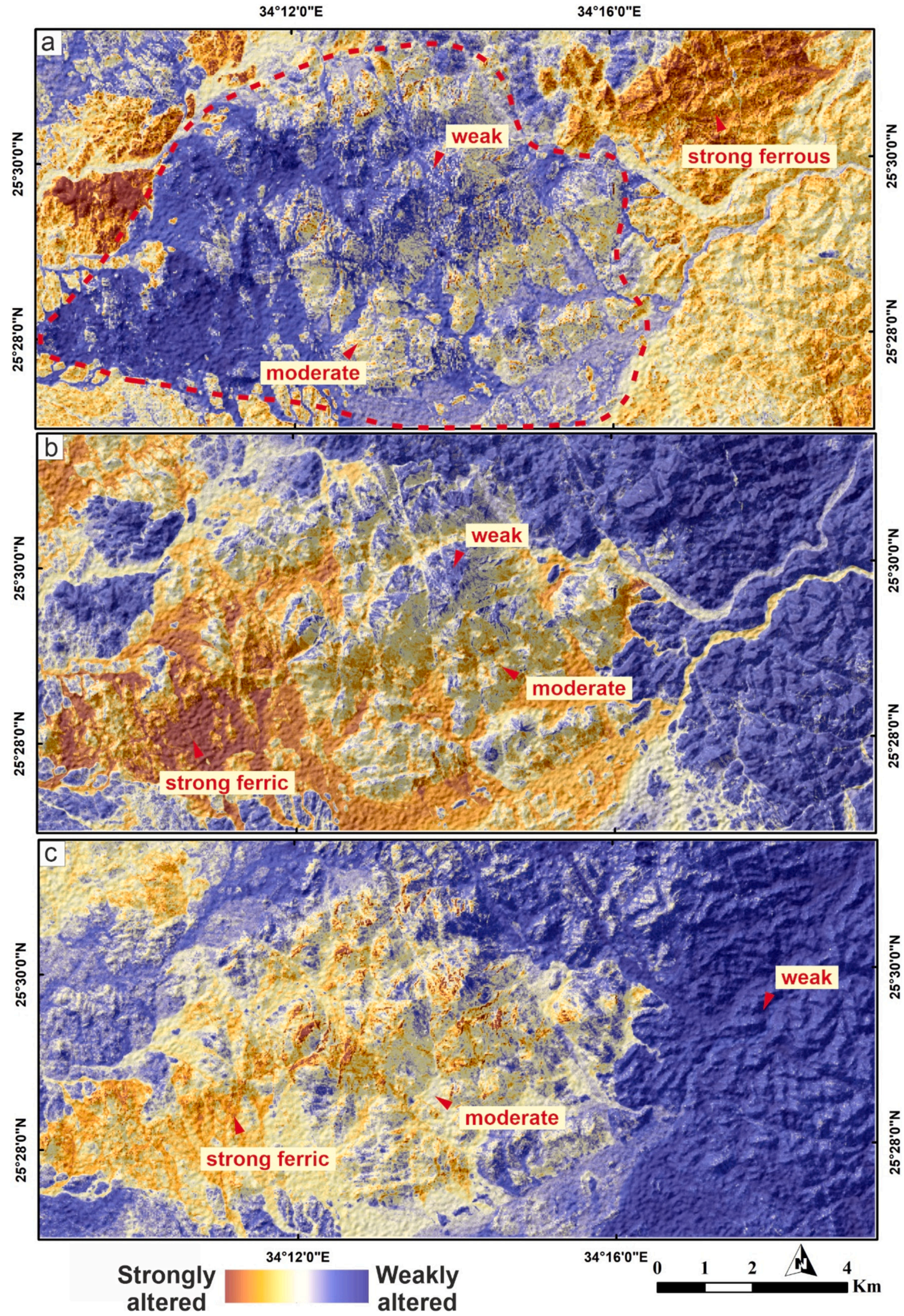

Fig. 6. Color ramps showing the spatial distribution and intensity variations of (a) ferrous-bearing alteration utilizing ASTER combination of (b5/b3 + b1/b2), (b) ferric-bearing alteration utilizing Sentinel 2 band ratio of (b4/b3), and (c) ferric-bearing alteration utilizing ASTER band ratio of (b2/b1). (For interpretation of the references to color in this figure legend, the reader is referred to the web version of this article.)

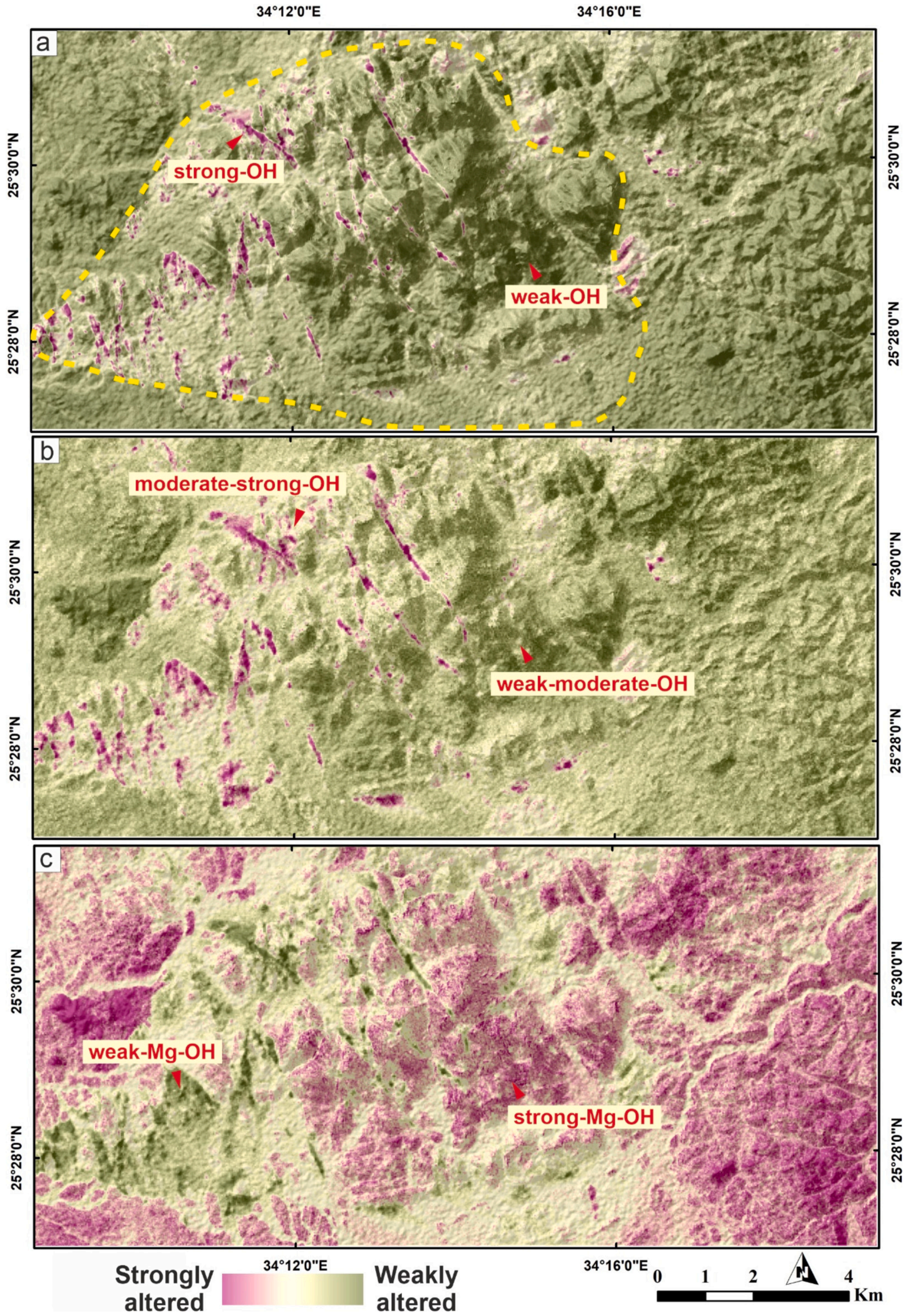

Fig. 7. Color ramps showing the spatial distribution and intensity variations of (a) OH-bearing alteration utilizing Sentinel 2 band ratio of (b11/b12), (b) OH-bearing alteration utilizing ASTER band ratio of (b4/b6), and (c) propylitic and ferrous silicates-bearing alterations utilizing ASTER band ration of (b5/b4 + b9/b8). (For interpretation of the references to color in this figure legend, the reader is referred to the web version of this article.)

the southern region and the concentration of the Mg-Fe-OH minerals and, consequently, the intensity of the propylitic and ferrous silicate alteration.

Additionally, the peripheries of the NYG exhibit a relatively lower degree of alteration. In contrast, the density of propylitic alteration tends to intensify towards the core of the pluton. Towards the East, the metasedimentary rocks mostly exhibit a modest propylitic alteration, whereas the metagabbro-diorites reveal a weak to moderate intensity of propylitic alteration. The observed association (alteration density-rock type) demonstrates the congruity between the geological data collected in the field and the mapping outcomes derived from remote sensing data.

4.2.3.2. Argillic Al-OH-bearing alteration. The most prominent minerals in argillic and phyllic alteration zones are alunite, kaolinite, illite, sericite, and muscovite. Al-OH minerals demonstrate a distinct spectral absorption characteristic at a wavelength of 2.205 μm, which may be observed in the ASTER band 6 (ranging from 2.235 to 2.285 μm). However, a narrower absorption characteristic at 2.165 μm, located within band 5 (ranging from 2.145 to 2.185 μm), discriminates kaolinite from other Al-OH minerals (Appendix C) (Pour et al., 2019a; Sengar et al., 2020). Band ratios, mineral indices, and RBD are applied to classify argillic and phyllic alteration zones, utilizing SWIR bands of ASTER data.

The diagnostic spectral characteristics of argillic minerals, such as kaolinite and alunite, serve as the basis for mapping argillic alteration. Argillic minerals exhibit pronounced reflectance characteristics in the wavelength range of band 4 (1.60–1.70 μm), while they demonstrate

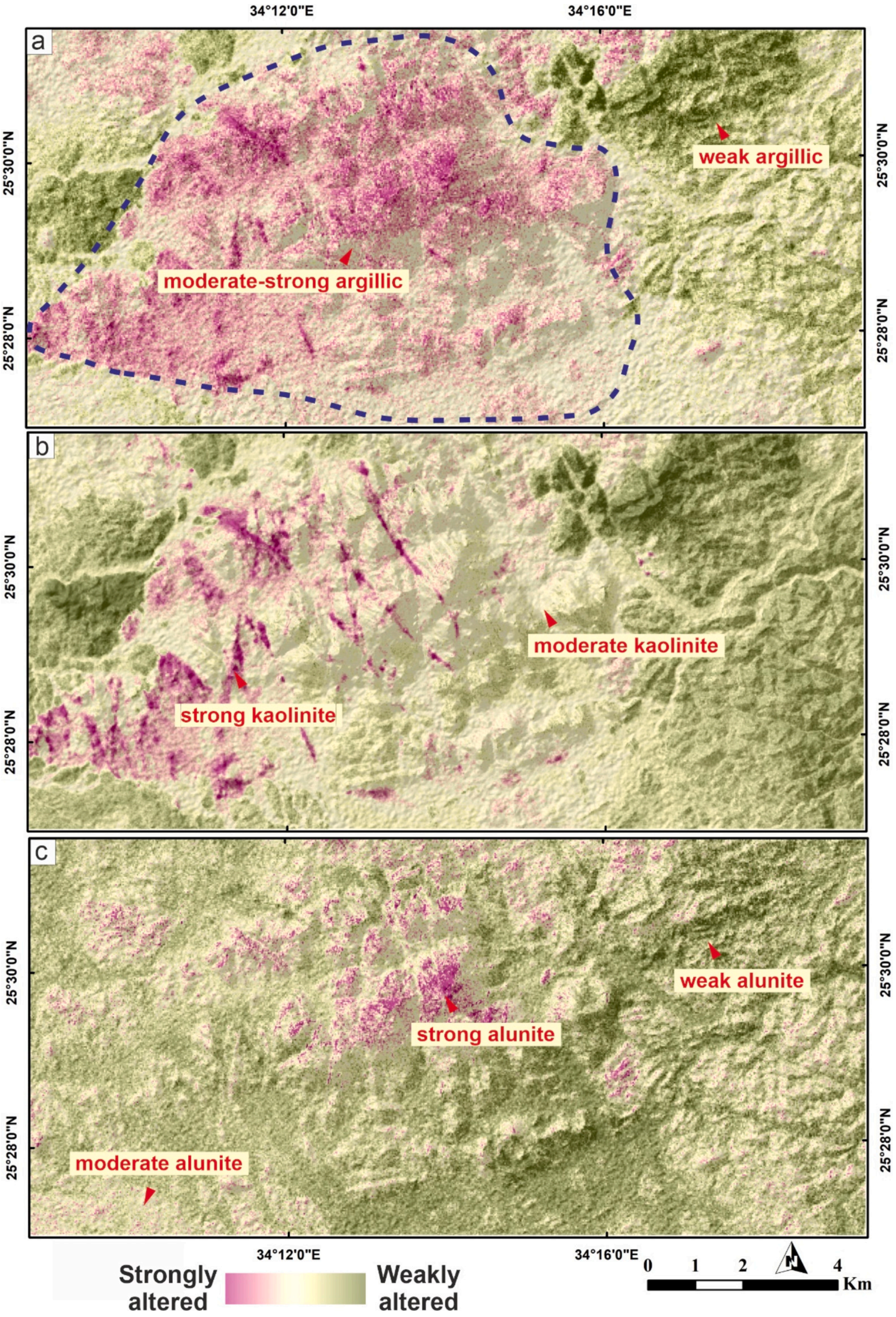

Fig. 8. Color ramps showing the spatial distribution and intensity variations of (a) argillic alteration utilizing ASTER band ratio of (b7/b5), (b) kaolinitic alteration utilizing ASTER kaolinite index of [(b4/b5) * (b8/b6)], and (c) alunitic alteration utilizing ASTER alunite index of [(b9/b5) * (b7/b8)]. (For interpretation of the references to color in this figure legend, the reader is referred to the web version of this article.)

significant absorption features in the wavelength ranges of band 5 (2.145–2.185 μm) (Mars and Rowan, 2006; Rowan and Mars, 2003; Sengar et al., 2020). Consequently, ASTER band ratio (b7/b5), kaolinite index (KLI) [(b4/b5) * (b8/b6)], and alunite index (ALI) [(b9/b5) * (b7/b8)], proposed by Ninomiya (2003a, 2003b), were selected to emphasize the occurrence of argillic alteration and to delineate the distribution of its associated Al-OH minerals especially kaolinite and alunite (Fig. 8).

The SWIR band ratio of ASTER (b7/b5) distinguishes the general argillic alteration zones, characterized by their irregular shapes and indistinct borders (Fig. 8a). Argillic zones are primarily restricted to the NYG pluton and its interfaces with the surrounding country rocks, particularly the metasedimentary rocks (Fig. 8a). The argillic alteration density exhibits a gradual decrease from the northern region (ABG + AFG) to the southern region (BTG) within the NYG. Towards the South, older granites are characterized by moderate degrees of argillic alteration. On the other hand, metavolcanics, serpentinites, and metagabbrodiorites exhibit inconstant argillic alteration fluctuating from weak to moderate (Fig. 8a).

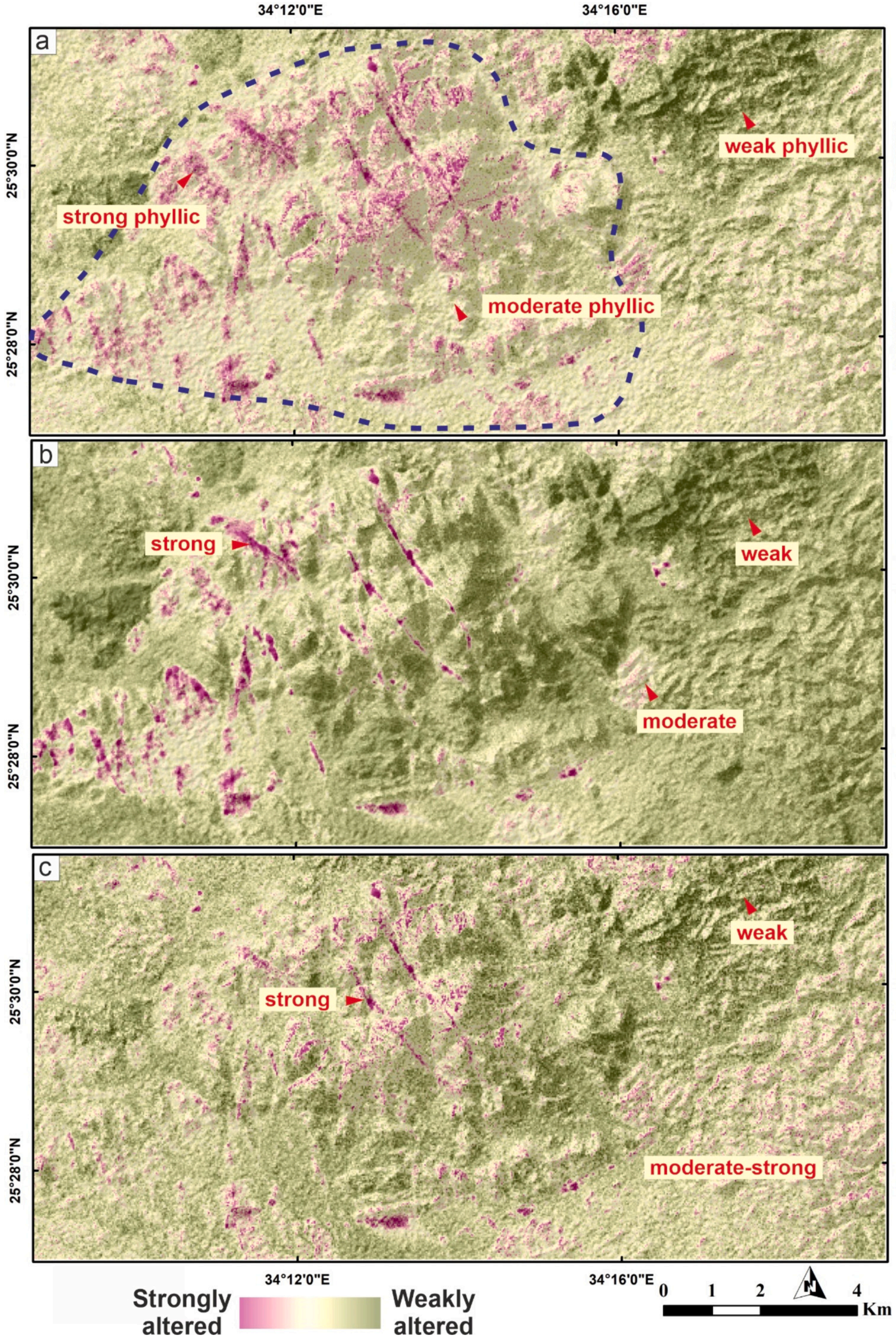

Fig. 9. Color ramps showing the spatial distribution and intensity variations of phyllic alteration utilizing ASTER (a) band ratio of (b7/b6), (b) phyllic OH-index of [(b7/b6) * (b4/b6)], and (c) RBD of [(b5 + b7)/b6]. (For interpretation of the references to color in this figure legend, the reader is referred to the web version of this article.)

A reasonable allocation of argillic Al-OH minerals is further distinguished regarding the different lithologies. For instance, the identification of kaolinite is achieved through the utilization of the KLI employing ASTER SWIR bands [(b4/b5) * (b8/b6)] (Fig. 8b). Kaolinite widely covers the extensively weathered NYG pluton in the central part of the study area with variable intensities. Generally, the whole NYG pluton is characterized by a moderate-kaolinitic alteration with a gradual decrease in the abundance of kaolinite towards the mafic-rich biotite granite in the South (Fig. 8b). In contrast, the stronger phase of Al-OH kaolinitic alteration occurs as subparallel linear alterations cut through the albitized granites, mafic-poor alkali feldspar granite, and extending to the western outcrop biotite granite. The kaolinite linear pattern exhibits NNW-NW-NNE-NE directions, suggesting that the structure and fracture systems in the study area might control kaolinitic alteration. Minor occurrences of kaolinite, with strong density, are dispersed along the outer southern peripheries of the NYG (Fig. 8b). The majority of country rocks display a notable absence (very weak) in kaolinitic alteration, except for the metasedimentary rock, which demonstrates a moderate to a high level of kaolinitic alteration intensities.

Moreover, the delineation of alunite is conducted by employing [(b9/b5) * (b7/b8)] ASTER shortwave infrared index (Fig. 8c). Compared to kaolinite, alunite demonstrates a limited occurrence clustering inside the northern part of the NYG and the metasedimentary rocks. Alunite displays a dispersed and non-uniform distribution characterized by varying levels of intensity. For instance, the ABG and AFG notably show moderate to strong alunite alteration. In contrast, the biotite granite is alunite-poor (Fig. 8b). Metavolcanics exhibit significant variations in alunite abundances, contingent upon their geographical distribution. In the eastern region, the metavolcanic rocks exhibit a range of alunite alteration from weak to moderate; however, in the western region, the alunite alteration varies from moderate to slightly strong. Unlike the propylitic alteration zone, the surface distribution pattern of the argillic alteration zone, kaolinite, and alunite is variable and mostly spatially correlates with the NYG in the central parts of the study area (Figs. 7c and 8).

4.2.3.3. Phyllic Al-OH-bearing alteration. The phyllic alteration zones are particularly important in geological exploration as they frequently accompany high-grade mineralization (Sillitoe, 2010). The spectral absorption characteristics indicative of the mineral assemblages in the phyllic zone, such as muscovite, illite, and sericite, are observed in the ASTER SWIR band 6 (Sengar et al., 2020). Consequently, several ASTER combinations, including band 6, were utilized, such as band ratio, mineral indices, and relative absorption band depth.

The ASTER band ratio (b7/b6) was employed to highlight the rock units displaying Phyllic alteration (Fig. 9a). The results differentiate the study area into two dissimilar groups characterized by varying levels of Phyllic alteration intensity: (1) the NYG and metasedimentary rocks and (2) metavolcanics, serpentinites, older granites, and metagabbro-diorites. The NYG and metasedimentary rocks primarily exhibit moderate concentrations of Phyllic alteration, which is overprinted by an irregularly distributed strong phyllic pattern (Fig. 9a). The most extensive phyllic alteration exhibits a non-uniform distribution within the ABG and AFG in the northern half of the NYG pluton. Furthermore, there is a noticeable decline in the strength of Phyllic alteration within the NYG as one moves from the northern (ABG + AFG) to the southern (BTG) regions (Fig. 9a). This transition is accompanied by an evolution from strong phyllic to moderate phyllic alteration, and ultimately culminating in weak phyllic alteration along the southern boundary of the NYG and metavolcanic rocks. Furthermore, metavolcanics, older granites, serpentinites, and metagabbro-diorites exhibit varying levels of phyllic alteration, ranging from significantly weak to moderate (Fig. 9a).

Several mineral indices (MI) have been established using logical band math operators to target the Phyllic Al/Fe–OH minerals more precisely. Ninomiya (2003b, 2004) proposed the utilization of the Phyllic OH-index (OHI_p) [(b7/b6) * (b4/b6)] to differentiate the Al/Fe–OH group minerals (sericite, muscovite, and illite) commonly associated with phyllic alterations (Fig. 9b). Detecting Al/Fe–OH-enriched minerals using OHI_p shows a more accurate allocation of the Phyllic alteration than the ASTER band ratio (b7/b6) (Fig. 9a, b). Strong phyllic alteration occurs as subparallel NNW-NNE-trending swarm-like patterns that limitedly occur in the northwestern part of the NYG pluton. Zones with extremely strong Phyllic alteration may suggest a convergence or coincidence of argillic and Phyllic Al-OH minerals (as depicted in Figs. 9b and 8b). The previously proposed overlapping issue is ascribed to the narrower absorption feature observed in ASTER band 5 for kaolinite and its deep absorption in band 6 (Appendix C). Consequently, kaolinite is often confused with other Al-OH group minerals, such as illite and muscovite, which are distinguished solely by their spectral absorption in band 6. Moreover, a few isolated occurrences of the biotite granite, metagabbro-diorites, and metasedimentary rocks, showing moderate Al/Fe–OH minerals, are scattered around the southern and the eastern part of the NYG. Metavolcanics, serpentinites, and older granites show no signs of Phyllic minerals (Fig. 9b).

The RBD is more efficient than the BR in mapping Fe/Al-OH distribution as it calculates the intensity of spectral absorption features for targeted minerals (Sengar et al., 2020). The RBD efficiently normalizes the illumination and atmospheric variances between the exposed rocks with different elevations, hence diagnosing the targeted alteration with higher accuracy. It is important to highlight that RBD can map a diverse array of hydrothermal alteration mineral associations; however, it cannot particularly identify a specific single mineral compared to spectral localization methods such as constrained energy minimization (Shebl et al., 2023a). Using ASTER SWIR, the RBD [(b5 + b7)/b6] was utilized to confirm the Phyllic alteration distribution previously highlighted by the BR and OHI_p (Fig. 9c). The alteration pattern resulting from RBD shows a more sporadically dispersed distribution than BR and OHI_p. According to the RBD, Phyllic alteration moderately to strongly overprints the albitized granite and the mafic-poor alkali feldspar granite towards the North of the NYG pluton.

On the other hand, the mafic-rich biotite granite demonstrates a rather limited occurrence of phyllic alteration, except for its southern peripheries, where a small number of localized, extensively altered areas may be observed (Fig. 9c). Metasedimentary rocks and metagabbro-diorites exhibit notable quantities of Al/Fe–OH minerals, ranging from moderate to high levels. Metavolcanics can be distinguished into two unique groups. The first group, located in the northeastern part of the study area, exhibits minor Phyllic alteration. Conversely, the second group, situated in the southeastern portion of the study area, displays moderate to high levels of Phyllic alteration (Fig. 9c). Hence, a resemblance can be observed in mapping Phyllic alteration using BR, OHI_p, and RBD regarding allocation. However, there are some variations in the distribution pattern and the intensity of Al/Fe-OH minerals exhibited by both methods (Fig. 9).

4.3. Structural analysis results

4.3.1. Structural framework from remote sensing data

Most lineaments are concentrated in the central part of the Umm Naggat area, with fracturing density decreasing outwards towards the borders. The lineaments mapping, including their occurrence, directions, and density in the study area, suggest lineaments have diverse orientations but mainly trend in the WNW-NNE NNW-NW-NE-ENE and N-S directions (Fig. 10a). The NYG exhibits the maximum number of structural lines and the closest spatial spacing relative to the country rocks (Fig. 10a). The heterogeneity in lineament directions indicates complex tectonic fabrics and structural systems in the Umm Naggat area, particularly the NYG pluton. The analysis of the rose diagram plot demonstrates the prevalence of the NNW, NW, and NNE fault-fracture pattern over other directions (Fig. 10a). The line density map classified the study area into low, medium, and high structural density zones

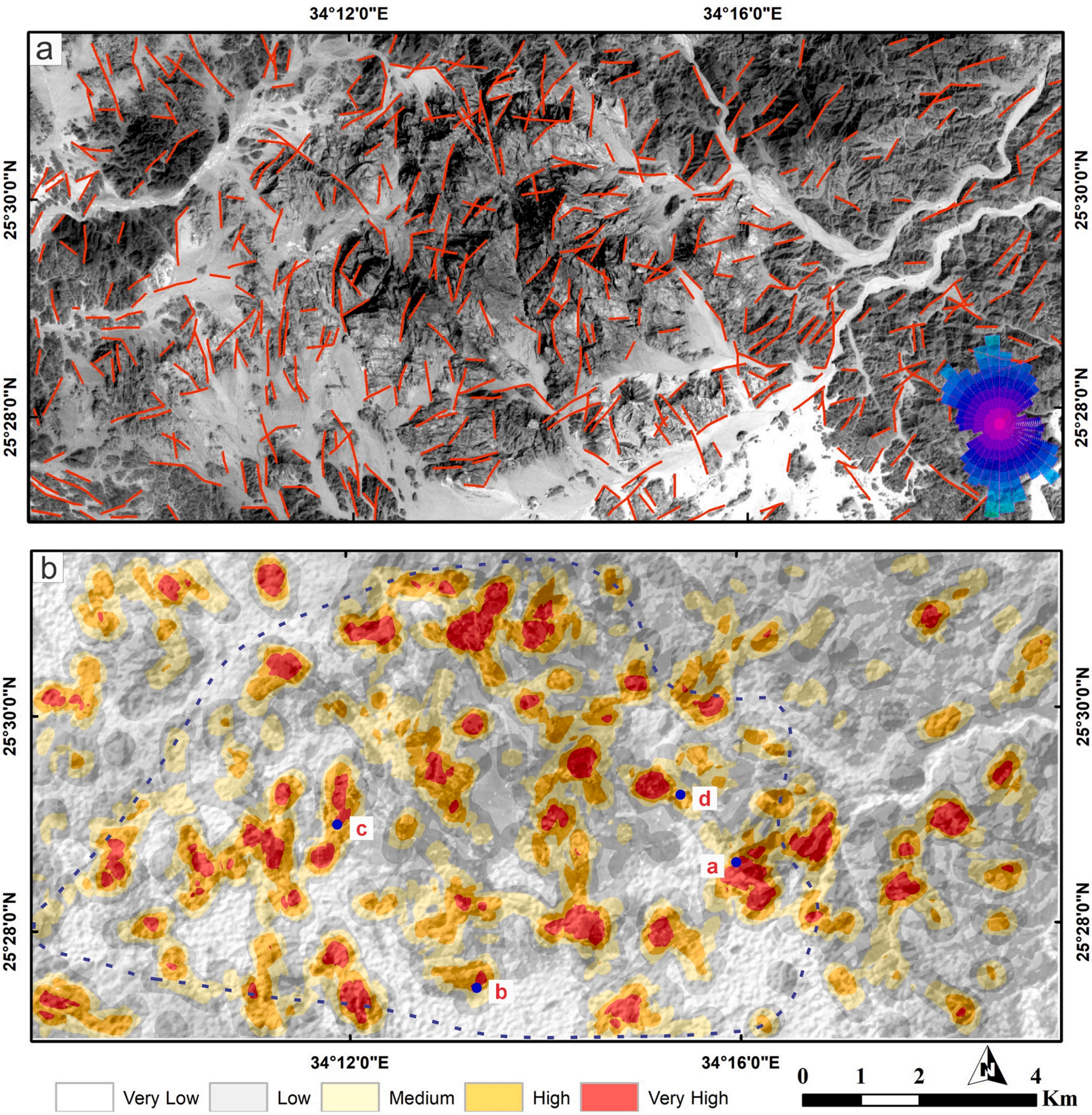

Fig. 10. (a) Automatically extracted lineaments with rose diagram in the bottom right corner, and (b) Structural lineaments density map showing the classification of the study area into low, medium, and high-structural density zones; a, b, c, and d are the locations of field photos in Fig. 15, the dashed blue line shows the boundaries of the NYG pluton. (For interpretation of the references to color in this figure legend, the reader is referred to the web version of this article.)

according to the number of lines (n) per unit area (n/km^2) (Fig. 10b). The yellow and red colors indicate the highest densities, which are hypothesized to correspond to a greater degree of fracturing, serving as a probable conduit for the transfer of fluids (Badawi et al., 2023; Gabr et al., 2022; Gupta, 2003; Ibrahim, 2013; Shebl et al., 2023a; Shebl et al., 2021). Zones characterized by a high lineament density are crucial in the concentration and localization of potential ore resources. Remarkably, the rare metal-bearing NYG pluton is an extensively structured zone predominantly characterized by medium to high structural density (Fig. 10b). The surrounding rocks are less structured than the NYG pluton, with low to medium-density zones prevailing over the high-density zones.

4.3.2. *Structural framework from aeromagnetic data*

The RTP shaded relief magnetic map exhibits both low and high magnetic signatures, respectively, in the area (Fig. 3b). The low magnetic zones are notable in the center of the area of interest with an average amplitude of 42,300 nT, related to the highly fractured rocks. The magnetic anomalies are oriented towards NNE or NNW. The surrounding rocks have high magnetic signatures and are oriented in NW and/or NE directions.

For more details about the prominent structural features (e.g., edges, faults, fractures, contacts), a tilt derivatives map and a normalized standard deviation map were generated from the RTP data (Fig. 11a, b). Examination of the two maps shows that the center of the study area (the NYG) is dominated by NNE and NNW trends that are mostly responsible for hydrothermal alteration. The southern part of the Umm Naggat area

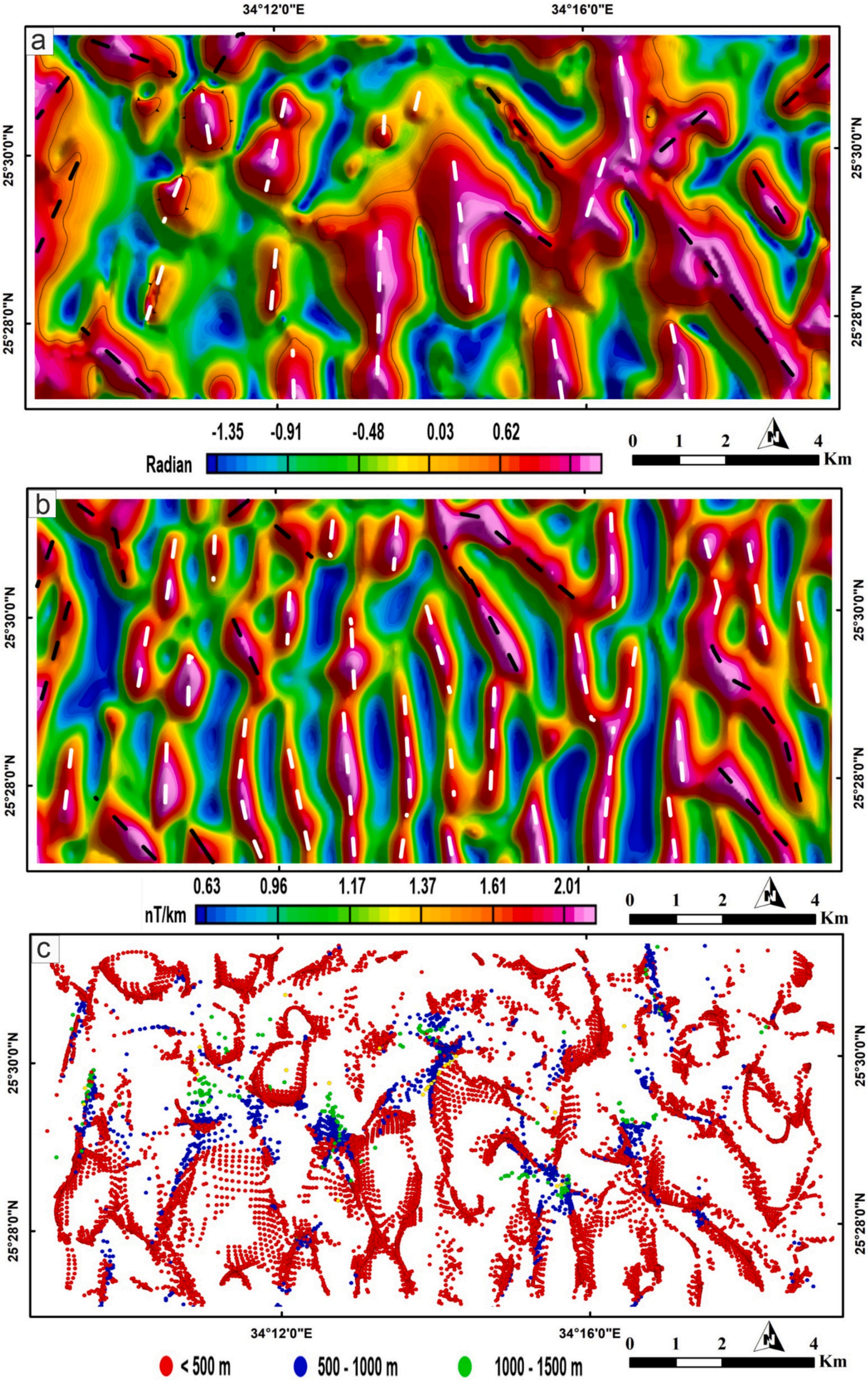

Fig. 11. Aeromagnetic results: (a) TD shaded relief map of the RTP data, (b) NSTD shaded relief map of the RTP data, and (c) Standard Euler deconvolution solutions of RTP data with SI = 0. The dashed white line shows the orientation over the area of interest, while the dashed black lines show the trends on the sides of the area.

is more fractured, which supports the higher intensities of hydrothermal alterations related to the BTG. These types of trends were depicted as white dashed lines on both maps. It is worth mentioning that more details were extracted from the NSTD map (Fig. 11b). Additionally, The NW and/or NE directions are dominant in the western and eastern parts of the area and exhibit black dashed lines (Fig. 11a, b).

In order to locate potential subsurface structures from the utilized airborne magnetic data, the standard Euler deconvolution technique has been implemented in the RTP grid map, defining a contact model (structural index $N = 0$) with a moving window of 4×4 data points. Euler solutions were acknowledged on the criterion of a relative error of 7 %. The depth ranges of the Euler solution are shown in Fig. 11c. Most of the depths range from 0 to 500 m, indicating shallow depths for the magnetic sources. In comparison, depths over 500 and up to 1500 m indicate the deepest magnetic sources. The application of this method shows a very good clustering of solutions manifesting linear segments of structural elements oriented towards the north in the study area.

5. Multiscale analysis and validation of the detected hydrothermal alterations and their associated mineralization

The presence of the remotely-sensed albitization along with ferruginated, propylitic, argillic, and phyllic alteration zones was verified through the identification of their corresponding and diagnostic mineral associations (albite, hematite, ilmenite, chlorite, epidote, calcite, biotite, kaolinite, alunite, muscovite, and illite) using the CEM technique applied to ASTER data pluton (Appendix D). Furthermore, a systematic application of conventional techniques, including fieldwork, field sampling, petrography, backscattered imaging, and SEM-EDS analysis, was employed in conjunction with CEM to validate the identified alteration zones, secondary alteration minerals, and secondary rare metal-bearing minerals associated with the mineralized NYG pluton (Appendix D).

5.1. Na-metasomatism (albitization)

Albitization is one of the most pronounced alterations in the NYG pluton. In order to validate the findings obtained by the conventional MNF methodology (Fig. 5a), the spectral fingerprints of albite were retrieved using the CEM method (Appendix E). Visual correlation between the two results demonstrates spatial coherence in allocating albitization from the MNF and albite from the CEM. During field investigations, albitization was extensive, where albitized granites are commonly observed as dome-like protrusions within the BTG (Appendix E). Additionally, swarm-like parallel thin layers of albite were observed along the outer peripheries of the AFG. These layers are closely spaced with variable thickness. Friable albitization zones up to several meters in width frequently develop grading from the biotite granite. Hence, albitization facilitated the fluid circulation of the subsequent alterations.

Additionally, NW-trending dykes of the albitized granites frequently dissect AFG and BTG. Several apophyses of albitized granites cut across the country rocks, particularly metavolcanics towards the North. The thickness of these dykes and apophyses is mostly less than 3 m. Thus, the albitization process and albite abundance are largely fracture-bound alterations developing close to the granitic pluton and its tectonic lineaments. The whitening phenomenon exhibited in feldspars or granitoid outcrops is a significant macroscopic signal of intense albitization, which has been frequently documented in numerous albitized granitoids (Azer et al., 2019; El-Dokouny et al., 2023; Kaur et al., 2012; Zoheir et al., 2020). Therefore, albitization has washed out the original pinkish-buff color of the granite and turned it white albite-dominated granite. Albitized granites exhibit a grain size varying from medium to coarse-grained and occasionally porphyritic (Appendix E). Silicification and iron oxide impregnations are developed in close spatial association with the albitization. The presence of Fe-oxide is inferred to have caused the gray coloration of the rock (Appendix E). Silicification leads to the recrystallization of quartz and the formation of large quartz crystals (Appendix E). Consequently, albitized granite develops locally into albite-quartz-rich varieties. In areas characterized by intense hydrothermal alteration, the formation of albitite may occur sporadically.

In thin sections, the albitization is marked by the precipitation of new albite crystals recorded as an intra-crystalline or inter-crystalline secondary phase. Albite crystals tend to have a smaller grain size than other mineral components. While albite increases, alkali feldspar and quartz decrease without extensive textural changes. The granitic rocks' original textures may still be preserved during albitization, even after completely altering the primary mineralogy. Intra-crystalline albite dominantly disturbs and replaces the original Na-rich phase of perthites to form the patchy perthites after string, rod, or vein perthitic textures (Appendix E). Moreover, the albite lamellae within the k-feldspar perthites are size-amplified and broadened as a record for the Na-alteration (Appendix E). Chessboard-twinned albite is one of the most prominent features of the albitized rocks, which is considered to have resulted from the intense replacement of microcline by albite. Inter-crystalline albite frequently fills the fractures between the primary minerals such as quartz and perthites. Recrystallized swapped-albite rims are common and frequently developed along the boundaries between adjacent feldspar crystals, indicating the redistribution of the albite within the surrounding perthitic feldspar (Appendix E). Quartz-rich albite veins are also recorded cutting across the major mineral constituents. These albitization-indicative textures are readily observed in the whole NYG varieties, predominantly the albitized granite samples, hence offering compelling evidence of Na-metasomatism. The former textures are further supported by SEM-EDS backscattered images where patchy perthites evolve at the expense of rod perthites and irregular invasions of newly-formed albite are infiltrated through the boundaries of perthitic k-feldspar (Appendix E).

5.2. Fe-bearing alteration (ferrugination)

Ferrugination exhibits a wide distribution within the Umm Naggat region, increasing the total concentration of iron oxides (Fe^{3+}/Fe^{2+}) that lead to the formation of hematite, ilmenite, goethite, and limonite within the invaded rocks (Robb, 2005). The CEM approach was employed to extract and map the spectral signatures of hematite and ilmenite, representing the Fe-bearing oxides. The highlighted results of the iron-bearing alteration extracted from Sentinel 2 and ASTER using band ratios (Figs. 5b, c, and 6) are comparable to those confirmed by extracted hematite and ilmenite spectral fingerprints (Fig. 12a). The field observations and sampling indicate that ferrugination is very common, and iron oxides impregnations are widely observable. Iron oxides exhibit red or black colors and could cement to form surface iron rust in oxidation zones. Shear zones and joint planes were invaded by reddish iron oxides, especially along the outer peripheries of the NYG pluton. Intense iron alteration results in completely ferruginated blocks in the southern part of the study area (Fig. 12b). The rocks collected from the NGY pluton are often highly hematitized and display a range of reddish hues, which can be attributed to the varying levels of invasion by Fe-oxides. Ilmenite exhibits submetallic luster with an iron-black color. Polished samples show partial to complete ferrugination and staining by deep reddish tints (Fig. 12c). Iron oxides occur in various forms where they fill the fractures and interspaces between mineral grains and replace the rock-forming minerals in the hand specimen. Ferrugination frequently overprints albitization and kaolinization in hand samples.

The petrographic analysis reveals a notable occurrence of iron oxides, specifically hematite and ilmenite. Most primary minerals are stained by hematite, which diminishes their optical properties. Hematite predominantly manifests as irregular aggregates, veinlets, and elongated fibrous crystals with no preferred orientation, resulting in noticeable brownish-red stains (Fig. 12d). In addition, most perthitic feldspars are turbid by reddish hematite along twinning planes. Hematite and ilmenite dominantly coexist, settled along grain margins and

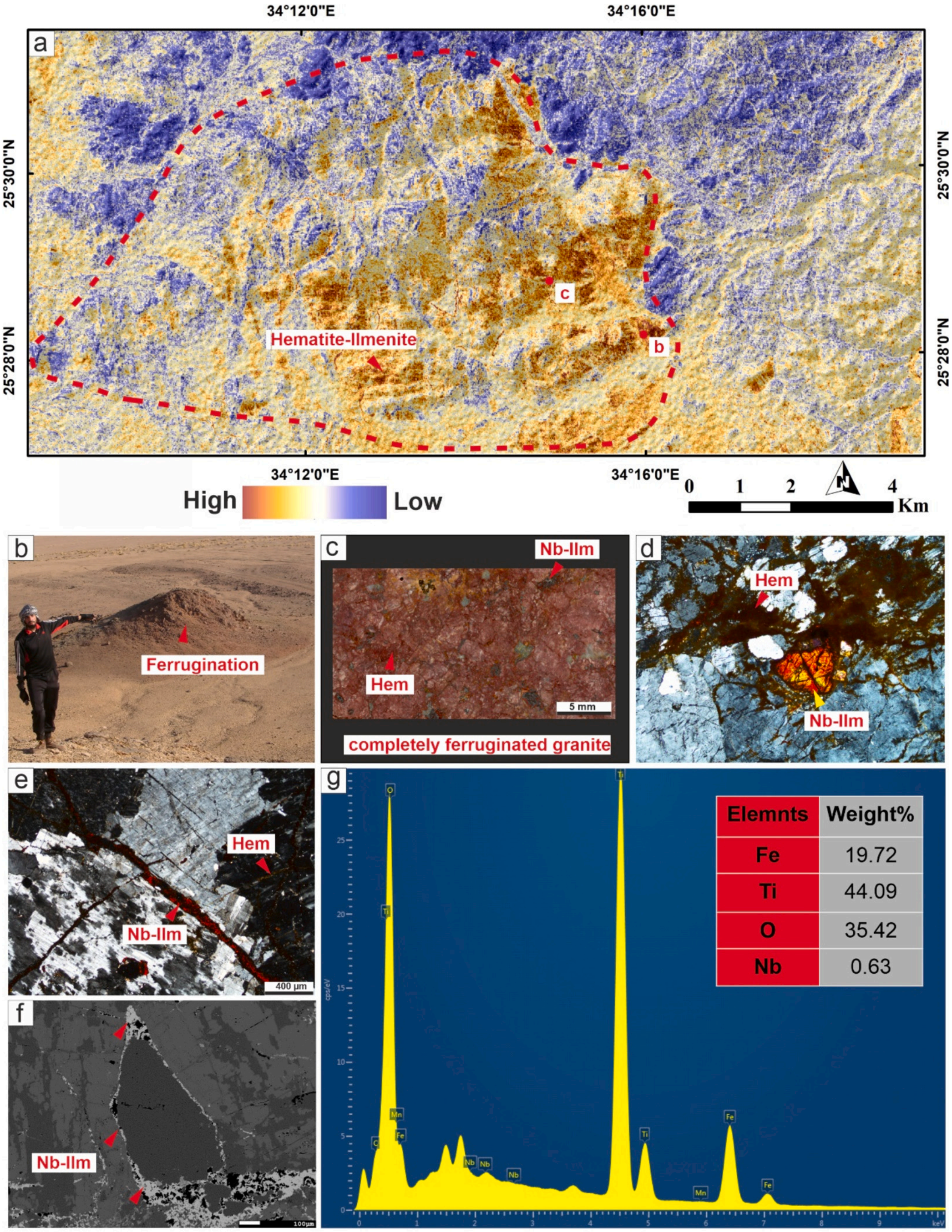

Elemnts	Weight%
Fe	19.72
Ti	44.09
O	35.42
Nb	0.63

Fig. 12. Systematic validation of iron-bearing alteration including (a) hematite and ilmenite minerals extracted by the CEM from ASTER data; b and c are the field locations of (b) and (c) images, (b) field photo show a completely ferruginated block of the NYG pluton, (c) polished hand specimen showing the extensive ferrugination of granitic sample from the NYG pluton, (d) microscopic photo (XPL) showing irregular invasions of hematite and ilmenite through the cracks and intergranular spaces, (e) microscopic photo (XPL) showing micro veins of ilmenite and hematite invading through the grain boundaries and felspar twin lamellae respectively, (f) BSE showing secondary ilmenite along the grain boundaries, and (g) SEM-EDS chart confirming the elemental composition of ilmenite as niobium (Nb)-bearing ilmenite. Nb = niobium, Hem = hematite, and Ilm = ilmenite.

cleavage planes of the biotite crystals. Veins of blackish-red iron oxides cut along and across the feldspars twinning lamellae and cleavages. The association of hematite and ilmenite in close proximity to feldspar and biotite and along their cleavages could imply a co-genetic link, probably due to the feldspar and biotite breakdown during alteration. Commonly, veins of ilmenite cut across the essential minerals or fill the fractures in between (Fig. 12e). The SEM analysis and backscattered imagery confirm the secondary origin of ilmenite, which occurs as non-uniform infiltrations through the cracks or along crystal boundaries (Fig. 12f). The elemental composition of ilmenite has been confirmed through semi-quantitative and quantitative mineral chemistry. This analysis reveals the presence of a significant quantity of Nb. Thus, ilmenite might be a possible potential source for Nb and other rare metals in the study area.

5.3. OH-bearing alterations

The study area exhibits a variety of hydroxyl-bearing alteration types, including propylitic, argillic, and phyllic alterations, commonly detected in the exposed rocks.

5.3.1. Propylitic alteration

The spectral fingerprints of chlorite and epidote were highlighted using CEM to verify the results of remote sensing image processing techniques (BR). These two minerals are most commonly associated with propylitic and ferrous silicate-rich alteration zones. The abundance of chlorite and epidote is more pronounced in the granitic rocks and metavolcanics than in other country rocks (Fig. 13a). The distribution of chlorite-epidote produced by CEM exhibits similarities to band rationing results, as depicted in Fig. 7c. Both results provide mutual support for their respective validity.

Field investigation shows a standard green color associated with propylitic and ferrous silicate alteration zones due to the formation of epidote, chlorite, and calcite (Fig. 13b). Commonly, epidote is a green-to-yellow-green mineral formed during the reaction between plagioclase feldspar and hydrothermal fluids rich in calcium and aluminum. Chlorite is a greenish mineral formed during the alteration of ferromagnesian minerals, such as biotites and amphiboles, due to the invasions of hydrothermal fluids (Fig. 13c). White calcite veins or veinlets may form due to the circulation of calcium-rich fluids. The alteration process often produces a less hard rock with a finer-grained texture, and the original rock-forming minerals may become less distinguishable (Fig. 13c). The colors of the altered minerals can vary depending on the abundance of secondary alteration minerals like epidote and chlorite (Fig. 13b, c). The alteration process can create microfractures, miarolitic cavities, and micro veins due to the chemical redistribution of minerals during hydration and alteration. Epidote, chlorite, and calcite frequently precipitate within these fractures and voids. Transitional zones are frequently observed within the BTG when the original rock undergoes partial alteration, resulting in the formation of altered rock enriched with secondary propylitic minerals. The propylitized rocks are occasionally spotted close to the albitization phases. Disseminated opaques, mainly hematite, ilmenite, and rarely magnetite, are observed in hand specimens (Fig. 13c).

Plagioclase feldspar, ferromagnesian biotites, and amphiboles are the primary minerals undergoing propylitic alteration in thin sections. This type of alteration is often associated with chloritization. The original equigranular texture changes locally to a finer-grained altered texture. Aggregates of secondary minerals such as chlorite, epidotes, and carbonates partially to completely replace the primary minerals during the alteration process (Fig. 13d). Chlorite and epidote are preferentially associated with opaque minerals. Additionally, the boundaries between alteration minerals (chlorite-epidote-carbonates) and non-altered minerals (plagioclase-biotite-amphibole) turn into gradational and are not easily distinguished. A common feature of propylitic alteration is the alteration of ferrous silicates, such as biotites, into chlorite. Most biotites in the NYG are extensively altered and exhibit partial or complete chloritization. Chlorite pseudomorphs after biotite are common (Fig. 13e). Chlorite ranges from colorless to light green to brown, exhibiting a fan-shaped to fibrous morphology. Chlorite partially replaces biotites along the grain boundaries or the cleavage planes. The alteration commonly proceeds from the crystal peripheries and extends towards the cores. The propylitic alteration and chloritization are further surveyed using mineral chemistry and backscattered imagery.

Interestingly, rare metal-bearing minerals such as ferrocolumbite ($Fe^{+2}Nb_2O_6$) are recorded within chlorite. Columbite is one of the most crucial minerals as a source of Nb. Marginal fine grains of columbite within chlorite are aligned parallel to the biotite boundaries (Fig. 13f). Occasionally, columbite is found disseminated within chlorite lamellae along biotite cleavage planes (Fig. 13f). Semi-quantitative elemental analysis using EDS confirms the higher iron content in columbite rather than manganese, and the Nb reaches up to 53 % of the composition (Fig. 13g).

5.3.2. Argillic alteration

The CEM technique was executed using kaolinite and alunite spectral signatures to define the highest pixel value for the two minerals. The visually observable correlation suggests a reasonable agreement between band ratio-mineral indices and CEM results (Fig. 8 and Appendix F). The field outcrops exhibit remarkable evidence of argillic alteration, characterized by various zones of friable kaolinitic alteration showing extensive textural and mineralogical changes. The kaolinized rocks often show a characteristic pale yellowish-brown color due to the presence of clay minerals (Appendix F). Kaolinitic alteration is best evidenced in the granitic rocks characterized by high fracturing and jointing, facilitating fluid transport (Appendix F).

Kaolinitic alteration sometimes grades into or merges with propylitized rocks, especially within biotite granite in the South. Thrust faults are commonly enclosed in argillic alteration zones, such as those along the contact between the BTG and metagabbro-diorites. The alteration zones associated with kaolinization are marked by the existence of fine-grained clay minerals and a high degree of silica enrichment due to the aluminosilicates base-leaching in the surrounding rock. Rocks underwent bleaching, resulting in various colorations such as pale yellow, white, and light gray (Appendix F). These rocks exhibit a distinctive porous texture; vugs are abundant. Locally, impregnations of manganese-iron oxides are precipitated within the zones of kaolinitic alteration. Clay minerals have a lower refractive index than most primary minerals, resulting in light scattering and giving the polished samples a distinctive dull appearance (Appendix F).

Feldspar crystals are hydrolyzed and altered into clay minerals in kaolinization. In thin sections, feldspar minerals, particularly the K-rich phases (orthoclase and microcline), show a cloudy appearance. Clay minerals are inter-dispersed throughout the rock, filling inter-crystalline spaces. Polymineralic (clay and quartz) veins are common. Moreover, Kaolinite prominently forms irregular patches disturbing orthoclase and microcline (Appendix F). Perthites, in particular, are extensively kaolinized; however, the alteration is confined to the k-rich phase. In perthites, kaolinitic alteration exhibits the same shape as the k-feldspar: lamellar, rod, patches, or flames (Appendix F). Kaolinite pseudomorphs after K-feldspar argillization are also recorded. Sometimes, the clay minerals are interlocking with granular, fine quartz, and minor hematitic dust.

5.3.3. Phyllic alteration

Phyllic hydrothermal alteration is widespread in a variety of exposed rocks in the Umm Naggat area. The spectral signatures of the muscovite and illite were used in the CEM technique to highlight their abundance within the study area and to confirm the mapping outcomes of phyllic-altered zones by BR and RBD. Notably, the obtained muscovite-illite distribution within the NYG pluton is moderately similar to the BR and RBD techniques that highlighted phyllic alteration (Figs. 14a and 9).

During phyllic alteration, most rock-forming minerals were replaced, and the primary textures were destroyed (Fig. 14b). Severely affected phyllic alteration zones in the field are characterized by intensive muscovitization and subsequent silicification rather than illitization. The phyllic zones cover broad areas mainly within the BTG in the western and southern parts of the NYG pluton. In outcrop, zones exhibiting phyllic alteration are readily observable due to their dull brownish-white coloration and abundance of rust stainings. Silicification usually concludes phyllic alteration, where swarm-like quartz veins are common.

The collected samples are characterized by a brittle sticky surface and an assemblage of mm-wide sericite-muscovite-recrystallized silica (Fig. 14c). Pure sericite occurrences are also noted in the extensively altered samples. Moreover, sericitization and muscovitization can be pervasive, selectively-pervasive (certain minerals are replaced), or non-pervasive (cavity-controlled or bordering on fractures). The hand specimens exhibiting phyllic alteration display a bleached coloration and nearly textureless surface. Pervasively altered samples are commonly white to gray, and primary textures are often obliterated. Sericite is exceedingly fine-grained and may exhibit white or pale-yellowish-brown coloration or pale pinkish flakes (Fig. 14c). Since quartz is

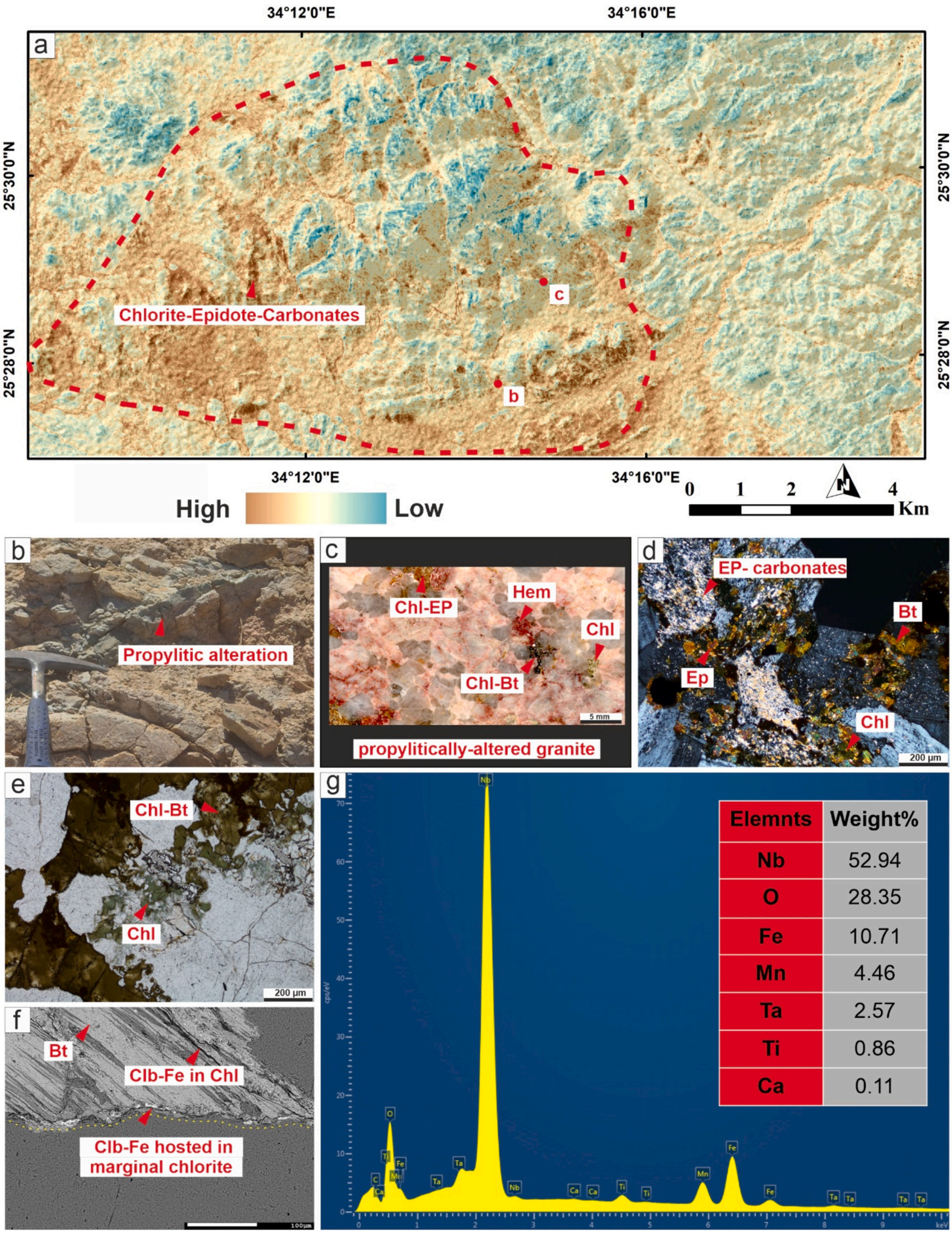

Elemnts	Weight%
Nb	52.94
O	28.35
Fe	10.71
Mn	4.46
Ta	2.57
Ti	0.86
Ca	0.11

Fig. 13. Systematic validation of propylitic alteration including (a) chlorite, epidote, and calcite minerals extracted by the CEM from ASTER data; b and c are the field locations of (b) and (c) images, (b) field photo showing propylitic alteration occurring in green, (c) polished hand specimen showing the extensive propylitic alteration (d) microscopic photo (XPL) showing irregular fine aggregates of chlorite, epidote, and carbonates filling the intergranular spaces, (e) microscopic photo (PPL) showing fine aggregates of chlorite in green and chlorite pseudomorph, (f) BSE showing secondary columbite-Fe as a marginal phase due to alteration of biotite, and (g) SEM-EDS chart confirming the elemental composition of columbite. Nb = niobium, Hem = hematite, Chl = chlorite, Bt = biotite, Clb-Fe = columbite-Fe, and Ep = epidote. (For interpretation of the references to color in this figure legend, the reader is referred to the web version of this article.)

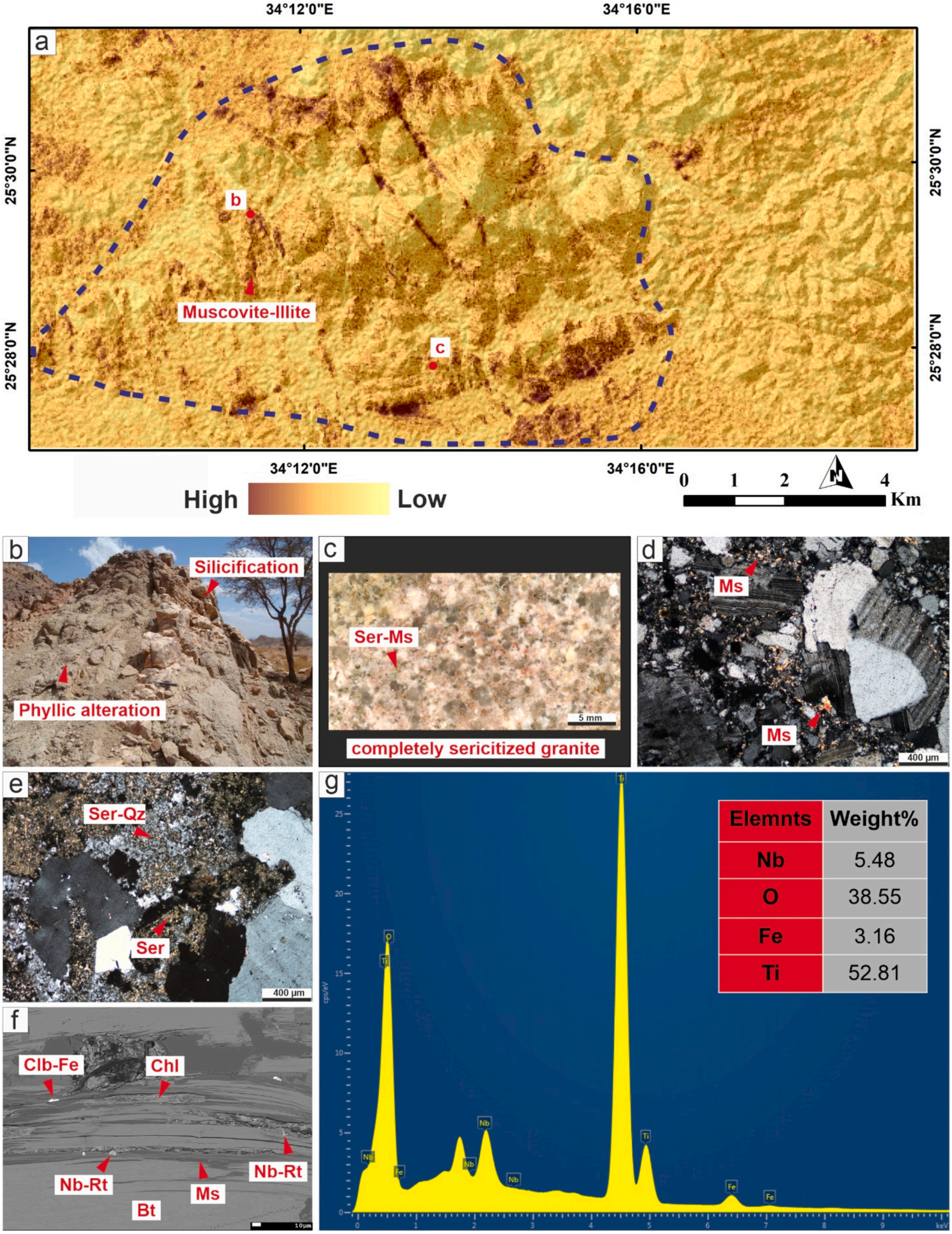

Elemnts	Weight%
Nb	5.48
O	38.55
Fe	3.16
Ti	52.81

Fig. 14. Systematic validation of phyllic alteration including (a) sericite (muscovite-illite) minerals extracted by the CEM; b and c are the field locations of (b) and (c) images, (b) field photo showing phyllic alteration (muscovitization) occurring with quartz veins cutting through the phyllic alteration zone, (c) polished hand specimen showing the complete sericitization of granite sample, (d) microscopic photo (XPL) showing irregular fine aggregates of muscovite filling the intergranular spaces, (e) microscopic photo (XPL) showing fine aggregates of sericite replacing quartz and feldspars, (f) BSE image showing the secondary columbite-Fe and Nb-rutile as an alteration phase after biotie muscovitization, and (g) SEM-EDS chart confirming the elemental composition of rutile as Nb-rich rutile. Nb = niobium, Ser = sericite, Ms. = muscovite, Qz = quartz, Rt = rutile, and Clb-Fe = columbite-Fe.

typically associated with phyllic alteration, the altered rocks range in hardness from soft (predominantly sericitized) to hard (sericite-quartz dominant).

In thin sections, phyllic alteration dominantly includes the formation of very fine sericite-muscovite after partial or complete replacement of feldspars and biotite. Muscovite is widely disseminated as an interstitial phase between primary feldspars (Fig. 14d). In extensive phyllic alteration zones, the granitic rocks are entirely altered to sericite-quartz-dominated rock (Fig. 14c, e). Sericite occurs as fine anhedral aggregates and is typically colorless or pale yellow under the microscope, but pale green varieties are rarely recorded. Sericite commonly fills cavities and fractures. Biotite is frequently altered to muscovite and quartz. Muscovite pervasively replaces biotite and the replacement proceeds from crystal boundaries towards the core. Flakes of muscovite occur along cleavage planes of biotite (Fig. 14f). Tiny anhedral crystals of columbite-(Fe) and rutile are observed within secondary muscovite using the mineral chemistry analysis. Columbite and rutile crystals are frequent byproducts of biotite alteration (muscovitization). Remarkably, the elemental analysis of rutile reveals the Nb enrichment (Fig. 14g). The observed spatial correlation between columbite and rutile with inter-embayed muscovite suggests a cogenetic relationship.

5.4. EPMA analysis of gangue and secondary rare metal minerals

Alteration-formed rare metal-rich minerals are reasonably common in the studied granites and are mostly associated with biotite, muscovite, chlorite, albite, and hematite (Figs. 12, 13, and 14), indicating a genetic relationship. Therefore, the precise chemical composition of some host and ore minerals was analyzed by EPMA for quantitative investigation (Tables 1 and 2). Quantitative EPMA analysis of biotite (Table 1) implies the iron enrichment of the studied biotites with FeO contents ranging between 27.99 and 31.92 wt%. According to compositional classification of Foster (1960), this biotite exhibits a siderophyllite composition (Fig. 15a). The average contents of SiO_2, K_2O, and Al_2O_3 are 33.88, 8.90, and 16.76 wt%, respectively. The volatile content (H_2O and F) reaches up to 3.55 wt%. Remarkably, the Ti and Nb contents are enriched in the studied biotite and consequently can be categorized as Nb-rich biotites. The TiO_2 contents vary from 1.05 to 1.90 wt% (average = 1.44 wt%), while the Nb_2O_5 contents range between 0.17 and 0.20 wt% (average = 0.18 wt%). Based on the ternary $10TiO_2$–(FeO + MnO)–MgO discrimination diagram, the biotite plots within the hydrothermally-altered biotite field due to its relatively low Ti contents as an indication for alteration (Nachit, 1985) (Fig. 15b).

The EPMA analysis (Table 1) included the examination of secondary muscovite and chlorite, which were formed as a result of biotite alteration. Muscovite contains higher Si and Al than biotite, with SiO_2 and Al_2O_3 contents peaking at 53.23 and 29.83 wt%, respectively. The K_2O contents of muscovite are widely variable, ranging between 2.57 and 9.80 wt% (average = 4.60 wt%). Considerable amounts of Fe, Ti, and Nb are still preserved (after biotite) within the crystal structure of muscovite. According to the chemical classification diagram after Foster (1960), the studied muscovites are classified as Fe-rich, containing up to 14.19 wt% of FeO (Fig. 15a). The TiO_2 and Nb_2O_5 contents are lower than biotite, averaging at 0.76 and 0.11 wt%, respectively. The alteration processes enriched the secondary muscovite with Li_2O compared to biotite (average = 1.01 wt%). On the other hand, chlorite contains the

Table 1

EPMA analyses (wt%) of the primary biotite, secondary muscovite, and secondary chlorite from the studied granites in the Umm Naggat area.

Mineral	Primary biotite (n = 12)			Secondary muscovite (n = 7)			Secondary chlorite (n = 8)		
Oxides	Min	Max	Avg	Min	Max	Avg	Min	Max	Avg
SiO_2	31.66	35.02	33.88	48.02	53.23	49.71	19.55	28.19	25.22
TiO_2	1.05	1.90	1.44	0.30	1.25	0.76	0.16	0.49	0.25
Al_2O_3	15.76	17.74	16.76	22.08	29.83	24.13	8.70	14.50	12.00
FeO	27.99	31.92	29.33	6.05	14.19	10.22	42.26	53.33	47.19
MnO	0.81	1.34	1.09	0.03	0.75	0.47	0.01	0.05	0.04
MgO	0.00	0.30	0.03	0.00	1.61	0.23	0.45	0.76	0.60
Nb_2O_5	0.17	0.20	0.18	0.02	0.23	0.11	0.01	0.14	0.05
Ta_2O_5	nd	nd	nd	nd	nd	nd	nd	nd	nd
CaO	0.00	0.17	0.09	0.01	0.09	0.03	0.65	0.82	0.71
Na_2O	0.09	0.14	0.12	0.06	0.12	0.09	0.01	0.05	0.03
K_2O	8.29	9.34	8.90	2.57	9.80	4.60	0.14	1.07	0.54
BaO	0.01	0.09	0.05	0.00	0.06	0.02	0.04	0.17	0.10
F	0.12	0.77	0.48	1.04	3.49	2.16	0.00	0.00	0.00
Cl	0.06	0.08	0.07	0.00	0.01	0.00	0.00	0.01	0.01
Li_2O*	0.00	0.50	0.21	0.25	1.01	0.60	nd	nd	nd
H_2O*	3.17	3.50	3.34	2.54	4.12	3.25	9.02	10.33	9.80
O=F,Cl	0.07	0.34	0.21	0.44	1.47	0.91	0.00	0.00	0.00
Total	93.75	97.97	95.74	94.08	98.87	95.48	92.26	99.81	96.54
Structural formula calculated based on 22 O (biotite and muscovite) and 14 O (chlorite)									
Si	5.46	5.76	5.66	6.76	6.98	6.88	2.60	3.27	3.08
Al^{IV}	2.24	2.54	2.34	1.02	1.24	1.12	0.73	1.36	0.92
AI^{VI}	0.80	1.11	0.95	2.47	3.39	2.81	0.00	1.23	0.81
Ti	0.13	0.24	0.18	0.03	0.13	0.08	0.01	0.04	0.02
Fe^{2+}	3.94	4.60	4.10	0.65	1.66	1.19	4.27	5.93	4.85
Mn	0.12	0.19	0.15	0.00	0.09	0.06	0.00	0.01	0.00
Mg	0.00	0.07	0.01	0.00	0.31	0.05	0.09	0.13	0.11
Nb	0.01	0.01	0.01	0.00	0.02	0.01	0.00	0.00	0.00
Li*	0.00	0.00	0.00	0.00	0.00	0.00	0.00	0.00	0.00
Ca	0.00	0.03	0.02	0.00	0.01	0.00	0.08	0.10	0.09
Na	0.03	0.04	0.04	0.02	0.03	0.02	0.00	0.01	0.01
K	1.79	2.02	1.90	0.42	1.76	0.82	0.02	0.17	0.09
Ba	0.00	0.01	0.00	0.00	0.00	0.00	0.00	0.01	0.00
F	0.06	0.40	0.25	0.43	1.54	0.95	0.00	0.00	0.00
Cl	0.00	0.02	0.02	0.00	0.00	0.00	0.00	0.00	0.00
OH*	3.58	3.92	3.73	2.46	3.57	3.05	8.00	8.00	8.00

LiO_2* calc. from Monier and Robert (1986).

H_2O* calculation after Tindle and Webb (1990).

nd = not detected.

Table 2
EPMA analyses (wt%) of alteration-formed columbite, rutile, and ilmenite from the studied granites in the Umm Naggat area.

Mineral	Secondary columbite (n = 5)			Secondary rutile (n = 5)			Secondary ilmenite (n = 5)		
Oxides	Min	Max	Avg	Min	Max	Avg	Min	Max	Avg
CaO	0.00	0.63	0.22	0.00	0.07	0.01	0.91	1.18	1.00
Al_2O_3	0.00	0.99	0.29	0.00	0.00	0.00	1.73	1.95	1.84
FeO	14.65	16.20	15.55	7.05	8.49	7.94	20.56	23.38	21.90
MnO	4.10	5.35	4.66	0.00	0.03	0.02	0.08	0.10	0.08
SiO_2	0.00	0.36	0.15	0.00	0.08	0.02	1.57	1.83	1.73
TiO_2	1.77	3.05	2.39	62.79	70.49	66.67	62.68	65.77	64.27
Nb_2O_5	62.29	69.08	66.96	18.12	21.45	19.97	3.66	4.01	3.81
Ta_2O_5	4.12	10.85	6.52	1.36	5.13	3.74	nd	nd	nd
SnO_2	nd	0.33	0.13	0.66	1.61	1.23	nd	0.17	0.09
WO_3	2.09	4.12	2.78	0.44	0.73	0.56	nd	nd	nd
Total	98.72	100.56	99.94	99.25	101.50	100.17	94.01	95.64	94.73
Structural formula calculated based on 6 O (columbite and ilmenite) and 2 O (rutile)									
Ca	0.00	0.04	0.01	0.00	0.00	0.00	0.05	0.06	0.05
Al	0.00	0.07	0.02	0.00	0.00	0.00	0.10	0.11	0.10
Fe	0.70	0.80	0.76	0.09	0.11	0.10	0.80	0.93	0.86
Mn	0.20	0.26	0.22	0.00	0.00	0.00	0.00	0.00	0.00
Si	0.00	0.02	0.01	0.00	0.00	0.00	0.07	0.09	0.08
Ti	0.08	0.13	0.11	0.73	0.78	0.75	2.24	2.31	2.28
Nb	1.72	1.80	1.76	0.12	0.15	0.14	0.08	0.08	0.08
Ta	0.06	0.13	0.09	0.01	0.02	0.02	0.00	0.00	0.00
Sn	0.00	0.01	0.00	0.00	0.01	0.01	0.00	0.00	0.00
W	0.03	0.05	0.04	0.00	0.00	0.00	0.00	0.00	0.00

nd = not detected.

highest iron content relative to biotite and muscovite, with FeO contents reaching 53.33 wt%. Therefore, in the classification diagram of Ruiz Cruz and Nieto (2006), chlorite plots within the Fe-chlorite member (chamosite) (Fig. 15c). The SiO_2 and Al_2O_3 are depleted in chlorite with average contents of 25.22 and 12.00 wt%, respectively. Low but significant amounts of TiO_2 and Nb_2O_5 (averages = 0.25 and 0.05 wt%, respectively) are detected within chlorite. It is worth mentioning that the concentration of Ta in biotite, muscovite, and chlorite is consistently below the detection limit.

Secondary rare metal-bearing minerals such as columbite, rutile, and ilmenite were also analyzed using EPMA, as shown in Table 2. Secondary columbite is richer in Fe than Mn containing up to 16.20 and 5.35 wt%, respectively. Accordingly, it is classified as Ferro-columbite regarding the quadrilateral diagram for classifying Columbite-tantalite group minerals after Černý (1989) (Fig. 15d). Columbite is the major host for Nb and Ta compared to rutile and ilmenite. It contains high amounts of Nb and Ta, summing up to 73.84 wt% on average. The high contents of Ti (up to 3.05 wt% of TiO_2) within columbite are significat in indicating its secondary origin.

Furthermore, the analysis results of secondary rutile show extreme enrichment of rare metals (Table 2). While rutile contains high amounts of TiO_2 (up to 70.49 wt%), elevated amounts of Nb, Ta, Sn, and W are substantially incorporated at the expense of Ti in the crystal structure. The highest substitution is exhibited by Nb, reaching up to 21.45 wt%, followed by Ta (up to 5.13 wt%). The contents of Sn are higher than W, averaging 1.23 and 0.56 wt%, respectively. Ilmenite has lesser amounts of rare metals compared to rutile, mostly because it has lower titanium content (Table 2). However, the titanium concentrations in ilmenite are considerably higher than iron, suggesting that it has a secondary origin. Ilmenite can have a maximum of 4.18 wt% combined amounts of Nb, Ta, Sn, and W. The TiO_2 and FeO amounts range from 62.68 to 65.77 wt% and from 20.56 to 23.38 wt%, respectively. Ilmenite is present either as a result of the alteration of biotite within muscovite or chlorite, or it is formed directly from hydrothermal fluids associated with hematite or filling the spaces between essential minerals like quartz and feldspars.

5.5. *Field observations of linear structures and their related alterations*

The exposed rock units, specifically the NYG pluton, exhibit significant fracturing and structural deformation. Dykes, veins, fractures, joints, and shear zones are common (Fig. 16a). These linear structures exhibit a proximal spatial relationship with diverse alteration types. Albitization is frequently observed in diverse forms, such as albite dykes that traverse the granitic rocks in the study area (Fig. 16b). These dykes extend into adjacent rocks, such as metavolcanics in the northern portion. Additionally, quartz veins are prevalent structural attributes frequently occurring as parallel swarm-like patterns. Quartz veins, indicative of silicification, are often found in conjunction with phyllic alteration (Fig. 16c). Shear zones exhibit a large distribution in association with granitic rock, precisely along the boundaries of the NYG pluton. Iron-bearing alteration frequently invades these zones, resulting in a distinctive reddish tint distinguishing them from the surrounding host rocks (Fig. 16d). It is essential to highlight that the field measurements of dykes, veins, and shear zones confirm the consistency in trends found in these lineaments (such as N40E-N50W-N35W-N30W) as identified by remote sensing, airborne magnetic data, and rose diagrams (Figs. 16, 10, and 11). Moreover, most structural features observed during the field survey (dykes, veins, and shear zones) plot within the medium to high structural density zones highlighted by the automatic lineaments extraction results (Figs. 16 and 10b).

6. Discussion

6.1. *Structurally-controlled hydrothermal alterations and secondary rare metal mineralization*

The evolutionary history of the ANS is characterized by a prolonged period of magmatic activity spanning from 800 to 540 Ma (Stern, 1994; Johnson et al., 2011). The culmination of this activity was evidenced with highly fractionated A-type granite with mafic to felsic dikes. Liegeois et al. (1998) stated that this event marked a transition towards intra-plate, alkaline magmatism. After a collision, rifts, transtensional domains, and large-scale horizontal shear zones are common and would result in high-K calc-alkaline and alkaline-peralkaline magmas (Liegeois et al., 1998; Fowler, 2001; Bonin, 2004). According to several authors (e.g., Abdel-Rahman and Martin (1990), Beyth et al. (1994), and others), the main magmatism in this area is thought to be caused by (1) low-angle normal faults and extensional tectonics; (2) deformation after collisions; and/or (3) relatively shallow-level epizonal plutons along active continental margins. The granitoids were subdivided into

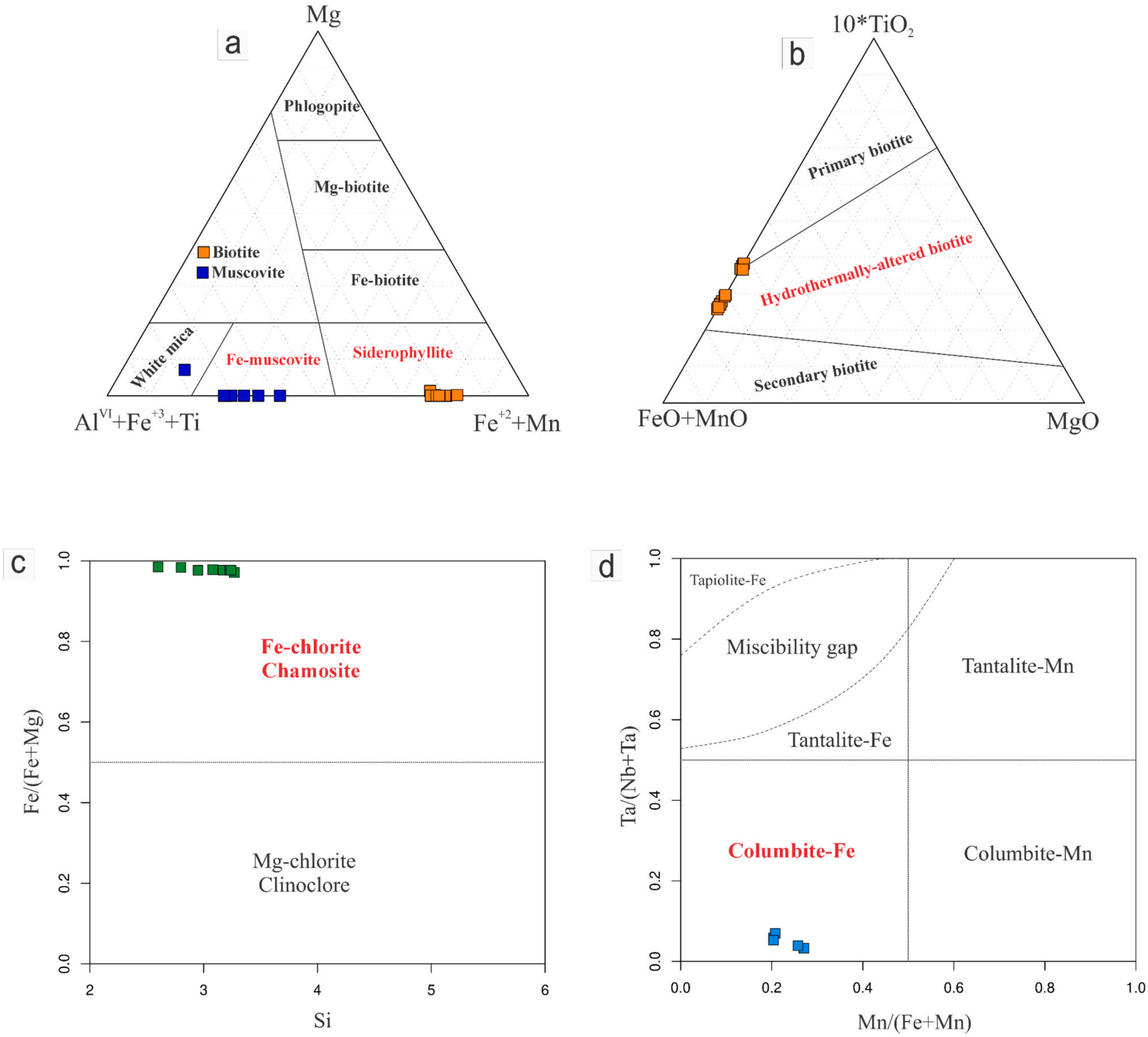

Fig. 15. (a) chemical classification diagram of primary biotite and secondary muscovite after Foster (1960), (b) the ternary $10TiO_2$–(FeO + MnO)–MgO discrimination diagram of primary, hydrothermally-altered and secondary biotite after (Nachit, 1985), (c) compositional classification diagram of secondary chlorite after (Ruiz Cruz and Nieto, 2006), and (d) Columbite-tantalite quadrilateral diagram for the classification of secondary columbite after Černý (1989).

foliated, mafic, gray (Older Granites), syn-to-late-orogenic of diorite to granodiorite composition (ca. 800–610 Ma: Bentor, 1985; Hassan and Hashad, 1990; Lundmark et al., 2012), and nonfoliated, felsic, pinkish-red (Younger Granites), post-orogenic granites of alkali granite, syenogranite and monzogranite composition (ca. 600 and 530 Ma: Lundmark et al., 2012; Hassan and Hashad, 1990; Stern and Gottfried, 1986; Beyth et al., 1994).

Utilizing our applicable methodology, particularly remote sensing, demonstrates an enhanced ability to differentiate the younger granite of Umm Naggat. This differentiation is achieved by considering the multiphase magmatism, as evidenced by the presence of mafic-rich biotite granite (specifically, granite rich in magnesium hydroxide), mafic-poor alkali feldspar granite, and albitized granite (see Figs. 5–9). The variation in the composition of mafic and felsic rock-forming minerals significantly affects the resulting byproducts and subsequent hydrothermal alterations. Upon conducting a comprehensive analysis of the observed alterations within the Umm Naggat pluton, it becomes evident that the alterations characterized by magnesium-iron enrichment (specifically, propylitization, ferrugination, and ferrous-silicate alterations) are more likely associated with the southern region of the pluton. Conversely, the alterations marked by magnesium-iron depletion (namely, argillization, phyllitization, and albitization) are found along the western and northern flanks and are linked to the corresponding fault sets. The former can document that these granites have evidenced prolonged crustal fractionation, indicating emplacement of the pluton from south to north contemporaneous with the development of mature continental crust.

Regarding mineralization, the NYG is characterized by high concentrations of rare metals (particularly niobium and tantalum). The NYG is widely accepted as one of the demonstrative models for magmatic-hydrothermal rare metal deposits, which is characterized by a systematic hydrothermal alteration and potential mineralization zones (Abd El Nabi, 2012; Abdelkader et al., 2022; Al-Arifi et al., 2021; Gaafar et al., 2022; Gamal-Adeen et al., 2023; Khedr et al., 2023). However, the nature of rare metal mineralization and petrogenesis (relative role of magmatic versus hydrothermal processes) is still debated to the degree that the majority of prior studies limit the occurrence of rare metals to the albitized granite in the northern part of the NYG pluton (Abd El Nabi,

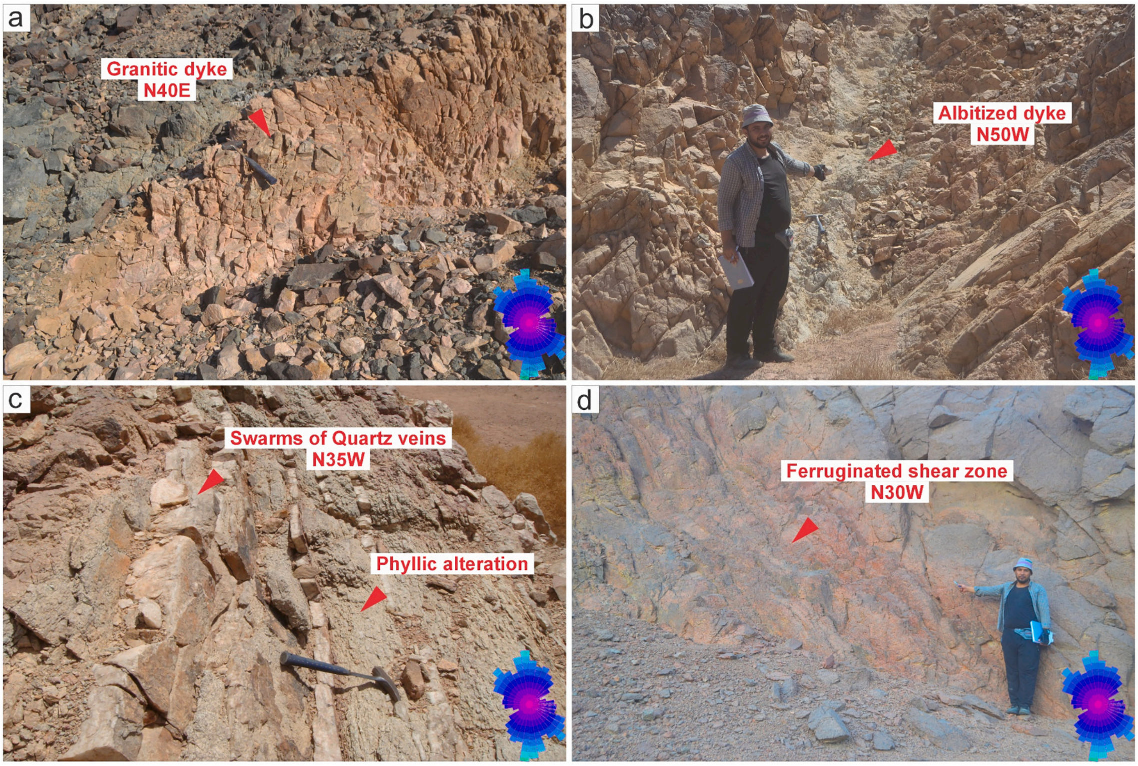

Fig. 16. Field validation of the extracted lineaments, their trends, and alterations where (a) granitic dyke cutting through metagabbro-diorites, trending in N40E direction, (b) albitization occurring as albite dyke trending in N50W direction and cutting through the biotite granite, (c) parallel swarms of quartz veins trending in N35W directions and cutting through phyllic alteration zone, and (d) shear zone within the biotite granite trending in N30W direction and invaded by iron-bearing hydrothermal fluids. Note that all the trends measured during field reconnaissance concord with those from the rose diagram analysis. (For interpretation of the references to color in this figure legend, the reader is referred to the web version of this article.)

2012; Abdelkader et al., 2022; Al-Arifi et al., 2021; Gaafar et al., 2022; Gamal-Adeen et al., 2023; Khedr et al., 2023). This limitation is not conformable with the granitic pluton's widely and extensively altered character, where it exhibits several types of alterations as depicted in the current research. Mineral assemblages in hydrothermally altered rocks are influenced by various factors, including pressure, temperature, fluid composition (for instance, elements concentrations Cl-, H+, CO2, Na+, K+, F, B, H2S), original host-rock composition, and the fluid-rock ratio (El-Desoky et al., 2022b). Magmatic-hydrothermal processes are a critical contributor to rare metal mineralization (Abd El Monsef et al., 2023; Abuamarah et al., 2022; Harlaux et al., 2017; Michaud and Pichavant, 2020; Sami et al., 2022; Su et al., 2021; Yang et al., 2020a). However, there has been a scarcity of scholarly investigations focusing on the occurrence of rare metal mineralization originating solely from secondary processes, specifically hydrothermal alteration (Yang et al., 2023; Yang et al., 2020b; Zhu et al., 2019; Zhu et al., 2018). The former issue was a strong motive in the current study to investigate more deeply into the fluid circulation system (detailed analysis of hydrothermal zones), structural framework (remote sensing and geophysical data), and their spatial correlation (overlay analysis).

The study area is overprinted by several types of hydrothermal alterations like albitization, ferrugination, argillic, propylitic, and phyllic alteration, as depicted by remote sensing results (Fig. 17a). Aeromagnetic data and automatic lineaments directional analysis indicate the occurrence of major faulting and fracturing in NW-NNW-NNE-NE directions, with WNW, ENE, and N-S as minor trends. Structures are key elements for hydrothermal alteration mapping since they serve as pathways for the movement of hydrothermal fluids. Therefore, an integrated overlay analysis was conducted by superimposing the extracted hydrothermal alterations onto the lineaments density map of the Umm Naggat area to enable their spatial correlation (Fig. 17b). As a result, it is possible to discern the most promising regions for mineralization by considering the convergence of areas with a high density of lineaments and significant degrees of alteration (Fig. 17b).

Strikingly, the spatial overlay analysis of hydrothermal alteration zones and structural density highlights the following: (1) Most high structural density zones are confined within and around the Umm Naggat rare metal-bearing granite, (2) the intensity of hydrothermal alteration in the study area is primarily more pronounced in the NYG pluton compared to the surrounding rocks, (3) the notable spatial correlation between the hydrothermal alteration and the high structural density zones, where the intense hydrothermal alteration is frequently found overprinting or close to a high structural density zone, particularly in the NYG, (4) the consistency between linear hydrothermal alteration trends and the directional analysis results from remote sensing and aeromagnetic data, several types of hydrothermal alterations exhibit an NNW and NNE linear trends.

Field reconnaissance and sampling accurately delineated and validated the ground distribution of the various alteration types in the study area and the spatial association between structural elements and alteration zones. Moreover, the mineral assemblages, indicative of distinct alteration types, were verified through petrographic investigations. Remarkably, secondary rare metal-bearing phases resulting from hydrothermal alteration within the NYG were confirmed using backscattered imaging and mineral chemistry analysis. Secondary Ilmenite, rutile, and columbite-(Fe) were recorded as fine flakes and dispersed grains associated with secondary muscovite and chlorite or veins cutting across and filling the spaces between the primary minerals. The utilization of mineral chemistry analysis confirmed the elemental composition and facilitated the identification of the alteration minerals. Secondary ilmenite, rutile, and columbite have a notable enrichment in niobium (Nb) and hence present a potential reservoir of hydrothermal

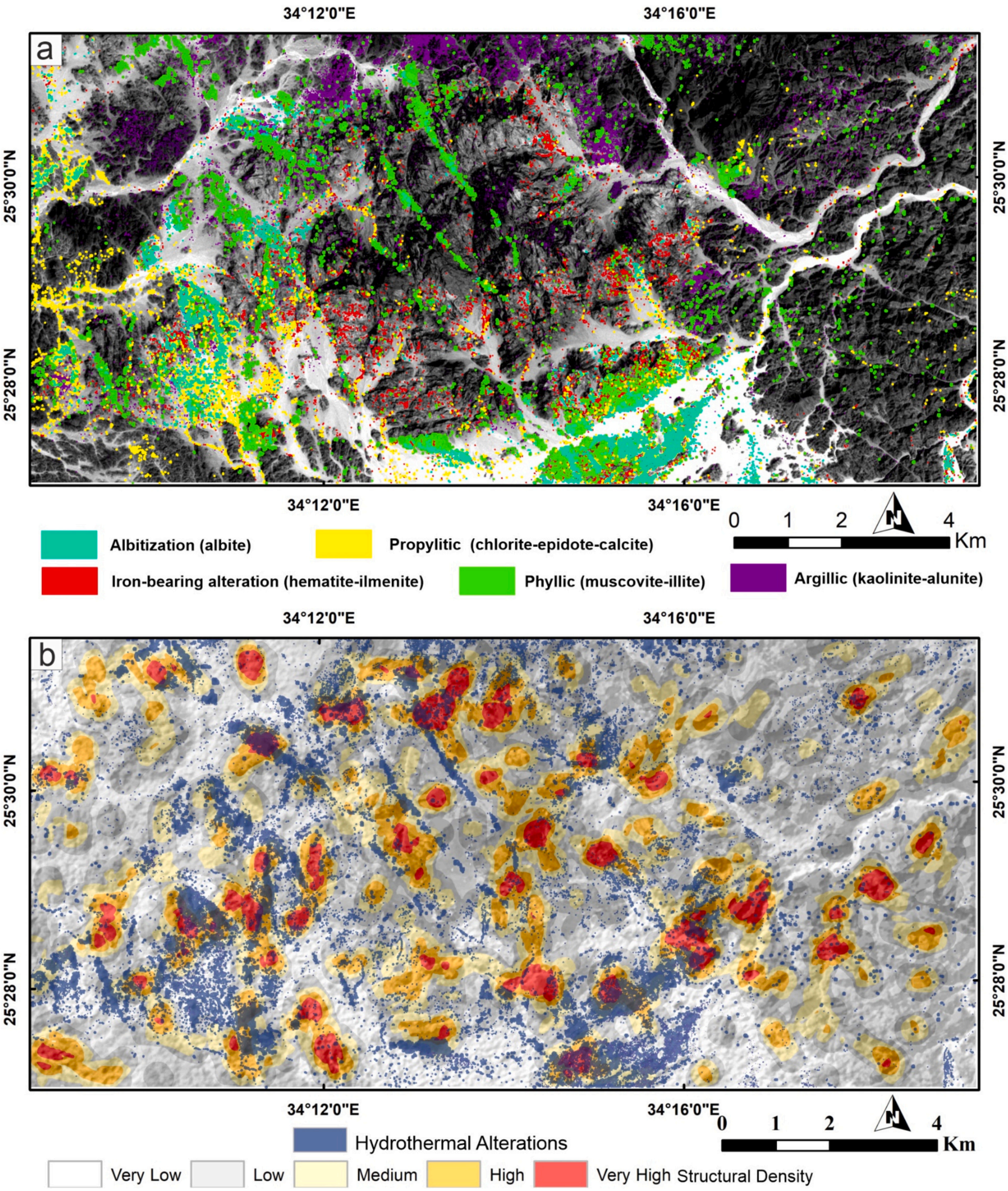

Fig. 17. (a) Integrated distribution of alteration minerals extracted by the CEM technique superimposed on a gray-scale image of ASTER band 1, and (b) integrated alteration-structural density map for correlation and potentiality interpretation within the study area.

rare metals within the Umm Naggat area.

6.2. Preliminary insights about the origin of alteration-formed rare metal minerals

Alteration is crucial in the transportation and concentration of metals, such as Nb, Ta, Sn, and W, during hydrothermal processes (Li et al., 2015; Monier and Robert, 1986; Monnier et al., 2022; Tindle and Webb, 1990; Yang et al., 2023; Yang et al., 2020b; Yin et al., 2022). Secondary minerals can precipitate directly from hydrothermal fluids or form due to the interaction between fluids and the parent mineral phases (Yang et al., 2023; Yang et al., 2020b). In the Umm Naggat granites, secondary rare metal-bearing minerals are recorded for the first time. Secondary columbite, Nb-Ta-rich rutile, and Nb-rich ilmenite are found incorporated along the cleavage planes of biotite included within secondary muscovite or chlorite (Figs. 13f and 14f). The former spatial association indicates a genetic relationship, meaning that secondary rare metal phases are formed during the alteration of biotite, particularly by muscovitization and chloritization. Despite the fact that this type of mineralization has not been reported in the study area, it is widely accepted that the alteration of biotites can result in secondary rare metal-rich minerals such as rutile, ilmenite, and titanite (Yang et al., 2023; Yang et al., 2020b; Zhu et al., 2018). According to Yang et al. (2020b) and Zhu et al. (2018), the alteration of biotite by the action of acidic and F-rich fluids during the processes of muscovitization and chloritization leads to the release of Nb, Ta, Ti, and Fe from biotite into the fluids. For instance, the Ti removal from the crystal structure of biotite can be monitored through the classification of biotite as a hydrothermally-altered type because of the depletion in its Ti content relative to its primary fresh equivalent.

Subsequently, secondary mineral phases containing high concentrations of these elements can precipitate. In addition, Yang et al. (2020b) proposed that this mineralization style represents a new potential type of Nb-Ta mineralization from biotite alteration, considering its distinct mineralogy, petrology, and texture. In addition, only a limited number of experimental studies have been conducted to examine the leaching of niobium (Nb) and tantalum (Ta) from biotite during alteration (Yang et al., 2023). In line with the findings of Yang et al. (2020b) and Zhu et al. (2018), the experimental investigations carried out by (Yang et al., 2023) showed the sequential formation of a group of alteration products consisting of titanomagnetite, ilmenite, Nb-rutile, fergusonite, and aeschynite at various temperatures. These results indicate that hydrothermal processes have the potential to cause the mineralization of Nb and the enrichment of rare metals in the form of oxides formed through alteration. Xiao and Chen (2020) studied the elemental behavior during biotite alteration to chlorite and stated that Fe, Mg, Al, and Ni are mostly retained in chlorite, whereas Co, Ga, Mn, and Zn are commonly transferred to chlorite from the hydrothermal fluid, and Sc, Sr, Si, V, Li, K, Nb, Ba, Rb, Ti, Cl, Na, Sn, and Cu from the biotite mostly do not enter chlorite during chloritization.

Nevertheless, ilmenite can occasionally be seen in isolation, not tightly associated with biotite, and documented as intergranular veins that form along grain boundaries (Fig. 12f). This suggests that Nb-rich ilmenite is formed directly from hydrothermal fluids that are rich in Ti, Nb, and Fe. To summarize, the analysis of the mineral chemistry and textures of the rare metal-bearing phases formed through alteration confirms that these minerals were precipitated as a result of secondary processes. They were directly precipitated from the hydrothermal fluids, and there was a significant increase in the concentration of these metals during the alteration of biotite into muscovite and chlorite in the studied granites. Additional mineralogical, geochemical, and textural investigation is necessary in the future to more accurately determine the origin and the geochemical mechanisms that contribute to the secondary rare metal enrichment in the Umm Naggata area.

Consequently, the hydrothermal alteration, structural mapping, spatial overlay analysis, and multi-tool validations suggest that the hydrothermal alteration system and mineralization are structurally controlled. Additionally, it is strongly favored to consider the whole pluton of the NYG as a potential source for rare metals, particularly of hydrothermal origin. Moreover, these findings have the potential to significantly contribute to future geochemical and mineralogical analysis, aiming to resolve and reconcile the ongoing debate regarding the impact of magmatic versus hydrothermal mechanisms and the origin of rare metals in the Umm Naggat area.

Furthermore, our future research will focus on incorporating hyperspectral data to explore its spectral potential in deciphering hydrothermal characteristics in the study area. While hyperspectral data like PRISMA or EnMap offer rich spectral information, their coarse spatial resolution presents a challenge. To address this limitation, we aim to integrate very high-resolution (VHR) data, such as WV-3, which can provide finer spatial detail. By combining these datasets, we anticipate improved monitoring of geochemical changes and more accurate delineation of transitions and borders within complex altered zones.

7. Conclusion

The current study integrated remote sensing techniques, airborne geophysical methods, field observations, polished samples, petrographic investigations, and mineral chemistry analysis to delineate the hydrothermal alterations pattern and structural framework in the study area. The study concludes the following:

1. Sentinel 2 and ASTER data efficiently discriminated the different granitic verities (BTG-AFG-ABG) within the NYG pluton. This lithological characterization serves as the base for improved hydrothermal alteration mapping.
2. Integrating Sentinel 2 and ASTER with various image processing techniques (MNF, BR, BM, MI, RBD, and CEM) allowed reliable detection of alteration zones and representative secondary minerals within the VNIR-SWIR range.
3. Extensive alterations, such as albitization, ferrugination, propylitization, argillization, and phyllitization, widely overprint the Umm Naggat area.
4. Aeromagnetic geophysical techniques (TD, NSTD, and 3D Euler deconvolution), remote sensing lineament extraction, and directional analysis highlighted NW, NNW, NNE, and NE as the major structural trends.
5. The high structural density and intensively altered zones are spatially associated and more localized within the NYG pluton Than the surrounding rocks.
6. Spatial overlay analysis and the concordant structural-linear alteration trends confirm that hydrothermal alteration and fluid circulation systems are structurally-controlled.
7. The mineral chemistry analysis confirms the hydrothermal genesis of rare metal-bearing minerals (Nb-rutile, Nb-ilmenite, and columbite) in the alteration zones, which might be a new potential source for Nb and Ta in Egypt. Biotite muscovitization and chloritization significantly contribute to the secondary rare metal enrichment in the Umm Naggat area.
8. The current study emphasizes the extensive distribution of rare metal mineralization within the whole NYG pluton, challenging previous studies that suggested its confinement to the Northern albitized granite.
9. The current findings recommend further geochemical and mineral chemistry investigations to assess better the role of magmatic versus hydrothermal processes in rare metal enrichment in the Umm Naggat area.

Following our multiscale investigation of hydrothermal patterns in the study area, we strongly recommend considering our integrated approach beyond the study area. Our method, characterized by its comprehensive nature and cost-effectiveness, is suitable for exploration programs targeting rare-metal-bearing minerals. We believe that adopting this method in other terrains will optimize exploration efforts and enhance the efficiency of future exploration programs.

CRediT authorship contribution statement

Mohamed A. Abdelkader: Writing – review & editing, Writing – original draft, Visualization, Validation, Software, Resources, Project administration, Methodology, Investigation, Formal analysis, Conceptualization. **Yasushi Watanabe:** Validation, Supervision, Resources, Project administration, Funding acquisition, Conceptualization. **Ali Shebl:** Writing – original draft, Software, Methodology, Investigation. **Mohamed Badawi:** Writing – original draft, Validation, Formal analysis, Conceptualization. **Maher Dawoud:** Supervision, Project administration, Investigation, Conceptualization. **Hanaa A. El-Dokouny:** Validation, Methodology, Data curation. **Árpád Csámer:** Supervision, Resources, Project administration, Funding acquisition, Data curation. **Mahmoud Abdellatif:** Writing – original draft, Visualization, Software,

Methodology, Data curation, Conceptualization.

Declaration of competing interest

The authors declare the following financial interests/personal relationships which may be considered as potential competing interests: Mohamed A. Abdelkader reports financial support, administrative support, and equipment, drugs, or supplies were provided by Akita University. Mohamed A. Abdelkader reports financial support was provided by Government of Japan Ministry of Education Culture Sports Science and Technology. Ali Shebl reports financial support and article publishing charges were provided by University of Debrecen. Ali Shebl reports financial support was provided by Tempus Public Foundation. If there are other authors, they declare that they have no known competing financial interests or personal relationships that could have appeared to influence the work reported in this paper.

Data availability

Data will be made available on request.

Acknowledgements

We would like to express our heartfelt gratitude to Dr. Ahmed Elfeky for his invaluable assistance during this research project’s fieldwork and sample collection phase. Furthermore, we would like to extend our appreciation to Dr. Osamu Nishikawa and Dr. Carmela Tupaz for their expert guidance and support in the carbon coating and SEM/EPMA analysis. The research was partially financed by the NKFI K138079. Thanks to the editors and the anonymous reviewers for their efforts in managing and improving the manuscript.

Appendix A. Supplementary data

Supplementary data to this article can be found online at https://doi.org/10.1016/j.gexplo.2024.107598.

References

Aali, A.A., Shirazy, A., Shirazi, A., Pour, A.B., Hezarkhani, A., Maghsoudi, A., Hashim, M., Khakmardan, S., 2022. Fusion of remote sensing, magnetometric, and geological data to identify polymetallic mineral potential zones in Chakchak Region, Yazd, Iran. Remote Sens. 14, 6018.

Abd El Monsef, M., Sami, M., Toksoy-Köksal, F., Abart, R., Ondrejka, M., Abdelfadil, K. M., 2023. Role of magmatism and related-exsolved fluids during Ta-Nb-Sn concentration in the Central Eastern Desert of Egypt: evidences from mineral chemistry and fluid inclusions. J. Earth Sci. 1–16.

Abd El Nabi, S.H., 2012. An analysis of airborne gamma-ray spectrometric data of Gabal umm Naggat granitic pluton, Central Eastern Desert, Egypt. JAKU Earth Sci. 23, 19–42.

Abd El Wahed, A., 2006. Mineralogical and radio-metrical characteristics of rare metal pegmatite at southern Humr Waggat Pluton, Central Eastern Desert, Egypt. J. Middle East Res. 19, 105–116 (Center. Ain Shams University, Cairo).

Abdalla, H., Mohamed, F., 1999. Mineralogical and geochemical investigation of emerald and beryl mineralisation, Pan-African Belt of Egypt: genetic and exploration aspects. J. Afr. Earth Sci. 28, 581–598.

Abdalla, H.M., Matsueda, H., Obeid, M.A., Takahashi, R., 2008. Chemistry of cassiterite in rare metal granitoids and the associated rocks in the Eastern Desert, Egypt. J. Mineral. Petrol. Sci. 103, 318–326.

Abdelkader, M.A., Watanabe, Y., Shebl, A., El-Dokouny, H.A., Dawoud, M., Csámer, Á., 2022. Effective delineation of rare metal-bearing granites from remote sensing data using machine learning methods: a case study from the Umm Naggat Area, Central Eastern Desert, Egypt. Ore Geol. Rev. 150, 105–184.

Abdelnasser, A., Khedr, L., Kharbish, S., Zoheir, B., Zamzam, S., 2023. Sulfide disseminations and hydrothermal alteration haloes in the Gabal Monqul area, Egypt: field, mineralogical, and remote sensing studies. J. Afr. Earth Sci. 199, 104830.

Abdel-Rahman, A.-F.M., El-Kibbi, M.M., 2001. Anorogenic magmatism: chemical evolution of the Mount El-Sibai A-type complex (Egypt), and implications for the origin of within-plate felsic magmas. Geol. Mag. 138, 67–85.

Abdel-Rahman, A.-F.M., Martin, R.F., 1990. The Mount Gharib A-type granite, Nubian Shield: petrogenesis and role of metasomatism at the source. Contrib. Mineral. Petrol. 104, 173–183.

Abouzeid, A.-Z.M., Khalid, A.-A.M., 2011. Mineral industry in Egypt-part I: metallic mineral commodities. Nat. Resour. 2, 35.

Abrams, M., Yamaguchi, Y., 2019. Twenty years of ASTER contributions to lithologic mapping and mineral exploration. Remote Sens. 11, 1394.

Abuamarah, B.A., Azer, M.K., Seddik, A.M., Asimow, P.D., Guzman, P., Fultz, B.T., Wilner, M., Dalleska, N., Darwish, M.H., 2022. Magmatic and post-magmatic evolution of post-collisional rare-metal bearing granite: the Neoproterozoic Homrit Akarem Granitic Intrusion, south Eastern Desert of Egypt, Arabian-Nubian Shield. Geochemistry 82, 125840.

Aero-Service, 1984. Final Report on Airborne Magnetic and Radiation Survey in Eastern Desert, Egypt, vol. 6. Work completed for the Egyptian General Petroleum Corporation (EGPC), Aero-Service, Houston, Texas, USA.

Aisabokhae, J., Tampul, H., 2019. Spectral characteristics of hydrothermal alteration in Zuru, NW Nigeria. Korean J. Remote Sens. 35, 535–544.

Akaad, M.K., AM, N., 1978. Geology and Lithostratigraphy of the Arabian Desert Orogenic Belt of Egypt Between Latitudes 25°35’and 26°30’n.

Alarifi, S.S., Abdelkareem, M., Abdalla, F., Abdelsadek, I.S., Gahlan, H., Al-Saleh, A.M., Alotaibi, M., 2022. Fusion of multispectral remote-sensing data through GIS-based overlay method for revealing potential areas of hydrothermal mineral resources. Minerals 12, 1577.

Al-Arifi, N., El-Din, G.K., Abdelkareem, M., Abdalla, F., 2021. Integration of remote-sensing, structural, and geochemical data for characterizing granitoid rocks in Um Naggat pluton, Central Eastern Desert, Egypt. Arab. J. Geosci. 14, 1–22.

Ali, H., El Ata, A.A., Youssef, M., Salem, S., Ghoneim, S., 2023. A newly-developed multi-algorithm integration technique for mapping the potentially mineralized alteration zones. Egypt. J. Remote Sens. Space Sci. 26, 691–711.

Alrefaee, H., Kamh, S., Elhossainy, M., 2023. Integrating the remote sensing and aeromagnetic data to delineate the structural elements and mineralization zones in Safaga area, Eastern Desert, Egypt. Delta J. Sci. 46, 123–143.

Anwar, M., Abu El-Leil, I., Salem, S., 2023. Lithological and alteration mapping at the Um El-Rus Area, Central Eastern Desert, Egypt, using remote sensing techniques. J. Indian Soc. Remote Sens. 51, 829–848.

Araffa, S.A.S., Abd-AlHai, M.M., Mekkawi, M.M., ElGalladi, A.A.-M., 2022. Integrated geophysical, remote sensing and geochemical investigation to explore gold-mineralizations and mapping listvenites at Wadi Haimur, Eastern Desert, Egypt. Geocarto Int. 37, 17565–17602.

Atif, Y., Soulaimani, A., Ait lamqadem, A., Pour, A.B., Pradhan, B., Nouamane, E.A., Abdelali, K., Muslim, A.M., Hossain, M.S., 2022. Identifying hydrothermally altered rocks using ASTER satellite imageries in Eastern Anti-Atlas of Morocco: a case study from Imiter silver mine. Int. J. Image Data Fusion 13, 337–361.

Azer, M.K., Abdelfadil, K.M., Ramadan, A.A., 2019. Geochemistry and petrogenesis of Late Ediacaran rare-metal albite granite of the Nubian Shield: case study of Nuweibi intrusion, Eastern Desert, Egypt. J. Geol. 127, 665–689.

Badawi, M.A., Mahmoud, Shebl, Ali, Makroum, Farid, Shalaby, Ahmed, Németh, Norbert, 2023. Mapping structurally controlled alterations sparked by hydrothermal activity in the Fatira–Abu Zawal Area, Eastern Desert, Egypt. Acta Geol. Sin. - Engl. Ed. 97, 662–680.

Badr, Y.S., Dawoud, M., Arab, A.A., 2014. Geochemical Prospecting for Radioactive Mineralization at G. Um Naggat-G. Atawy Area, Central Eastern Desert, Egypt (MSc Thesis). Menoufia Univ., Egypt.

Bajwa, R.S., Ahsan, N., Ahmad, S.R., 2020. A review of landsat false color composite images for lithological mapping of Pre-Cambrian to recent rocks: a case study of Pail/Padhrar Area in Punjab Province, Pakistan. J. Indian Soc. Remote Sens. 48, 721–728.

Bentor, Y., 1985. The crustal evolution of the Arabo-Nubian Massif with special reference to the Sinai Peninsula. Precambrian Res. 28, 1–74.

Bety, A.K.S., 2022. Discrimination different lithological units using a remote sensing application: a case study in the Dokan Area, Kurdistan Region-Iraq. J. Water Land Dev. 55, 109–114.

Beygi, S., Talovina, I.V., Tadayon, M., Pour, A.B., 2021. Alteration and structural features mapping in Kacho-Mesqal zone, Central Iran using ASTER remote sensing data for porphyry copper exploration. Int. J. Image Data Fusion 12, 155–175.

Beyth, M., Stern, R.J., Altherr, R., Kröner, A., 1994. The late Precambrian Timna igneous complex, southern Israel: evidence for comagmatic-type sanukitoid monzodiorite and alkali granite magma. Lithos 31, 103–124.

Bishta, A.Z., Sonbul, A.R., Kashghari, W., 2014. Utilization of supervised classification in structural and lithological mapping of Wadi Al-Marwah Area, NW Arabian Shield, Saudi Arabia. Arab. J. Geosci. 7, 3855–3869.

Bonin, B., 2004. Do coeval mafic and felsic magmas in post-collisional to within-plate regimes necessarily imply two contrasting, mantle and crustal, sources? A review. Lithos 78, 1–24.

Canbaz, O., 2023. Application of spectral analysis and image processing methods to discriminate hydrothermal alteration minerals around the Tutakdağı (Şebinkarahisar-Giresun) Lead–Zinc Deposits, Northeastern Turkey. J. Indian Soc. Remote Sens. 1–21.

Cardoso-Fernandes, J., Teodoro, A.C., Lima, A., Roda-Robles, E., 2020. Semi-automatization of support vector machines to map lithium (Li) bearing pegmatites. Remote Sens. 12, 2319.

Cardoso-Fernandes, J., Silva, J., Dias, F., Lima, A., Teodoro, A.C., Barrès, O., Cauzid, J., Perrotta, M., Roda-Robles, E., Ribeiro, M.A., 2021. Tools for remote exploration: a lithium (li) dedicated spectral library of the fregeneda–almendra aplite–pegmatite field. Data 6, 33.

Černý, P., 1989. Characteristics of pegmatite deposits of tantalum. In: Lanthanides, Tantalum and Niobium: Mineralogy, Geochemistry, Characteristics of Primary Ore Deposits, Prospecting, Processing and Applications Proceedings of a workshop in Berlin, November 1986. Springer, pp. 195–239.

Chen, Q., Zhao, Z.-F., Xia, J.-S., Zhao, X., Yang, H.-Y., Zhang, X.-L., 2022. Improving the accuracy of hydrothermal alteration mapping based on image fusion of ASTER and

Sentinel-2A data: a case study of Pulang Cu deposit, Southwest China. Geocarto Int. 37, 13923–13948.

Cooper, G.R., Cowan, D.R., 2008. Edge enhancement of potential-field data using normalized statistics. Geophysics 73, H1–H4.

Crowley, J.K., Brickey, D.W., Rowan, L.C., 1989. Airborne imaging spectrometer data of the Ruby Mountains, Montana: mineral discrimination using relative absorption band-depth images. Remote Sens. Environ. 29, 121–134.

Dawood, Y.H., 2010. Mineral chemistry and genesis of uranyl minerals associated with psammitic gneisses, Abu Rusheid area, South Eastern Desert of Egypt. J. King Abdulaziz Univ.: Earth Sci. 150, 1–66.

Dawoud, M.K., El-Dokouny, Ibrahim, M., Shebl, Hanaa, A., El-Desouky, Ali, El-Lithy, Hamdy, A., Mai, A., 2023. Applications of remote sensing in lithological mapping of East Gabal Atud area, central Eastern Desert, Egypt. Geo-Eco-Marina 29, 125–146.

Denghui, Z., Le, Y., 2011. Support vector machine based classification for hyperspectral remote sensing images after minimum noise fraction rotation transformation. In: 2011 International Conference on Internet Computing and Information Services. IEEE, pp. 132–135.

Ducart, D.F., Silva, A.M., Toledo, C.L.B., Assis, L.M.d., 2016. Mapping iron oxides with Landsat-8/OLI and EO-1/Hyperion imagery from the Serra Norte iron deposits in the Carajás Mineral Province, Brazil. Braz. J. Geol. 46, 331–349.

El Hadek, H.H., Mohamed, M., Bishara, W.W., El Habaak, G.H., Ali, K.A., 2016. Evolution of mineralizing fluids of greisen and fluorite veins, evidence from fluid inclusions. Inter. J. Geophys. Geochem. 3, 49–56.

El-Afandy, A.H., Abdalla, H.M., Aly, M.M., Ammar, F., 2000. Geochemistry and radioactive potentiality of Um Naggat apogranite, central eastern desert, Egypt. Resour. Geol. 50, 39–51.

El-Desoky, H.M., Shebl, A., Abdel-Rahman, A.M., Fahmy, W., El-Awny, H., El-Sherif, A. M., El-Rahmany, M.M., Csámer, Á., 2022a. Multiscale mineralogical investigations for mineral potentiality mapping of Ras El-Kharit-Wadi Khashir district, Southern Eastern Desert, Egypt. Egypt. J. Remote Sens. Space Sci. 25, 941–960.

El-Desoky, H.M., Tende, A.W., Abdel-Rahman, A.M., Ene, A., Awad, H.A., Fahmy, W., El-Awny, H., Zakaly, H.M., 2022b. Hydrothermal alteration mapping using landsat 8 and ASTER data and geochemical characteristics of Precambrian rocks in the Egyptian shield: a case study from Abu Ghalaga, Southeastern Desert, Egypt. Remote Sens. 14, 3456.

El-Desoky, H., Shebl, A., El-Awny, H., El-Rahmany, M., Soliman, O., 2023. Detecting oxides mineralization utilizing remote sensing and comprehensive mineralogical analysis: a case study around Mikbi-Zayatit District, South Eastern Desert, Egypt. Iraqi Geol. J. 97–130.

El-Dokouny, H., Watanabe, Y., Mahmoud, A., Dawoud, M., 2023. Geochemistry and petrogenesis of late Neoproterozoic Nuweibi and Atawi rare metals bearing granites, central Eastern Desert, Egypt. J. Afr. Earth Sci. 206, 105–123, 105023.

El-Gaby, S., List, F.K., Tehrani, R., 1988. Geology, Evolution and Metallogenesis of the Pan-African Belt in Egypt, the Pan-African Belt of Northeast Africa and Adjacent Areas: Tectonic Evolution and Economic Aspects of a Late Proterozoic Oregon, pp. 17–68.

El-Qassas, R.A.Y., Abu-Donia, A.M., Omar, A.E.A., 2023. Delineation of hydrothermal alteration zones associated with mineral deposits, using remote sensing and airborne geophysics data. A case study: El-Bakriya area, Central Eastern Desert, Egypt. Acta Geod. Geophys. 58, 71–107.

El-Rus, M.A.A., Mohamed, M.A., Lindh, A., 2017. Mueilha rare metals granite, Eastern Desert of Egypt: an example of a magmatic-hydrothermal system in the Arabian-Nubian Shield. Lithos 294, 362–382.

El-Sayed, M.M., 2006. Geochemistry and petrogenesis of late Neoproterozoic peraluminous anorogenic leucogranite, Zabara area, Central Eastern Desert, Egypt. Neues Jb. Miner. Abh. 79–91.

El-Sayed, M., Obeid, M., Furnes, H., Moghazi, A., 2004. Late Neoproterozoic volcanism in the southern Eastern Desert, Egypt: petrological, structural and geochemical constraints on the tectonic-magmatic evolution of the Allaqi Dokhan volcanic suite. Neues Jb. Miner. Abh. 261–286.

Emam, A., Zoheir, B., Radwan, A.M., Lehmann, B., Zhang, R., Fawzy, S., Nolte, N., 2018. Petrogenesis and evolution of the Nuweibi rare-metal granite, Central Eastern Desert, Egypt. Arab. J. Geosci. 11, 1–15.

Fahmy, W., El-Desoky, H., Elyaseer, M., Ayonta Kenne, P., Shirazi, A., Hezarkhani, A., Shirazy, A., El-Awny, H., Abdel-Rahman, A., Khalil, A., 2023a. Remote sensing and petrological and geochemical data for lithological mapping in Wadi Kid, Southeast Sinai, Egypt. Minerals 13, 1160.

Fahmy, W., El-Desoky, H.M., Elyaseer, M.H., Ayonta Kenne, P., Shirazi, A., Hezarkhani, A., Shirazy, A., El-Awny, H., Abdel-Rahman, A.M., Khalil, A.E., 2023b. Remote Sensing, Petrological and Geochemical Data for Lithological Mapping in Wadi Kid, Southeast Sinai, Egypt. Minerals 13, 1160.

Farrand, W.H., Harsanyi, J.C., 1997. Mapping the distribution of mine tailings in the Coeur d'Alene River Valley, Idaho, through the use of a constrained energy minimization technique. Remote Sens. Environ. 59, 64–76.

Foster, M.D., 1960. Interpretation of the Composition of Trioctahedral Micas: A Study of the Compositional and Layer Charge Relations of Phlogipites, Biotites, Siderophyllites and Lepidomelanes. US Government Printing Office.

Fotze, Q.M.A., Lordon, A.E.D., Penaye, J., Sep, J.P., Fru, M.I.N., 2019. Mapping hydrothermal alteration targets from Landsat 8 OLI/TIRS and magnetic data using digital image processing techniques in Garoua, North Cameroon. J. Geosci. 7, 28–41.

Fowler, T., 2001. Pan-African granite emplacement mechanisms in the Eastern Desert, Egypt. J. Afr. Earth Sci. 32, 61–86.

Frutuoso, R., Lima, A., Teodoro, A.C., 2021. Application of remote sensing data in gold exploration: targeting hydrothermal alteration using Landsat 8 imagery in northern Portugal. Arab. J. Geosci. 14, 1–18.

Gaafar, I., 2015. Integration of geophysical and geological data for delimitation of mineralized zones in Um Naggat area, Central Eastern Desert, Egypt. NRIAG J. Astron. Geophys. 4, 86–99.

Gaafar, I., Elbarbary, M., Sayyed, M., Sulieman, A., Tamam, N., Khandaker, M.U., Bradley, D.A., Hanfi, M.Y., 2022. Assessment of radioactive materials in albite granites from Abu Rusheid and Um Naggat, Central Eastern Desert, Egypt. Minerals 12, 120.

Gabr, S.S., Diab, H., Fattah, T.A.A., Sadek, M.F., Khalil, K.I., Youssef, M.A., 2022. Aeromagnetic and Landsat-8 data interpretation for structural and hydrothermal alteration mapping along the Central and Southern Eastern Desert boundary, Egypt. Egypt. J. Remote Sens. Space Sci. 25, 11–20.

Gamal-Adeen, I., Shahien, M., Zayed, A., Bakhit, B., Sanislav, I., Sharib, A.A., 2023. Sequential deuteric and hydrothermal alterations in the Late Neoproterozoic Um Naggat rare metal-bearing granite, Central Eastern Desert, Egypt. J. Afr. Earth Sci. 203, 104932.

Garson, M.S., Krs, M., 1976. Geophysical and geological evidence of the relationship of Red Sea transverse tectonics to ancient fractures. Geol. Soc. Am. Bull. 87, 169–181.

Gemusse, U., Cardoso-Fernandes, J., Lima, A., Teodoro, A., 2023. Identification of pegmatites zones in Muiane and Naipa (Mozambique) from Sentinel-2 images, using band combinations, band ratios, PCA and supervised classification. Remote Sens. Appl. Soc. Environ. 32, 101022.

Ghoneim, S., Yehia, M., Salem, S., Ali, H., 2022. Integrating remote sensing data, GIS analysis and field studies for mapping alteration zones at Wadi Saqia area, central Eastern Desert, Egypt. Egypt. J. Remote Sens. Space Sci. 25, 323–336.

Green, A.A., Berman, M., Switzer, P., Craig, M.D., 1988. A transformation for ordering multispectral data in terms of image quality with implications for noise removal. IEEE Trans. Geosci. Remote Sens. 26, 65–74.

Gupta, R.P., 2003. Remote Sensing Geology. Springer Berlin Heidelberg, Berlin (655 pp.).

Hamimi, Z., El-Barkooky, A., Frías, J.M., Fritz, H., Abd El-Rahman, Y., 2020. The Geology of Egypt. Springer.

Hamimi, Z., Arai, S., Fowler, A.-R., El-Bialy, M.Z., 2021a. The Geology of the Egyptian Nubian Shield. Springer.

Hamimi, Z., Fowler, A.-R., Liégeois, J.-P., Collins, A., Abdelsalam, M.G., Abd El-Wahed, M., 2021b. The Geology of the Arabian-Nubian Shield. Springer.

Harlaux, M., Mercadier, J., Bonzi, W.M.-E., Kremer, V., Marignac, C., Cuney, M., 2017. Geochemical signature of magmatic-hydrothermal fluids exsolved from the Beauvoir rare-metal granite (Massif Central, France): insights from LA-ICPMS analysis of primary fluid inclusions. Geofluid 2017 (1), 1925817.

Harsanyi, J.C., 1993. Detection and Classification of Subpixel Spectral Signatures in Hyperspectral Image Sequences. University of Maryland, Baltimore County.

Hassan, M.A., Hashad, A.H., 1990. Precambrian of Egypt. In: Said, R. (Ed.), The Geology of Egypt. Balkema, Rotterdam, pp. 201–245.

Hegab, M.A.E.-R., Mousa, S.E., Salem, S.M., Farag, K., GabAllah, H., 2022. Gold-related alteration zones detection at the Um Balad Area, Egyptian Eastern Desert, using remote sensing, geophysical, and GIS data analysis. J. Afr. Earth Sci. 196, 104715.

Hewson, R., Cudahy, T., Drake-Brockman, J., Meyers, J., Hashemi, A., 2006. Mapping geology associated with manganese mineralisation using spectral sensing techniques at Woodie Woodie, East Pilbara. Explor. Geophys. 37, 389–400.

Holben, B., Justice, C., 1981. An examination of spectral band ratioing to reduce the topographic effect on remotely sensed data. Int. J. Remote Sens. 2, 115–133.

Hung, L., Batelaan, O., San, D., 2003. Lineament analysis in fractured rocks, methodology and application to the Suoimuoi karst catchment (extended abstract and full paper). In: Finds and Results From the Swedish Cyprus Expedition: A Gender Perspective at the Medelhavsmuseet.

Hung, L., Batelaan, O., De Smedt, F., 2005. Lineament extraction and analysis, comparison for LANDSAT ETM and ASTER. In: Case study: Suoimuoi tropical karst catchment, Vietnam, GIS Applications, and Geology V.

Hussein, A.A., 1973. Results of mineral exploration program in South-Eastern Desert of Egypt. Ann. Geol. Surv. Egypt III, 109–123.

Ibrahim, I.H., 2013. Impact of structural lineaments on mineralized occurrences in North Abu Rusheid-Sikait Area, South Eastern Desert, Egypt. In: Proceedings of the 5th Tunisian Days of Applied Geology JTGA, pp. 227–251.

Immaculate, N.-F.M., Tende, A.W., Fouateu, Y.R., Marc, A.F.Q., 2020. Remote sensing for geological investigation of Mayo Kila and environs, north west region of Cameroon. Am. J. Earth Sci. 7, 1–12.

Johnson, P.R., 2021. The Arabian–Nubian Shield, an introduction: historic overview, concepts, interpretations, and future issues. In: The Geology of the Arabian-Nubian Shield, pp. 1–38.

Johnson, P., Andresen, A., Collins, A., Fowler, A., Fritz, H., Ghebreab, W., Kusky, T., Stern, R., 2011. Late Cryogenian–Ediacaran history of the Arabian–Nubian Shield: a review of depositional, plutonic, structural, and tectonic events in the closing stages of the northern East African Orogen. J. Afr. Earth Sci. 61, 167–232.

Kaur, P., Chaudhri, N., Hofmann, A.W., Raczek, I., Okrusch, M., Skora, S., Baumgartner, L.P., 2012. Two-stage, extreme albitization of A-type granites from Rajasthan, NW India. J. Petrol. 53, 919–948.

Khedr, M.Z., Khashaba, S.M.A., El-Shibiny, N., Takazawa, E., Hassan, S.M., Azer, M.K., Whattam, S.A., El-Arafy, R.A., Ichiyama, Y., 2023. Integration of remote sensing and geochemical data to characterize mineralized A-type granites, Egypt: implications for origin and concentration of rare metals. Int. J. Earth Sci. 1–29.

Köhler, M., Hanelli, D., Schaefer, S., Barth, A., Knobloch, A., Hielscher, P., Cardoso-Fernandes, J., Lima, A., Teodoro, A.C., 2021. Lithium potential mapping using artificial neural networks: a case study from Central Portugal. Minerals 11, 1046.

Krs, M., 1977. Rift tectonics development in the light of geophysical data: Red Sea region. Stud. Geophys. Geod. 21, 342–350.

Küster, D., 2009. Granitoid-hosted Ta mineralization in the Arabian–Nubian Shield: ore deposit types, tectono-metallogenetic setting and petrogenetic framework. Ore Geol. Rev. 35, 68–86.

Li, J., Huang, X.-L., He, P.-L., Li, W.-X., Yu, Y., Chen, L.-l., 2015. In situ analyses of micas in the Yashan granite, South China: constraints on magmatic and hydrothermal evolutions of W and Ta–Nb bearing granites. Ore Geol. Rev. 65, 793–810.

Liegeois, J.-P., Navez, J., Hertogen, J., Black, R., 1998. Contrasting origin of post-collisional high-K calc-alkaline and shoshonitic versus alkaline and peralkaline granitoids. The use of sliding normalization. Lithos 45, 1–28.

Lundmark, A.M., Andresen, A., Hassan, M.A., Augland, L.E., Boghdady, G.Y., 2012. Repeated magmatic pulses in the East African Orogen in the Eastern Desert, Egypt: an old idea supported by new evidence. Gondwana Res. 22, 227–237.

Maged, M., Mazlan, H., 2010. Developing adaptive algorithm for automatic detection of geological linear features using RADARSAT-1 SAR data. Int. J. Phys. Sci. 5, 2223–2229.

Mahanta, P., Maiti, S., 2022. Remote detection of hydrothermal alteration zones using WorldView-3 VNIR-SWIR reflectance data: a study from Lawa Gold Mines, India. J. Indian Soc. Remote Sens. 50, 1979–1993.

Mahdi, A.M., Eldosouky, A.M., El Khateeb, S.O., Youssef, A.M., Saad, A.A., 2022. Integration of remote sensing and geophysical data for the extraction of hydrothermal alteration zones and lineaments; Gabal Shilman basement area, Southeastern Desert, Egypt. J. Afr. Earth Sci. 194, 104640.

Mars, J.C., Rowan, L.C., 2006. Regional mapping of phyllic-and argillic-altered rocks in the Zagros magmatic arc, Iran, using Advanced Spaceborne Thermal Emission and Reflection Radiometer (ASTER) data and logical operator algorithms. Geosphere 2, 161–186.

Megwara, J.U., Udensi, E.E., 2014. Structural analysis using aeromagnetic data: case study of parts of Southern Bida Basin, Nigeria and the surrounding basement rocks. Earth Sci. Res. 3, 27.

Melcher, F., Graupner, T., Gäbler, H.-E., Sitnikova, M., Henjes-Kunst, F., Oberthür, T., Gerdes, A., Dewaele, S., 2015. Tantalum–(niobium–tin) mineralisation in African pegmatites and rare metal granites: constraints from Ta–Nb oxide mineralogy, geochemistry and U–Pb geochronology. Ore Geol. Rev. 64, 667–719.

Meyyappan, M., Brijesh, V., 2022. Mapping of sittampundi anorthosite complex (sac) in southern granulite terrain (sgt), India with aster and Sentinel-2A data. ADBU J. Eng. Technol. 11.

Michaud, J.A.-S., Pichavant, M., 2020. Magmatic fractionation and the magmatic-hydrothermal transition in rare metal granites: evidence from Argemela (Central Portugal). Geochim. Cosmochim. Acta 289, 130–157.

Miller, H.G., Singh, V., 1994. Potential field tilt—a new concept for location of potential field sources. J. Appl. Geophys. 32, 213–217.

Moghazi, A., Mohamed, F., Kanisawa, S., 1999. Geochemical and petrological evidence of calc-alkaline and A-type magmatism in the Homrit Waggat and El-Yatima areas of eastern Egypt. J. Afr. Earth Sci. 29, 535–549.

Monier, G., Robert, J.-L., 1986. Evolution of the miscibility gap between muscovite and biotite solid solutions with increasing lithium content: an experimental study in the system K2O-Li2O-MgO-FeO-Al2O3-SiO2-H2O-HF at 600° C, 2 kbar PH2O: comparison with natural lithium micas. Mineral. Mag. 50, 641–651.

Monnier, L., Salvi, S., Melleton, J., Lach, P., Pochon, A., Bailly, L., Béziat, D., De Parseval, P., 2022. Mica trace-element signatures: highlighting superimposed W-Sn mineralizations and fluid sources. Chem. Geol. 600, 120866.

Nachit, H., 1985. Composition chemique des biotites et typologie magmatique des granitoids. C. R. Hebd. Acad. Sci. 301, 813–818.

Nations, U., 1973. Assessment of the mineral potential of the Aswan region: Technical report, follow-up geophysical survey (1968–1972) for the Government of the ARE. In: DP/SFIUN/114, New York (90 pp.).

Ninomiya, Y., 2003a. Advanced remote lithologic mapping in ophiolite zone with ASTER multispectral thermal infrared data. In: International Geoscience and Remote Sensing Symposium (III: 1561–1563 pp.).

Ninomiya, Y., 2003b. A stabilized vegetation index and several mineralogic indices defined for ASTER VNIR and SWIR data, IGARSS 2003. In: 2003 IEEE International Geoscience and Remote Sensing Symposium. Proceedings (IEEE Cat. No. 03CH37477). IEEE, pp. 1552–1554.

Ninomiya, Y., 2004. Lithologic mapping with multispectral ASTER TIR and SWIR data, Sensors, Systems, and Next-Generation Satellites VII. SPIE 180–190.

Ninomiya, Y., Fu, B., Cudahy, T.J., 2005. Detecting lithology with Advanced Spaceborne Thermal Emission and Reflection Radiometer (ASTER) multispectral thermal infrared "radiance-at-sensor" data. Remote Sens. Environ. 99, 127–139.

Niyeh, M.M., Jafarirad, A., Karami, J., Hydrothermal Alteration Mapping Using Multispectral Satellite Images in Cenozoic Volcanic Rocks of Tafresh Area, Markazi province, Central Iran.

Olatunji, S., 2022. Integration of remote sensing and geophysical methods for structural and lithological mapping in a part of Precambrian Basement Rocks, northern Nigeria. J. Fundam. Appl. Sci. 14, 161–180.

Osinowo, O.O., Gomy, A., Isseini, M., 2021. Mapping hydrothermal alteration mineral deposits from Landsat 8 satellite data in Pala, Mayo Kebbi Region, Southwestern Chad. Sci. Afr. 11, e00687.

Ousmanou, S., Fozing, E.M., Kwékam, M., Fodoue, Y., Jeatsa, L.D.A., 2023. Application of remote sensing techniques in lithological and mineral exploration: discrimination of granitoids bearing iron and corundum deposits in southeastern Banyo, Adamawa region-Cameroon. Earth Sci. Inf. 16, 259–285.

Pazand, K., Pazand, K., 2022. Identification of hydrothermal alteration minerals for exploring porphyry copper deposit using ASTER data: a case study of Varzaghan area, NW Iran. Geol. Ecol. Landsc. 6, 217–223.

Pohl, C., van Genderen, J., 2014. Remote sensing image fusion: an update in the context of Digital Earth. Int. J. Digit. Earth 7, 158–172.

Pour, A.B., Hashim, M., 2012. The application of ASTER remote sensing data to porphyry copper and epithermal gold deposits. Ore Geol. Rev. 44, 1–9.

Pour, A.B., Hashim, M., Park, Y., Hong, J.K., 2018. Mapping alteration mineral zones and lithological units in Antarctic regions using spectral bands of ASTER remote sensing data. Geocarto Int. 33, 1281–1306.

Pour, A.B., Hashim, M., Hong, J.K., Park, Y., 2019a. Lithological and alteration mineral mapping in poorly exposed lithologies using Landsat-8 and ASTER satellite data: North-eastern Graham Land, Antarctic Peninsula. Ore Geol. Rev. 108, 112–133.

Pour, A.B., Park, T.-Y.S., Park, Y., Hong, J.K., Muslim, A.M., Läufer, A., Crispini, L., Pradhan, B., Zoheir, B., Rahmani, O., 2019b. Landsat-8, advanced spaceborne thermal emission and reflection radiometer, and WorldView-3 multispectral satellite imagery for prospecting copper-gold mineralization in the northeastern Inglefield Mobile Belt (IMB), northwest Greenland. Remote Sens. 11, 2430.

Qari, M., Madani, A., Matsah, M., Hamimi, Z., 2008. Utilization of Aster and Landsat data in geologic mapping of basement rocks of Arafat Area, Saudi Arabia. Arab. J. Sci. Eng. 33, 99–116.

Rani, N., Mandla, V.R., Singh, T., 2022. Structural and alteration mapping using ASTER imagery and DEM for gold mineralization in the Gadag Schist Belt of Karnataka, India. In: Atlas of Structural Geological and Geomorphological Interpretation of Remote Sensing Images, pp. 197–204.

Reid, A.B., Allsop, J., Granser, H., Millett, A.t., Somerton, I., 1990. Magnetic interpretation in three dimensions using Euler deconvolution. Geophysics 55, 80–91.

Robb, L., 2005. Introduction to Ore-Forming Processes. Blackwell Publishing, Malden, MA.

Rowan, L.C., Mars, J.C., 2003. Lithologic mapping in the Mountain Pass, California area using advanced spaceborne thermal emission and reflection radiometer (ASTER) data. Remote Sens. Environ. 84, 350–366.

Ruiz Cruz, M.D., Nieto, J.M., 2006. Chemical and structural evolution of "metamorphic vermiculite" in metaclastic rocks of the Betic Cordillera, Málaga, Spain: a synthesis. Can. Mineral. 44, 249–265.

Sabet, T., 1973. Problems of geological and economic evaluation of tantalum deposits in apogranites during stages of prospection and exploration. In: Annals of the Geological Survey of Egypt, 3, pp. 87–107.

Sabins Jr., F.F., Ellis, J.M., 2020. Remote Sensing: Principles, Interpretation, and Applications. Waveland Press.

Saed, S., Azizi, H., Daneshvar, N., Afzal, P., Whattam, S.A., Mohammad, Y.O., 2022. Hydrothermal alteration mapping using ASTER data, Takab-Baneh area, NW Iran: a key for further exploration of polymetal deposits. Geocarto Int. 37, 11456–11482.

Said, R., 1990. The Geology of Egypt: Balkema. Rotterdam, Brookfield, p. 734.

Salawu, N.B., Omosanya, K.O.L., Eluwole, A.B., Saleh, A., Adebiyi, L.S., 2023. Structurally-controlled gold mineralization in the southern Zuru Schist Belt NW Nigeria: application of remote sensing and geophysical methods. J. Appl. Geophys. 211, 104969.

Salem, S., El Sharkawi, M., El-Alfy, Z., Soliman, N., Ahmed, S., 2016. Exploration of gold occurrences in alteration zones at Dungash district, Southeastern Desert of Egypt using ASTER data and geochemical analyses. J. Afr. Earth Sci. 117, 389–400.

Sami, M., Ntaflos, T., Farahat, E.S., Mohamed, H.A., Ahmed, A.F., Hauzenberger, C., 2017. Mineralogical, geochemical and Sr-Nd isotopes characteristics of fluorite-bearing granites in the Northern Arabian-Nubian Shield, Egypt: constraints on petrogenesis and evolution of their associated rare metal mineralization. Ore Geol. Rev. 88, 1–22.

Sami, M., Ntaflos, T., Farahat, E.S., Mohamed, H.A., Hauzenberger, C., Ahmed, A.F., 2018. Petrogenesis and geodynamic implications of Ediacaran highly fractionated A-type granitoids in the north Arabian-Nubian Shield (Egypt): constraints from whole-rock geochemistry and Sr-Nd isotopes. Lithos 304, 329–346.

Sami, M., El Monsef, M.A., Abart, R., Toksoy-Koksal, F., Abdelfadil, K.M., 2022. Unraveling the genesis of highly fractionated rare-metal granites in the nubian shield via the rare-earth elements tetrad effect, Sr–Nd isotope systematics, and mineral chemistry. ACS Earth Space Chem. 6, 2368–2384.

Santos, D., Cardoso-Fernandes, J., Lima, A., Müller, A., Brönner, M., Teodoro, A.C., 2022. Spectral analysis to improve inputs to random forest and other boosted ensemble tree-based algorithms for detecting NYF pegmatites in Tysfjord, Norway. Remote Sens. 14, 3532.

Sayah, E.M.B., Rahimi, A., Saber, N., Kholaiq, M., Maacha, L., 2023. Mineralogical mapping using remote sensing and geophysical data in IMITER Anti-Atlas of Morocco. Remote Sens. Earth Syst. Sci. 6, 77–89.

Sayed, F., Hammed, M.S.H., Shided, A.G., Hussein, A.W., 2023. Implementation of remote sensing techniques in structural and lithological mapping of Northwestern Margin of Red Sea, Egypt. J. Min. Environ. 14, 389–411.

Sekandari, M., Masoumi, I., Pour, A.B., Muslim, A.M., Hossain, M.S., Misra, A., 2022. ASTER and WorldView-3 satellite data for mapping lithology and alteration minerals associated with Pb-Zn mineralization. Geocarto Int. 37, 1782–1812.

Sengar, V.K., Venkatesh, A., Sahoo, P., Khan, I., Chattoraj, S.L., 2020. Spaceborne mapping of hydrothermal alteration zones associated with the Mundiyawas-Khera copper deposit, Rajasthan, India, using SWIR bands of ASTER: implications for exploration targeting. Ore Geol. Rev. 118, 103327.

Shebl, A., Csámer, Á., 2021. Reappraisal of DEMs, Radar and optical datasets in lineaments extraction with emphasis on the spatial context. Remote Sens. Appl. Soc. Environ. 24, 100617.

Shebl, A., Hamdy, M., 2023. Multiscale (microscopic to remote sensing) preliminary exploration of auriferous-uraniferous marbles: a case study from the Egyptian Nubian Shield. Sci. Rep. 13, 9173.

Shebl, A., Abdellatif, M., Elkhateeb, S.O., Csámer, Á., 2021. Multisource data analysis for gold potentiality mapping of Atalla area and its environs, Central Eastern Desert, Egypt. Minerals 11, 641.

Shebl, A., Abdelaziz, M.I., Ghazala, H., Araffa, S.A.S., Abdellatif, M., Csámer, Á., 2022. Multi-criteria ground water potentiality mapping utilizing remote sensing and geophysical data: a case study within Sinai Peninsula, Egypt. Egypt. J. Remote Sens. Space Sci. 25, 765–778.

Shebl, A., Abdellatif, M., Badawi, M., Dawoud, M., Fahil, A.S., Csámer, Á., 2023a. Towards better delineation of hydrothermal alterations via multi-sensor remote sensing and airborne geophysical data. Sci. Rep. 13, 7406.

Shebl, A., Abriha, D., Fahil, A.S., El-Dokouny, H.A., Elrasheed, A.A., Csámer, Á., 2023b. PRISMA hyperspectral data for lithological mapping in the Egyptian Eastern Desert: evaluating the support Vector Machine, Random Forest, and XG Boost Machine Learning Algorithms. Ore Geol. Rev., 105652

Sillitoe, R.H., 2010. Porphyry copper systems. Econ. Geol. 105, 3–41.

Stern, R.J., 1994. Arc assembly and continental collision in the Neoproterozoic East African Orogen: implications for the consolidation of Gondwanaland. Annu. Rev. Earth Planet. Sci. 22, 319–351.

Stern, R.J., Gottfried, D., 1986. Petrogenesis of a late Precambrian (575–600 Ma) bimodal suite in northeast Africa. Contrib. Mineral. Petrol. 92, 492–501.

Su, H.-M., Jiang, S.-Y., Zhu, X.-Y., Duan, Z.-P., Huang, X.-K., Zou, T., 2021. Magmatic-hydrothermal processes and controls on rare-metal enrichment of the Baerzhe peralkaline granitic pluton, inner Mongolia, northeastern China. Ore Geol. Rev. 131, 103984.

Thompson, D., 1982. EULDPH: a new technique for making computer-assisted depth estimates from magnetic data. Geophysics 47, 31–37.

Tindle, A.G., Webb, P.C., 1990. Estimation of lithium contents in trioctahedral micas using microprobe data; application to micas from granitic rocks. Eur. J. Mineral. 2, 595–610.

Van der Meer, F.D., Van der Werff, H.M., Van Ruitenbeek, F.J., Hecker, C.A., Bakker, W. H., Noomen, M.F., Van Der Meijde, M., Carranza, E.J.M., De Smeth, J.B., Woldai, T., 2012. Multi-and hyperspectral geologic remote sensing: a review. Int. J. Appl. Earth Obs. Geoinf. 14, 112–128.

Van der Meer, F., Van der Werff, H., Van Ruitenbeek, F., 2014. Potential of ESA's Sentinel-2 for geological applications. Remote Sens. Environ. 148, 124–133.

Weerasekara, W., Mayadunna, B., Senanayake, I., Dissanayake, D., 2014. Integrated remote sensing and GIS in lineament mapping for groundwater exploration–a case study in Ambalantota, Sri Lanka. In: Proceeding of SAITM Research Symposium on Engineering Advancements. South Asian Institute of Technology and Medicine Malabe, Sri Lanka (62e65 pp.).

Xi, Y., Mohamed Taha, A.M., Hu, A., Liu, X., 2022. Accuracy comparison of various remote sensing data in lithological classification based on random forest algorithm. Geocarto Int. 37, 14451–14479.

Xiao, B., Chen, H., 2020. Elemental behavior during chlorite alteration: New insights from a combined EMPA and LA-ICPMS study in porphyry Cu systems. Chem. Geol. 543, 119604.

Yang, W.-B., Niu, H.-C., Li, N.-B., Hollings, P., Zurevinski, S., Xing, C.-M., 2020a. Enrichment of REE and HFSE during the magmatic-hydrothermal evolution of the Baerzhe alkaline granite, NE China: implications for rare metal mineralization. Lithos 358, 105411.

Yang, Z., Wang, R., Che, X., Yin, R., Xie, L., Hu, H., 2020b. Formation of columbite and microlite after alteration of Nb-and Ta-bearing biotite from the Lizaizhai pegmatite (Guangning ore district, Guangdong, South China): identification of a new potential Nb–Ta mineralization type. J. Asian Earth Sci. 190, 104154.

Yang, Z.-Y., Wang, R.-C., Che, X.-D., Harlov, D., 2023. Restrictions on Niobium enrichment by alteration of Niobium-rich biotite in pure water, acid, alkaline and fluoride-bearing solutions at 200 MPa and 300–600 °C. Geochim. Cosmochim. Acta 343, 115–132.

Yin, R., Huang, X.-L., Wang, R.-C., Sun, X.-M., Tang, Y., Wang, Y., Xu, Y.-G., 2022. Rare-metal enrichment and Nb–Ta fractionation during magmatic–hydrothermal processes in rare-metal granites: evidence from zoned micas from the Yashan pluton, South China. J. Petrol. 63, egac093.

Zamyad, M., Afzal, P., Pourkermani, M., Nouri, R., Jafari, M.R., 2019. Determination of hydrothermal alteration zones using remote sensing methods in Tirka area, Toroud, NE Iran. J. Indian Soc. Remote Sens. 47, 1817–1830.

Zhu, Z., Wang, R., Marignac, C., Cuney, M., Mercadier, J., Che, X., Lespinasse, M.-Y., 2018. A new style of rare metal granite with Nb-rich mica: the Early Cretaceous Huangshan rare-metal granite suite, northeast Jiangxi Province, southeast China. Am. Mineral. 103, 1530–1544.

Zhu, Z.-Y., Wang, R.-C., Marignac, C., Cuney, M., Mercadier, J., Che, X.-D., Charles, N., Lespinasse, M., 2019. Petrogenesis of Nb–(Ta) aplo-pegmatites and fine-grained granites from the Early Cretaceous Huangshan rare-metal granite suite, northeast Jiangxi Province, southeast China. Lithos 346, 105150.

Zoheir, B., Lehmann, B., Emam, A., Radwan, A., Zhang, R., Bain, W.M., Steele-MacInnis, M., Nolte, N., 2020. Extreme fractionation and magmatic–hydrothermal transition in the formation of the Abu Dabbab rare-metal granite, Eastern Desert, Egypt. Lithos 352, 105329.